White LED

Byungwoo Park

Department of Materials Science and Engineering
Seoul National University

http://bp.snu.ac.kr

First Report on Electroluminescence (First LED)

A Note on Carborundum.

To the Editors of Electrical World:

SIRS:—During an investigation of the unsymmetrical passage of current through a contact of carborundum and other substances a curious phenomenon was noted. On applying a potential of 10 volts between two points on a crystal of carborundum, the crystal gave out a yellowish light. Only one or two specimens could be found which gave a bright glow on such a low voltage, but with 110 volts a large number could be found to glow. In some crystals only edges gave the light and others gave instead of a yellow light green, orange or blue. In all cases tested the glow appears to come from the negative pole. a bright blue-green spark appearing at the positive pole. In a single crystal, if contact is made near the center with the negative pole, and the positive pole is put in contact at any other place, only one section of the crystal will glow and that the same section wherever the positive pole is placed.

There seems to be some connection between the above effect and the e.m.f. produced by a junction of carborundum and another conductor when heated by a direct or alternating current; but the connection may be only secondary as an obvious explanation of the e.m.f. effect is the thermoelectric one. The writer would be glad of references to any published account of an investigation of this or any allied phenomena.

NEW YORK, N. Y. H. J. ROUND.

Fig. 1.1. Publication reporting on a "curious phenomenon", namely the first observation of electroluminescence from a SiC (carborundum) light-emitting diode. The article indicates that the first LED was a Schottky diode rather than a p-n-junction diode (after H. J. Round, *Electrical World* **49**, 309, 1907).

History of LED

1907 First report on LED

1955 GaAs LED (infrared emission)

1962 First practical visible-spectrum LED (General Electric)

1993 Blue LED based on InGaN (Shuji Nakamura, Nichia)

1996 First commercial white LED (Nichia)

The development of LED technology has caused the efficiency and light output to increase exponentially, with a doubling approximately every 36 months since the 1960s, in a way similar to Moore's law.

History of LED (Applications)

Fig. 1.7. AT&T telephone set ("Trimline" model) with the dial pad illuminated by two green N-doped GaP LEDs. The illumina-ted dial pad was one of the first applications of green GaP:N LEDs.

E. F. Schubert
Light-Emitting Diodes (Cambridge Univ. Press)
www.LightEmittingDiodes.org

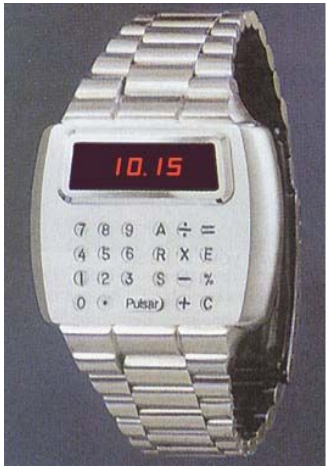

Fig. 1.8. Pulsar calculator watch with LED display released in 1975 by Hamilton Corporation. The first Pulsar LED watch (without calculator) was offered in 1972. It was based on GaInP LEDs (after Seiko, 2004).

E. F. Schubert
Light-Emitting Diodes (Cambridge Univ. Press)
www.LightEmittingDiodes.org

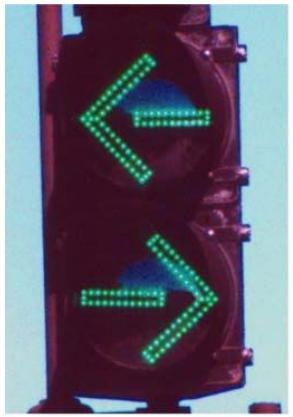

Fig. 1.12. Green traffic signals are one of the ubiquitous applications of GaInN/GaN green LEDs.

E. F. Schubert
Light-Emitting Diodes (Cambridge Univ. Press)
www.LightEmittingDiodes.org

Applications of LED

Illumination

Electimes

Illumination

Lucevista 2007 in Seoul

LCD Backlight

Samsung Electronics

White LED

LEDshop

Applications of LED

Growth Rates

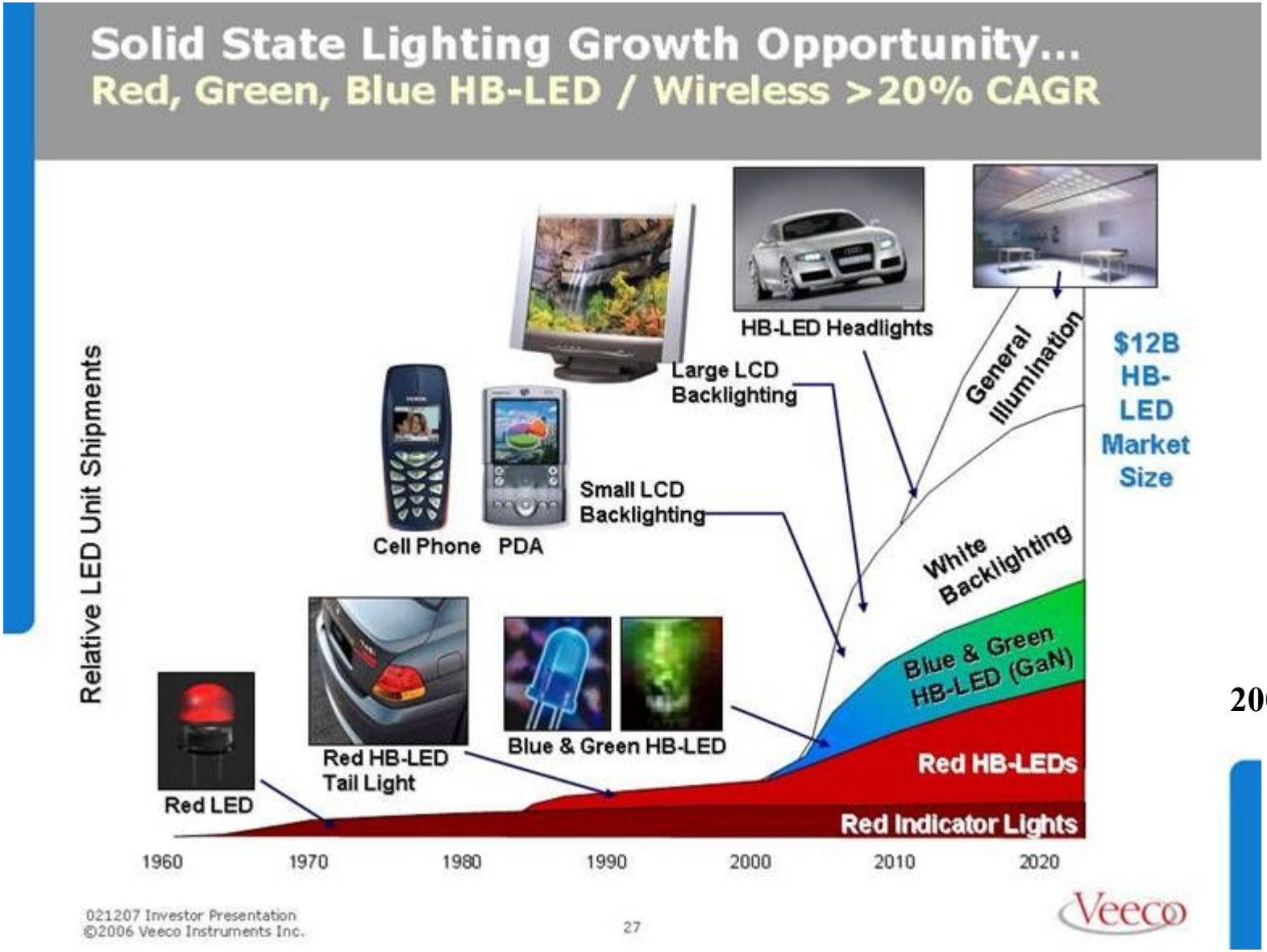

2007. 02

Progress in Luminous Efficiency of LEDs

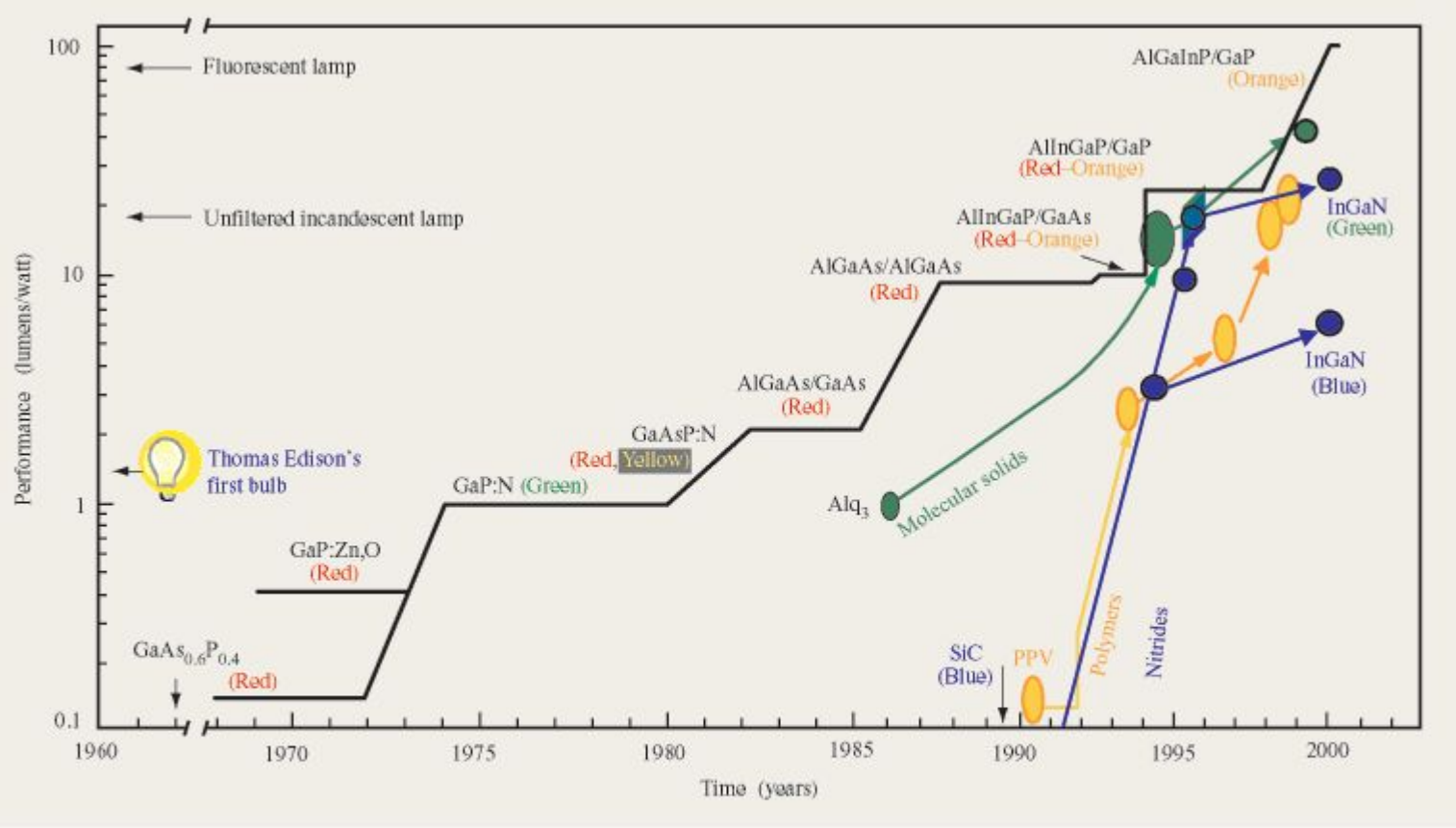

Figure 5

Evolution of LED/OLED performance. (Reprinted with permission from [24]; © 1996 American Association for the Advancement of Science.)

www.research.ibm.com

Electron-Hole Recombination of *p-n* Junction

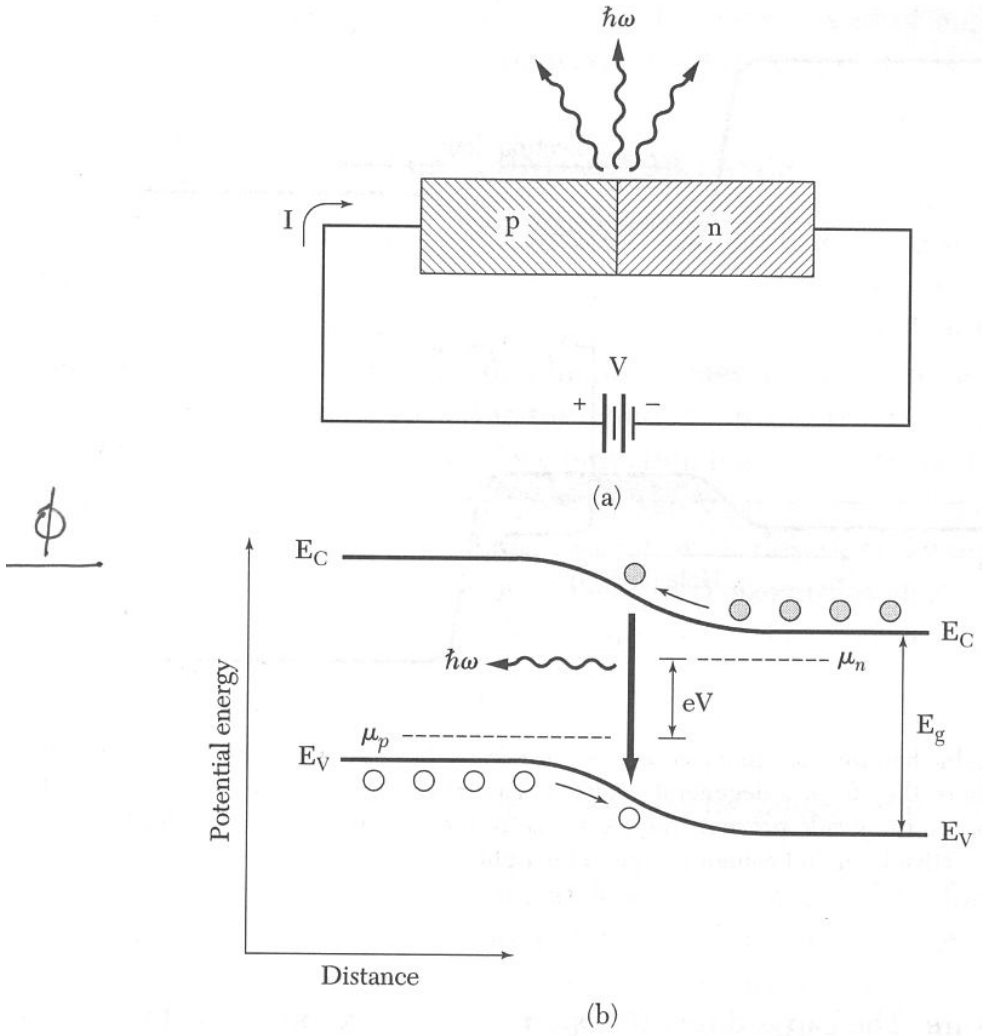

Figure 18 Electron-hole recombination into photons, across a *p-n* junction.

C. Kittel
Introduction to Solid State Physics

Double Heterostructure Injection Laser

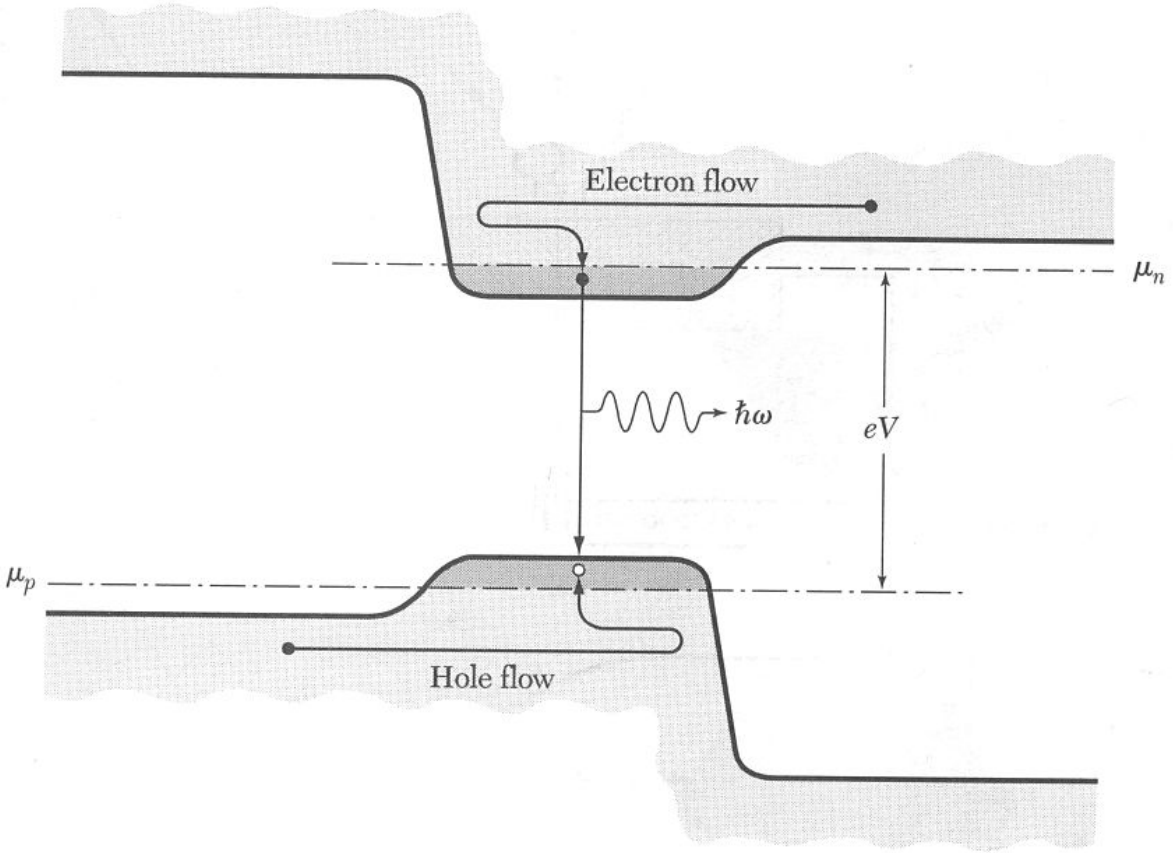

Figure 17 Double heterostructure injection laser. Electrons flow from the right into the optically-active layer, where they form a degenerate electron gas. The potential barrier provided by the wide energy gap on the p side prevents the electrons from escaping to the left. Holes flow from the left into the active layer, but cannot escape to the right.

C. Kittel
Introduction to Solid State Physics

Homojunction and Double Heterojunction

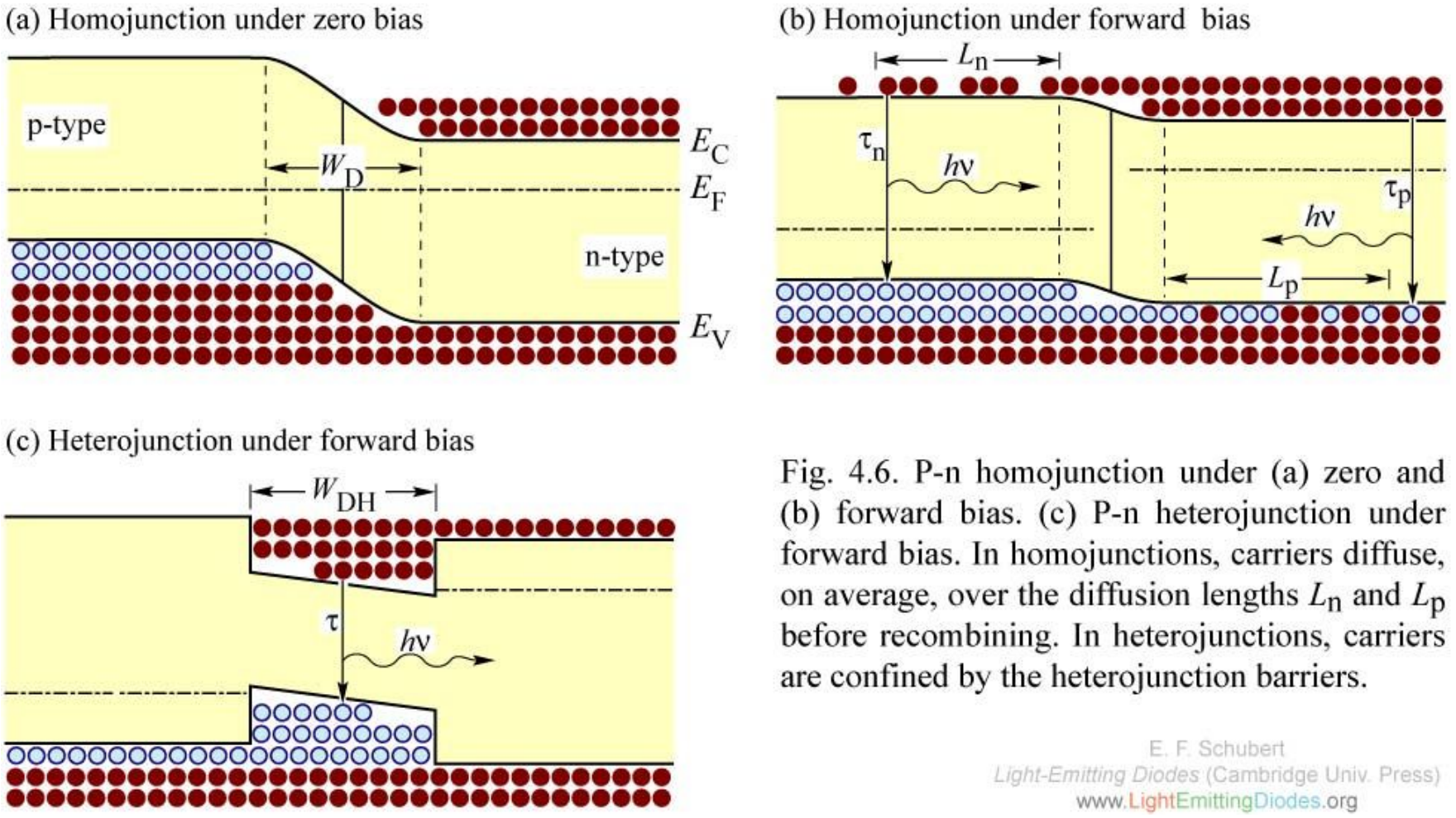

Fig. 4.6. P-n homojunction under (a) zero and (b) forward bias. (c) P-n heterojunction under forward bias. In homojunctions, carriers diffuse, on average, over the diffusion lengths L_n and L_p before recombining. In heterojunctions, carriers are confined by the heterojunction barriers.

Double Heterostructure

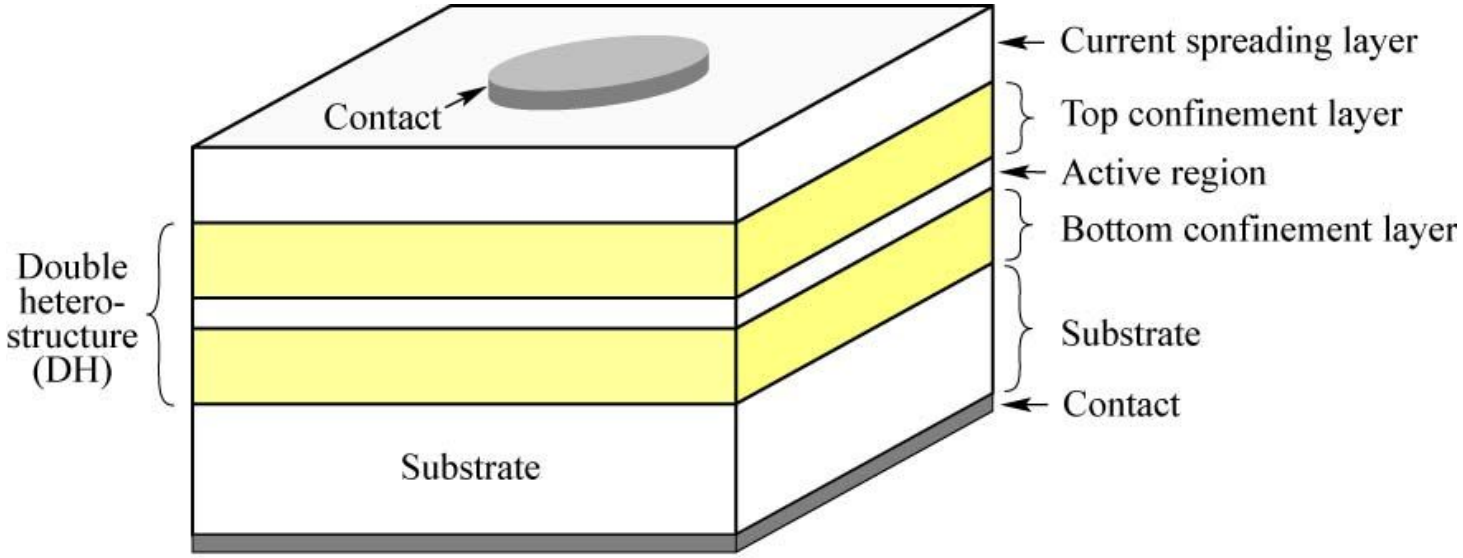

Fig. 7.1. Illustration of a double heterostructure consisting of a bulk or quantum well active region and two confinement layers. The *confinement* layers are frequently called *cladding* layers.

➔ **Confinement of carriers in the active region of double heterostructure (DH).**

➔ **High carrier concentration in the active region of DH.**

Multi Quantum Well Structure

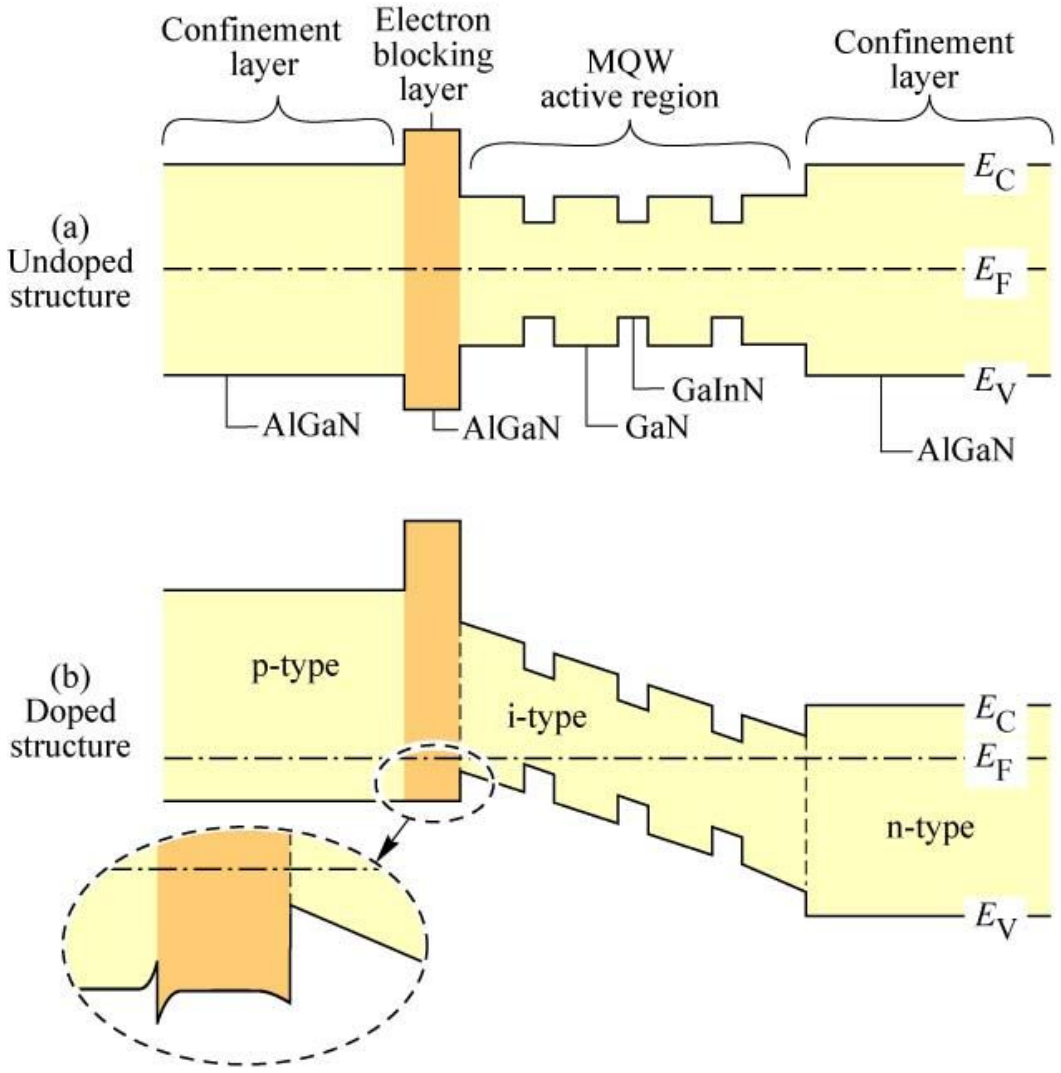

Fig. 4.12. AlGaN current-blocking layer in an AlGaN/GaN/GaInN multi quantum well structure. (a) Band diagram without doping. (b) Band diagram with doping. The Al content in the electron-blocking layer is higher than in the p-type confinement layer.

Structures of InGaN LED

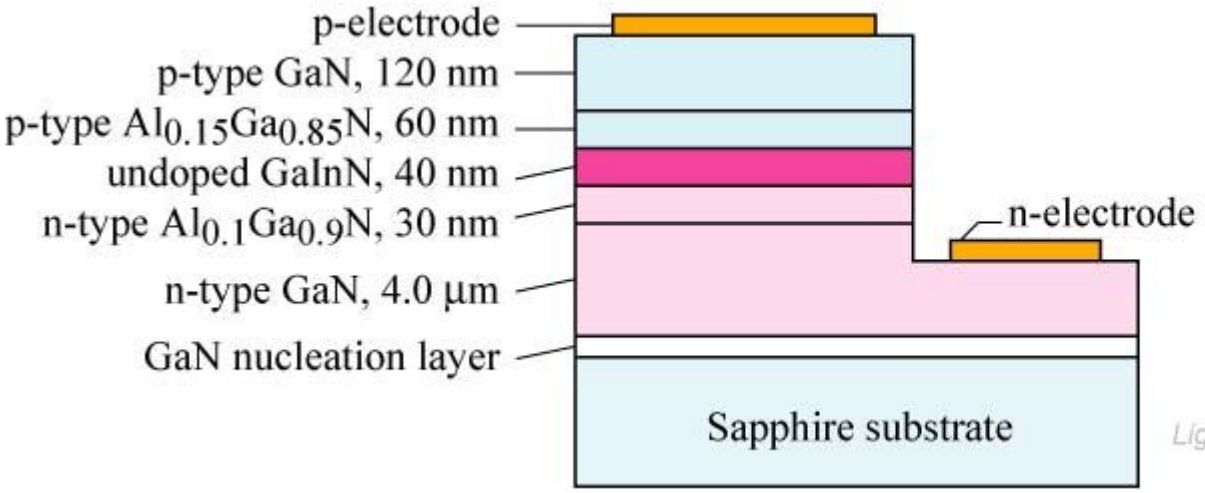

Fig. 13.2. Layer structure of GaInN UV LED grown on saphire substrate emitting at 370 nm (after Mukai *et al.*, 1998).

Trapped Light Problem

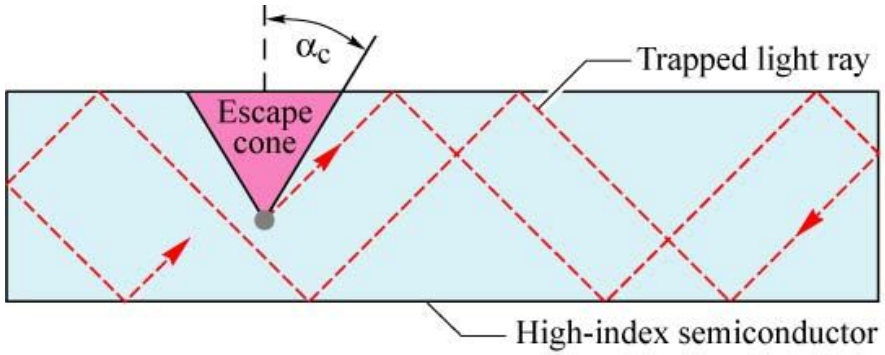

Fig. 9.3. "Trapped light" in a rectangular-parallelepiped-shaped semiconductor unable to escape for emission angles greater than α_c due to total internal reflection.

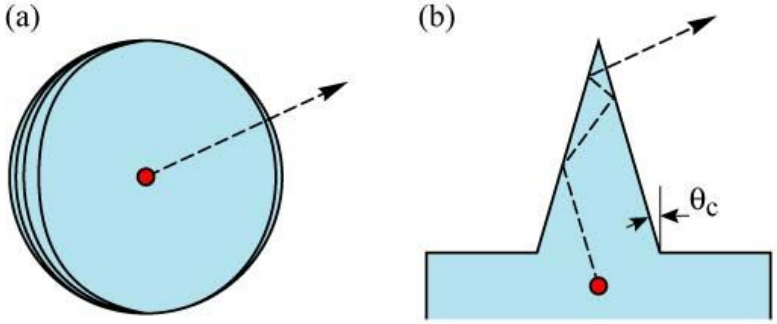

Fig. 9.4. Schematic illustration of different geometric shapes for LEDs with perfect extraction efficiency. (a) Spherical LED with a point-like light-emitting region at the center of the sphere. (b) A cone-shaped LED.

➔ **However, these structures are not practical. - High cost!!**

Truncated Inverted Pyramid (TIP) LED

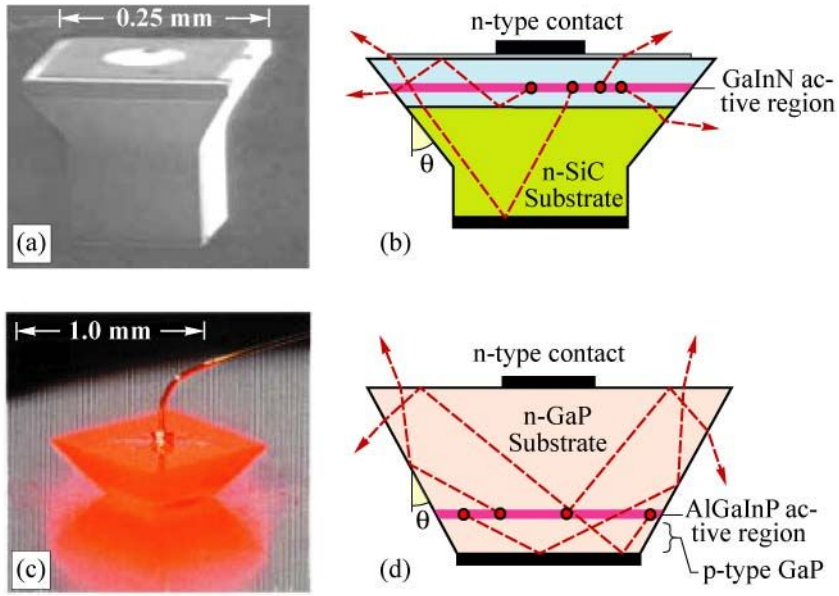

Fig. 9.6. Die-shaped devices: (a) Blue GaInN emitter on SiC substrate with trade name "Aton". (b) Schematic ray traces illustrating enhanced light extraction. (c) Micrograph of truncated inverted pyramid (TIP) AlGaInP/GaP LED. (d) Schematic diagram illustrating enhanced extraction (after Osram, 2001; Krames *et al.*, 1999).

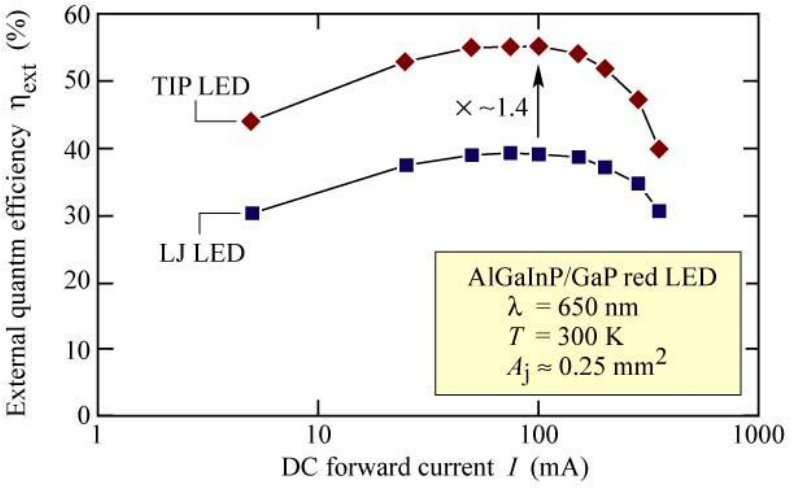

Fig. 9.7. External efficiency vs. forward current for red-emitting (650 nm) truncated inverted pyramid (TIP) LEDs and large junction (LJ) LEDs mounted in power-lamp packages. The TIP LED exhibits a 1.4 times improvement in extraction efficiency compared with the LJ device, resulting in a peak external quantum efficiency of 55 % at 100 mA (after Krames *et al.*, 1999).

Structures of OLED

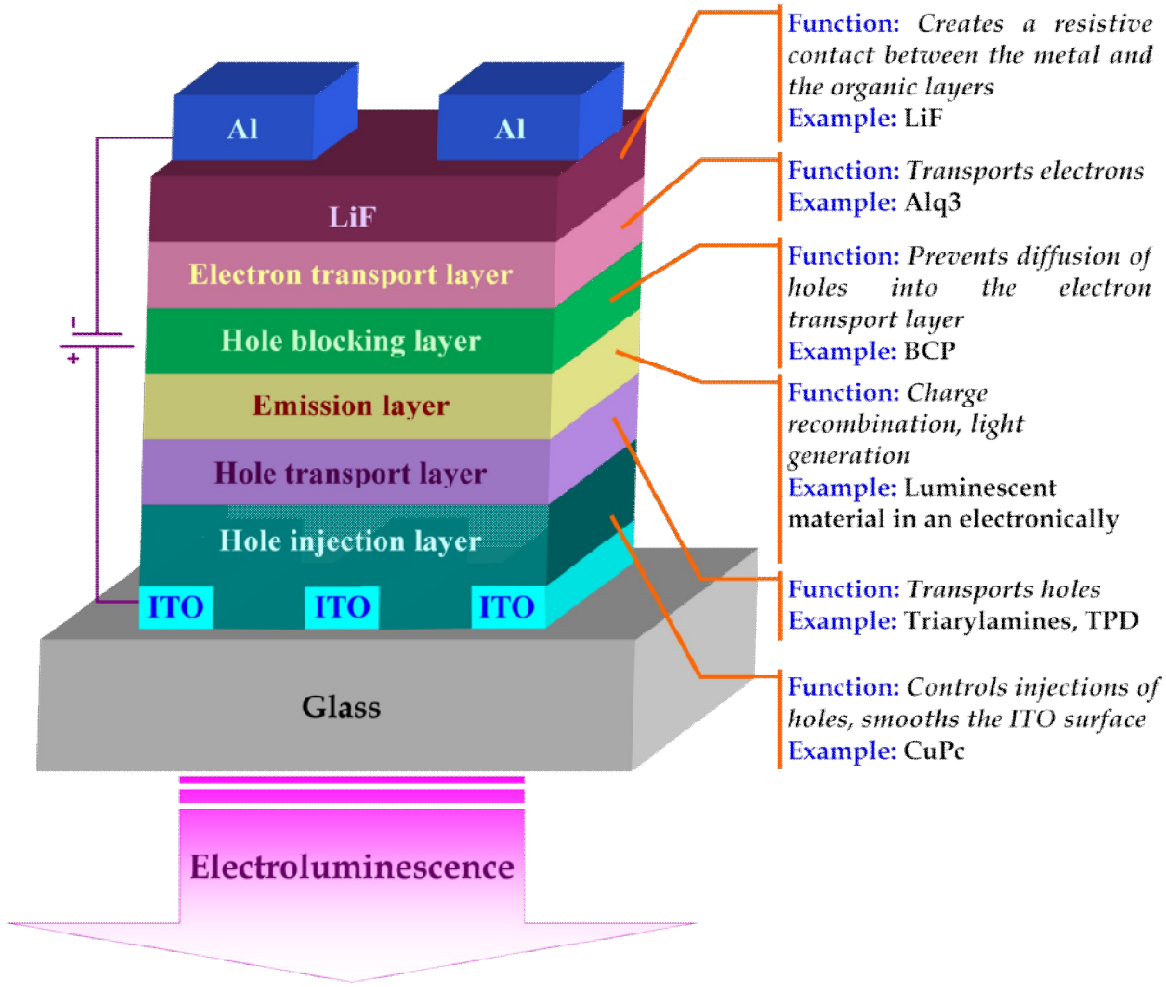

Schematic illustration of multi layer structure of small molecule based OLED

Ecole Polytechnique

White LED Devices

- Nichia High-Power LED

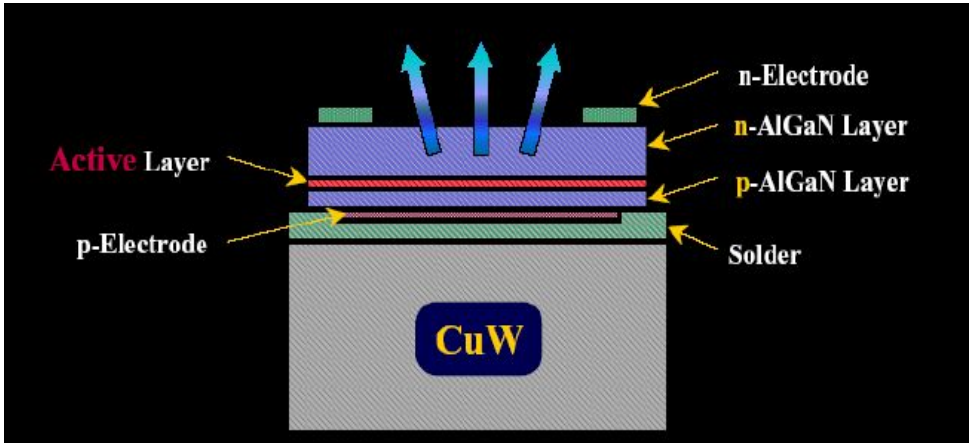

- UV LED & RGB Phosphor

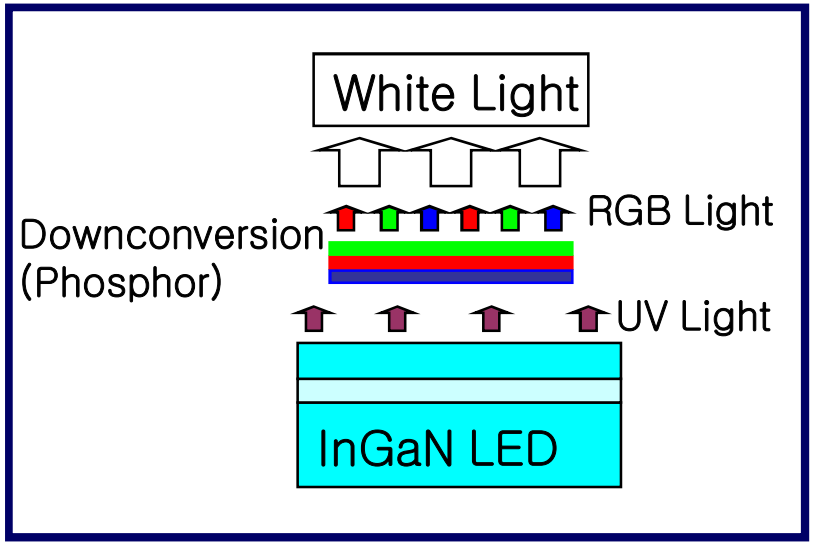

Color and Energy

Color	Wavelength	Wavenumber	Energy
Ultraviolet	< 390 nm	> 1.61×10^{-2} nm^{-1}	> 3.18 eV
Violet	390 – 455 nm	1.61 - 1.38×10^{-2} nm^{-1}	3.18 - 2.73 eV
Blue	455 – 490 nm	1.38 - 1.28×10^{-2} nm^{-1}	2.73 - 2.53 eV
Cyan	490 – 510 nm	1.28 - 1.23×10^{-2} nm^{-1}	2.53 - 2.43 eV
Green	515 – 570 nm	1.23 - 1.10×10^{-2} nm^{-1}	2.43 - 2.18 eV
Color	**Wavelength**	**Wavenumber**	**Energy**
Yellow	570 – 600 nm	1.10 - 1.05×10^{-2} nm^{-1}	2.18 - 2.07 eV
Amber	590 – 600 nm	1.06 - 1.05×10^{-2} nm^{-1}	2.10 - 2.07 eV
Orange	600 – 625 nm	1.05 - 1.01×10^{-2} nm^{-1}	2.07 - 1.98 eV
Red	625 – 720 nm	1.01×10^{-2} - 8.73×10^{-3} nm^{-1}	1.98 - 1.72 eV
Infrared	> 720 nm	< 8.73×10^{-3} nm^{-1}	< 1.72 eV

Color	Wavelength	Wavenumber	Energy
Blue	~460 nm	~1.37×10^{-2} nm^{-1}	~2.70 eV
Green	~525 nm	~1.20×10^{-2} nm^{-1}	~2.36 eV
Red	~670 nm	~9.38×10^{-3} nm^{-1}	~1.83 eV

Human Vision

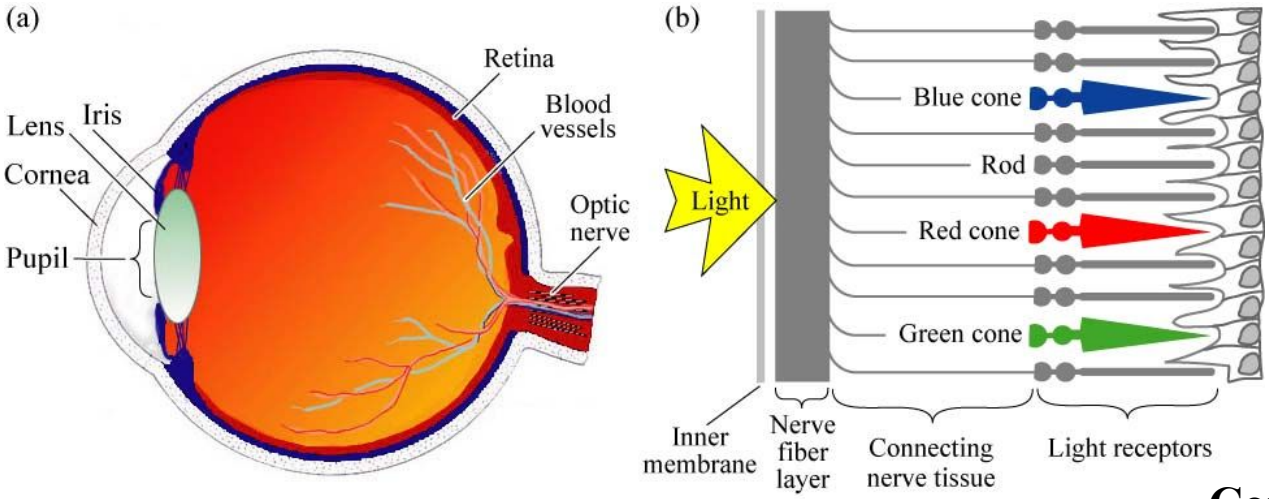

Fig. 16.1. (a) Cross section through a human eye. (b) Schematic view of the retina including rod and cone light receptors (adapted from Encyclopedia Britannica, 1994).

Cones: provide color sensitivity

Rods: color insensitive

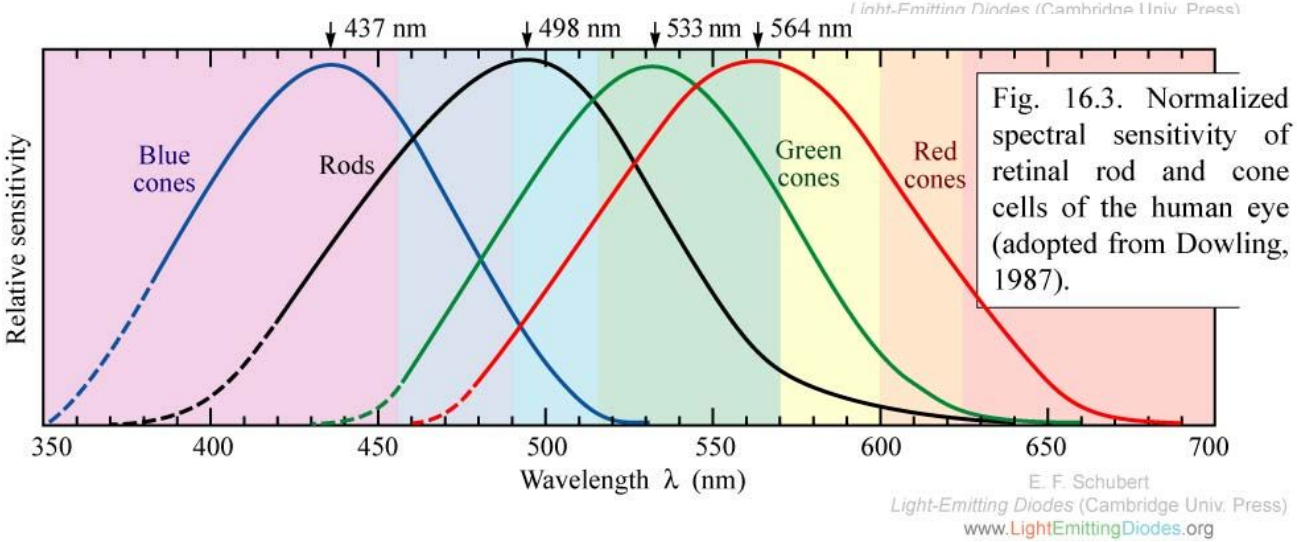

Fig. 16.3. Normalized spectral sensitivity of retinal rod and cone cells of the human eye (adopted from Dowling, 1987).

Eye Sensitivity Function and Luminous Efficiency

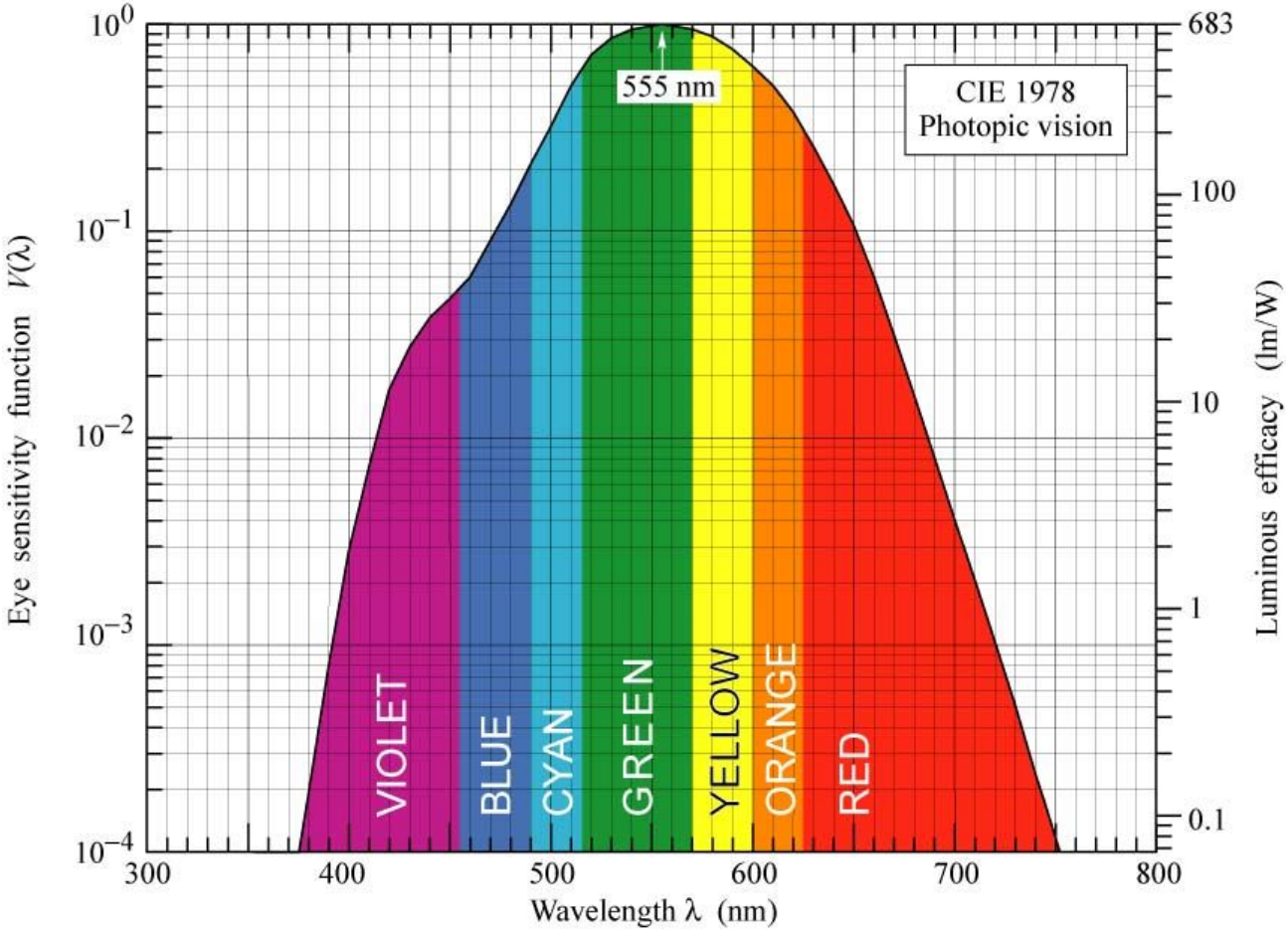

Fig. 16.7. Eye sensitivity function, $V(\lambda)$, (left ordinate) and luminous efficacy, measured in lumens per Watt of optical power (right ordinate). $V(\lambda)$ is greatest at 555 nm. Also given is a polynomial approximation for $V(\lambda)$ (after 1978 CIE data).

E. F. Schubert
Light-Emitting Diodes (Cambridge Univ. Press)
www.LightEmittingDiodes.org

- Definition of Lumen: Green light (555 nm) with power of 1 W has luminous flux 683 lm
- Among LEDs with same output power, green LEDs are brightest

CIE Color Triangle

CIE = COMMISSION INTERNATIONALE DE L'ECLAIRAGE
= INTERNATIONAL COMMISSION ON ILLUMINATION

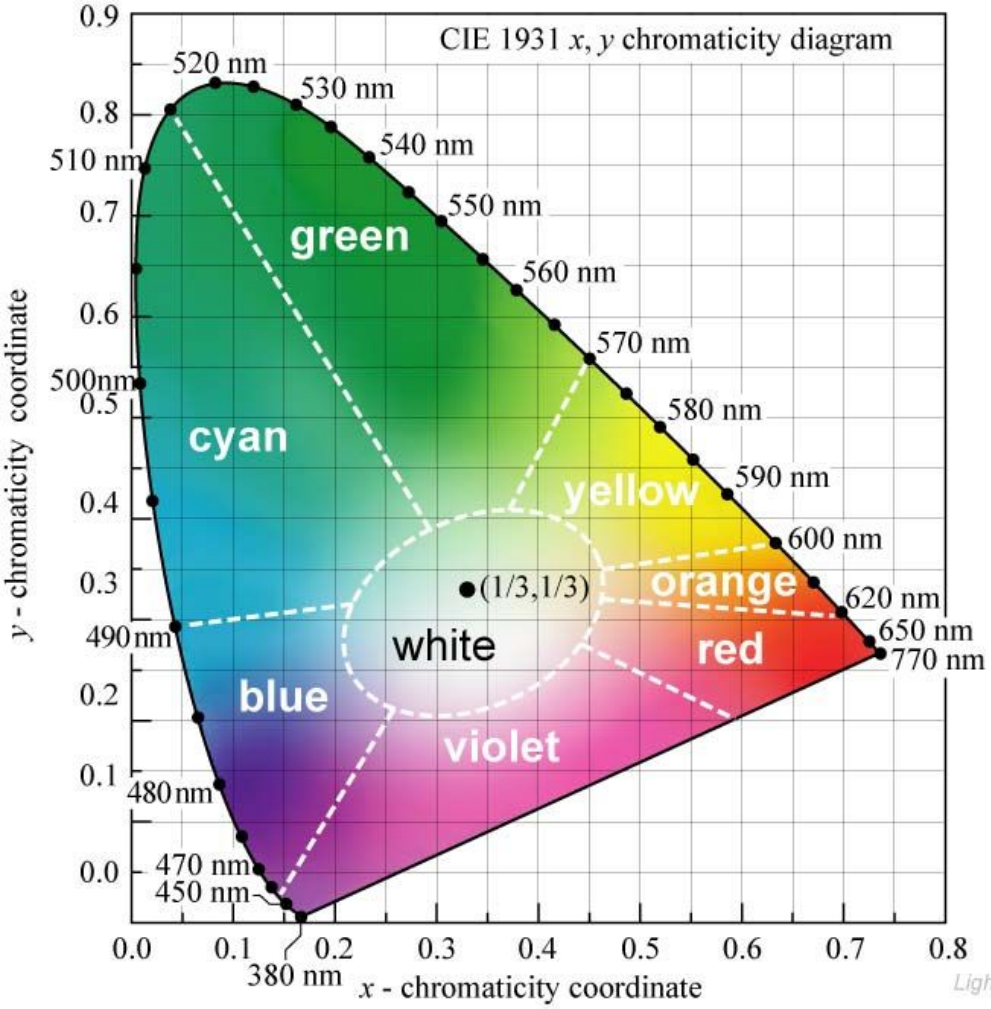

Fig. 17.4. CIE 1931 (x, y) chromaticity diagram. Monochromatic colors are located on the perimeter. Color saturation decreases towards the center of the diagram. White light is located in the center. Also shown are the regions of distinct colors. The equal-energy point is located at the center and has the coordinates (x, y) = (1/3, 1/3).

Color Gamut and Color Mixing

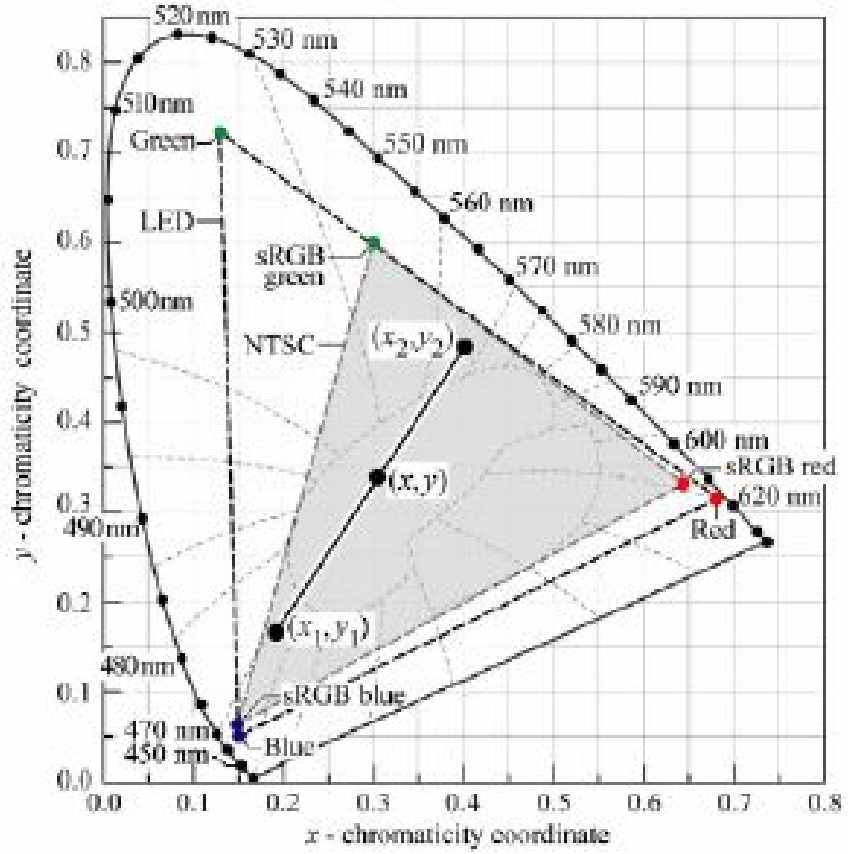

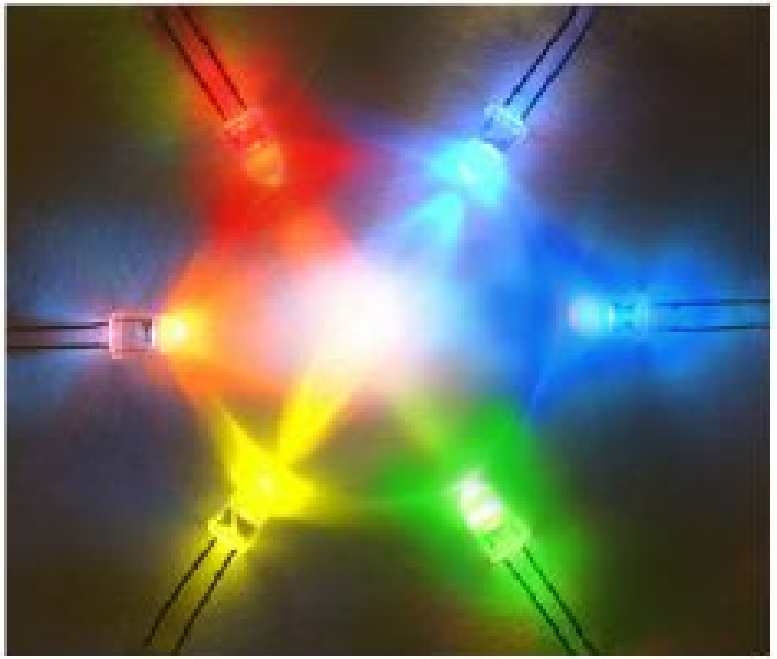

E. F. Shubert
Light Emitting Diodes

- *Color gamut; represents all colors that can be created by mixing primary colors, e.g. red, green, and blue. Webster: n. the entire scale or range*
- *Gamut of Red-Green-Blue light source has triangular shape.*
- *Area of gamut matters for displays, color printers, etc.*

Black-Body Radiation

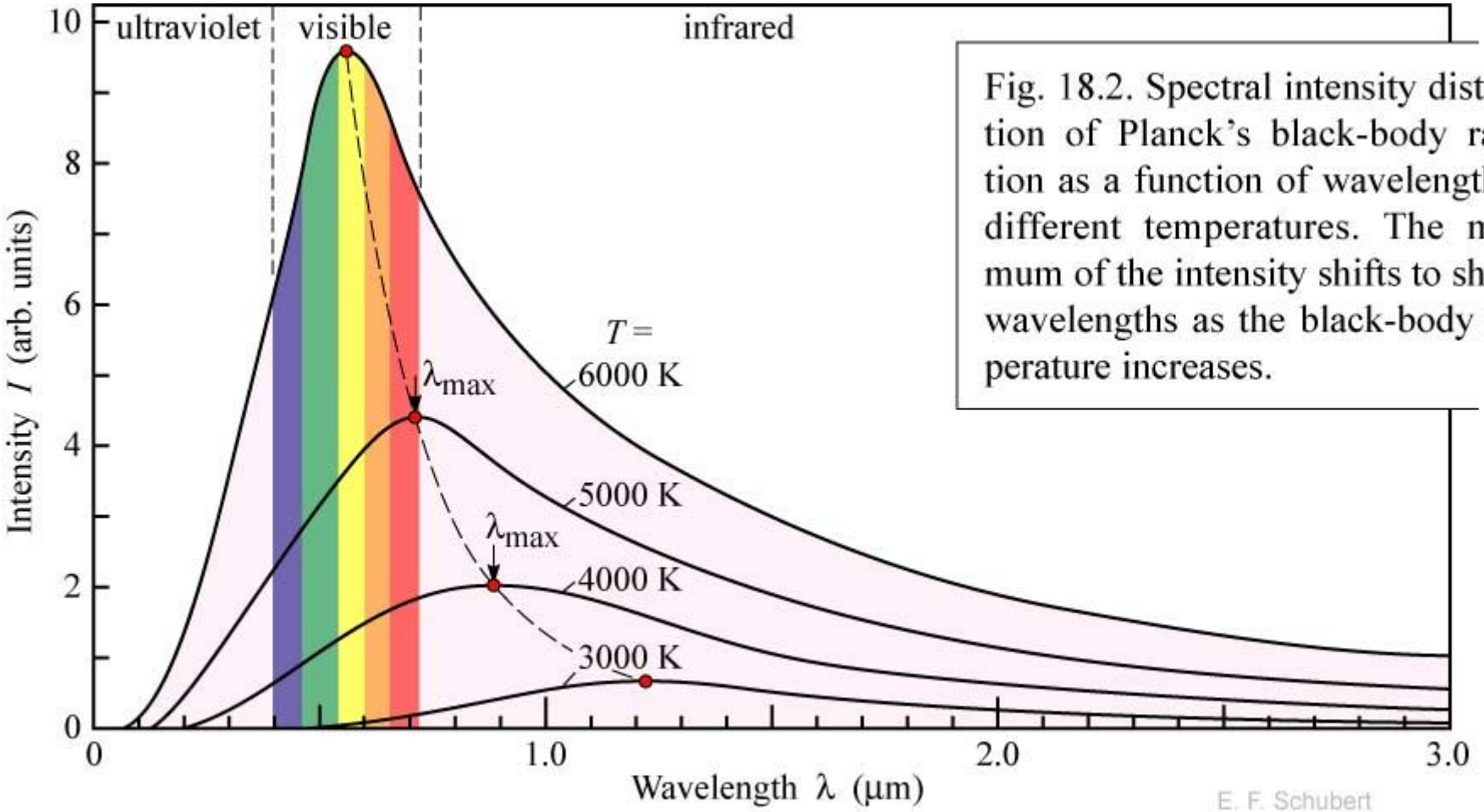

Fig. 18.2. Spectral intensity distribution of Planck's black-body radiation as a function of wavelength for different temperatures. The maximum of the intensity shifts to shorter wavelengths as the black-body temperature increases.

E. F. Schubert
Light-Emitting Diodes (Cambridge Univ. Press)
www.LightEmittingDiodes.org

Temperature of Sun: ~6000 K

White LEDs

LED-Based Approaches

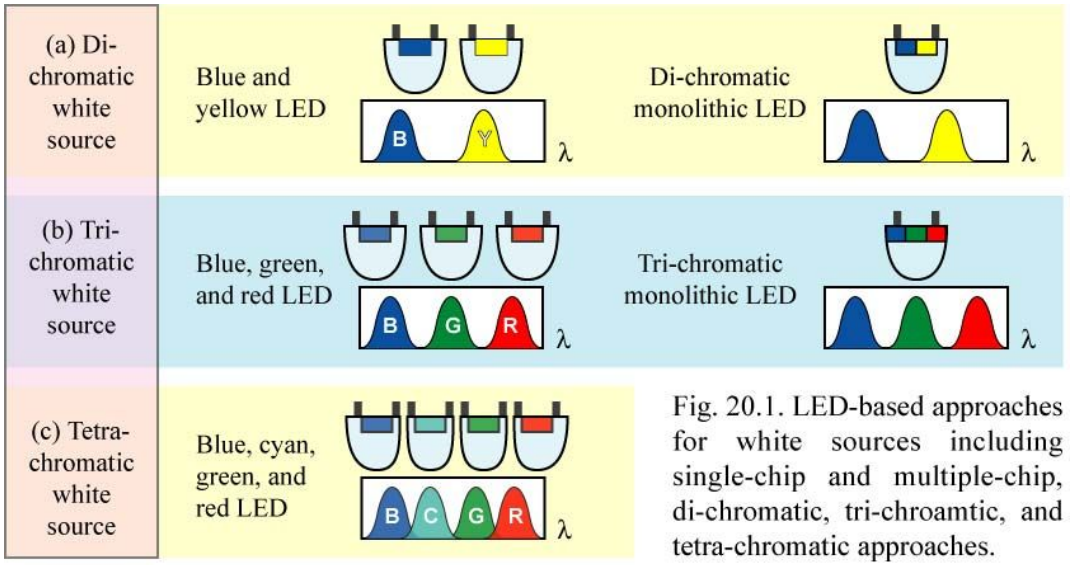

Fig. 20.1. LED-based approaches for white sources including single-chip and multiple-chip, di-chromatic, tri-chroamtic, and tetra-chromatic approaches.

Phosphor-Based Approaches

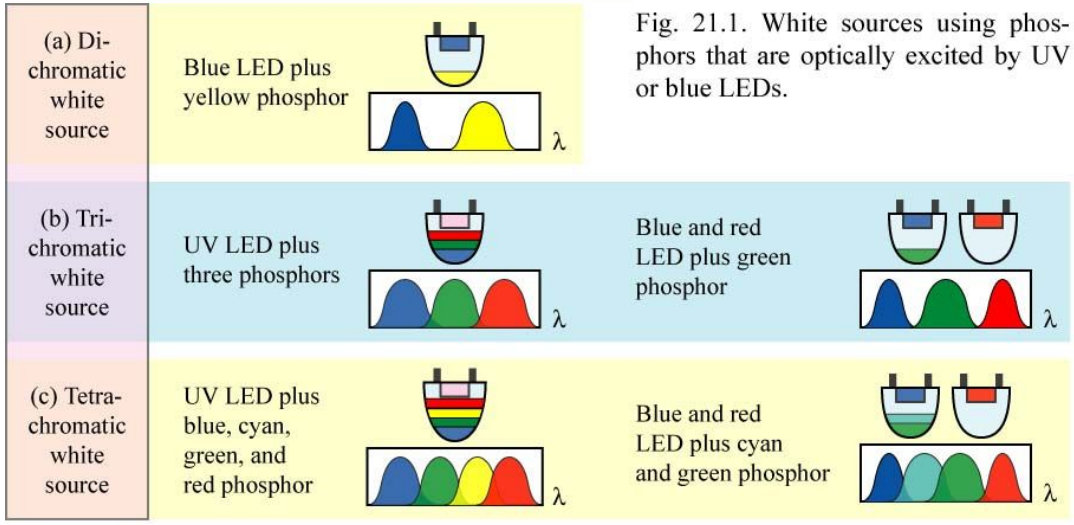

Fig. 21.1. White sources using phosphors that are optically excited by UV or blue LEDs.

Phosphor based approaches: color stability

Dichromatic LED

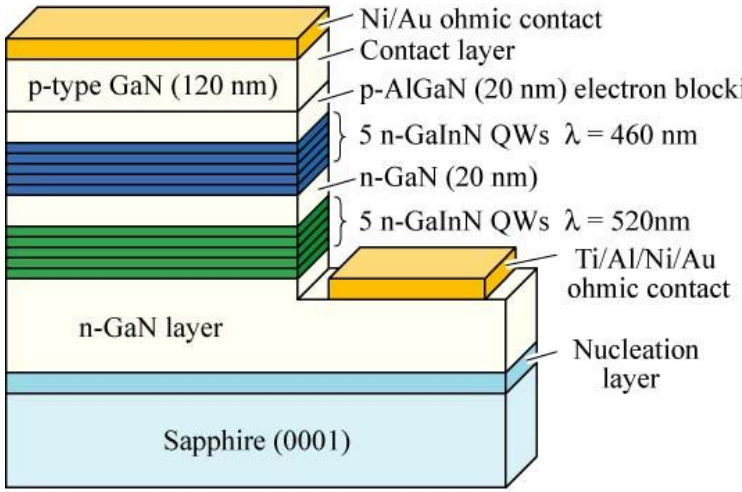

Fig. 20.4. Structure of a monolithic dichromatic LED with two active regions (after Li *et al.*, 2003).

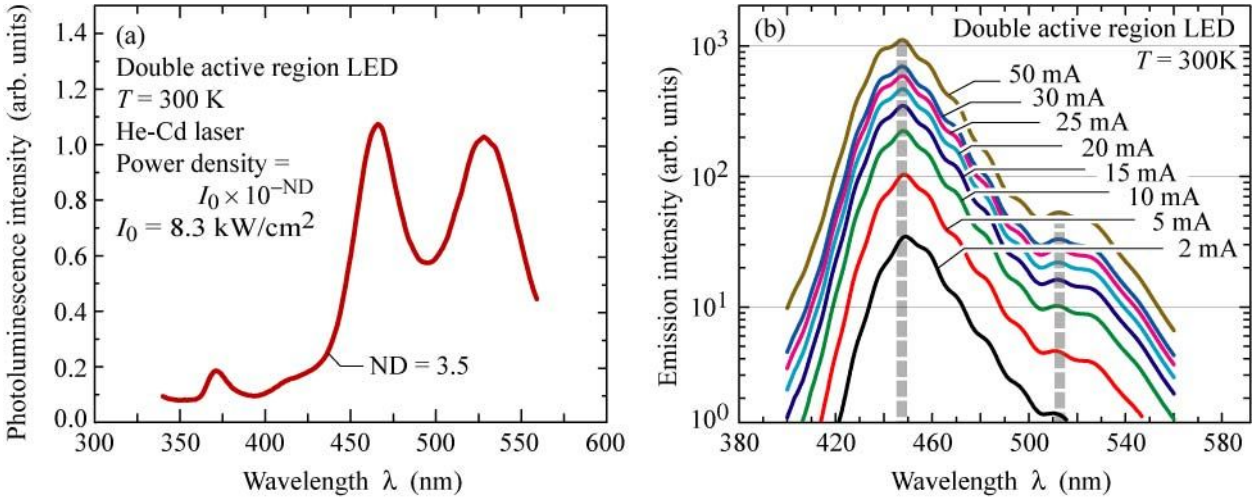

Fig. 20.5. Room temperature (a) photoluminescence and (b) electroluminescence spectra of monolithic dichromatic LED with two active regions (after Li *et al.*, 2003).

Phosphor-Based White LED

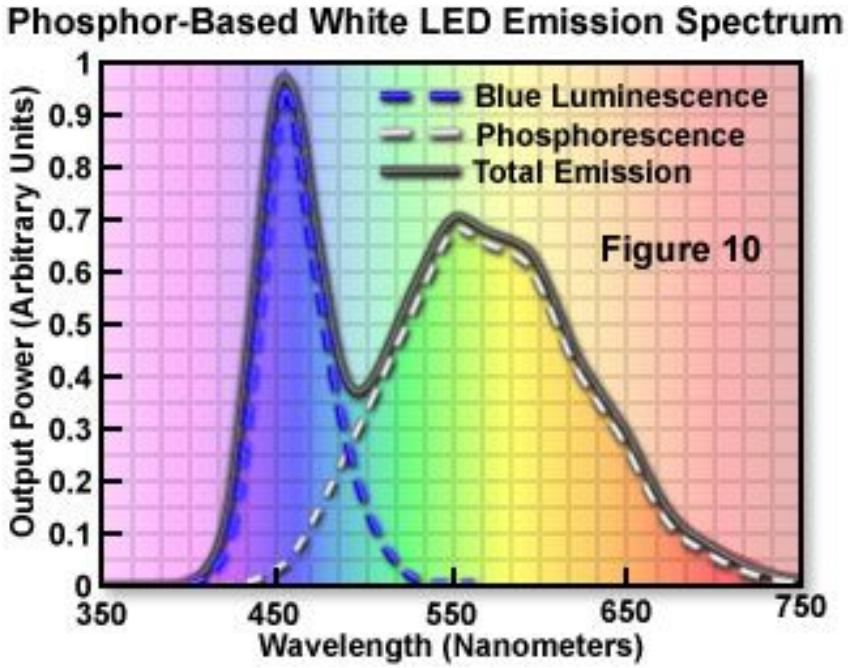

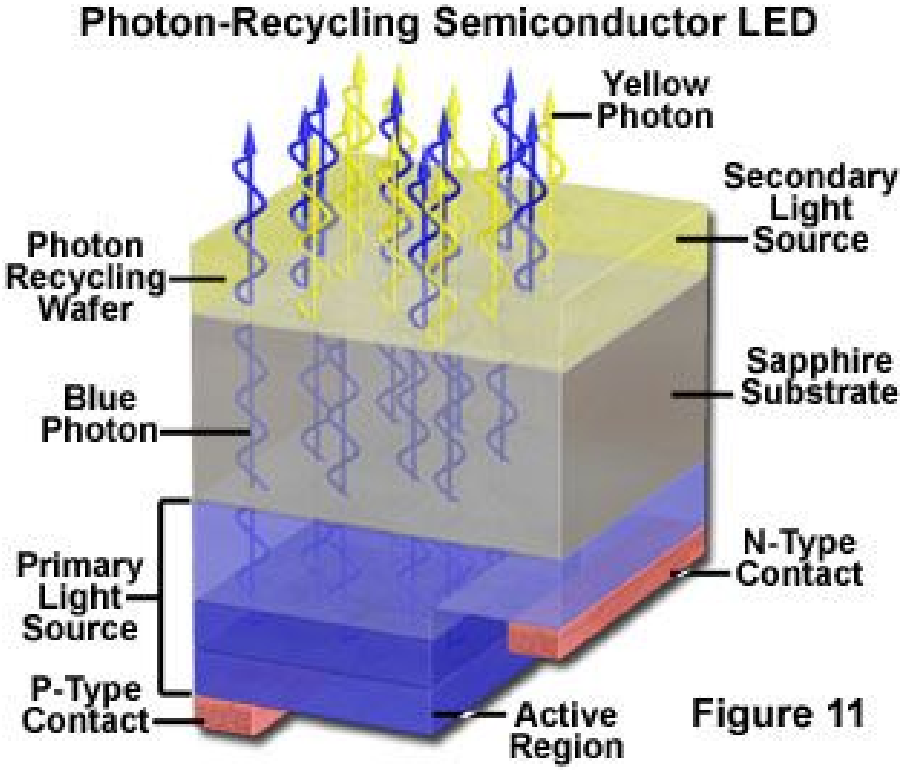

InGaN LED (blue) + YAG Phosphor (yellow)

micro.magnet.fsu.edu

- 2009-11-17

Phosphor-Based White LED

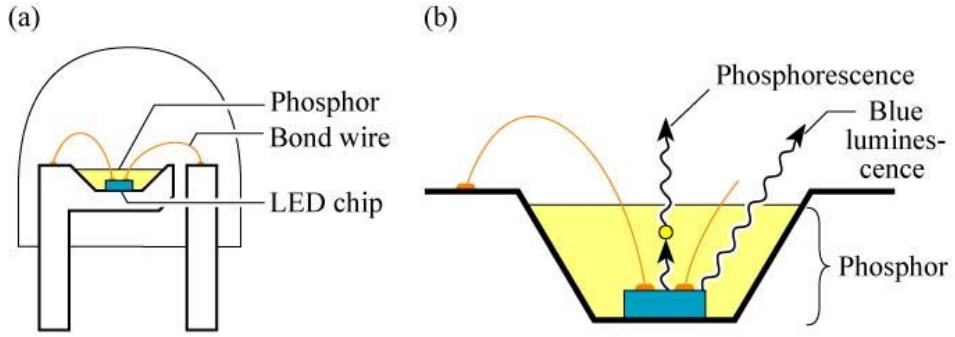

Fig. 21.7. (a) Structure of white LED consisting of a GaInN blue LED chip and a phosphor encapsulating the die. (b) Wavelength-converting phosphorescence and blue luminescence (after Nakamura and Fasol, 1997).

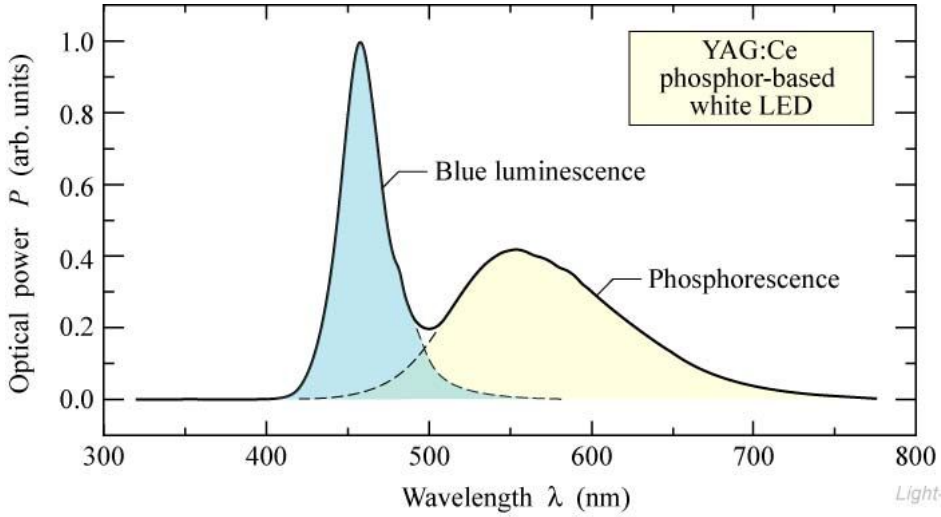

Fig. 21.8. Emission spectrum of a phophor-based white LED manufactured by Nichia Corporation (Anan, Tokushima, Japan).

➔ The thickness of the phosphor-containing epoxy and the concentration of the phosphor suspended in the epoxy determine the relative strengths of the two emission bands.

Photon-Recycling Semiconductor LED

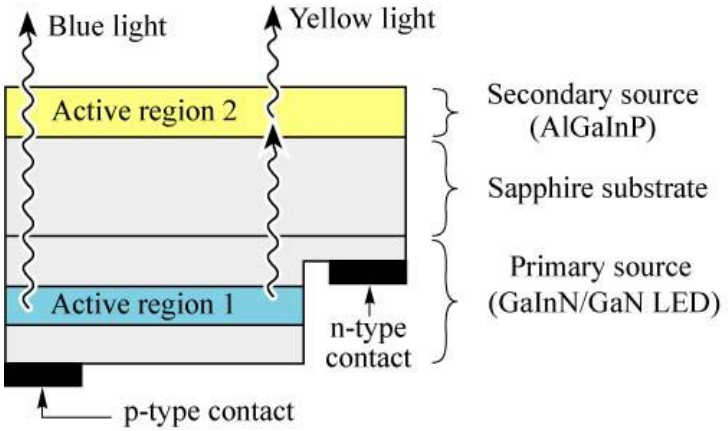

Fig. 21.12. Schematic structure of a photon-recycling semiconductor LED with one current-injected active region (Active region 1) and one optically excited active region (Active region 2) (after Guo *et al.*, 1999).

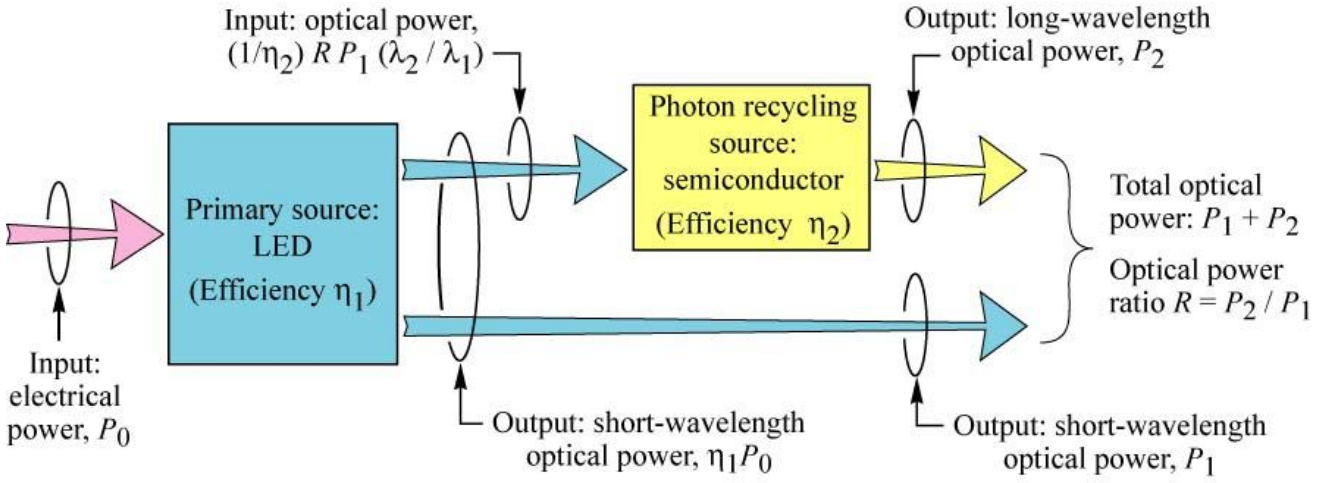

Fig. 21.13. Photon-recycling semiconductor LED power budget with electrical input power P_0 and optical output power P_1 and P_2.

Luminescence

The phenomenon in which electronic states of solids are excited by some energy from an external source, and the excitation energy is released as light.

Luminescence is light not generated by high temperatures alone. It is different from incandescence, in that it usually occurs at low temperatures.

Table 1. Different forms of luminescence.

Luminescence type	Excitation source	Application
cathodoluminescence	electrons	TV sets, monitors
photoluminescence	(UV) photons	fluorescent lamps, plasma displays
X-ray luminescence	X-rays	X-ray amplifier
electroluminescence	electric field	LEDs, EL displays
sonoluminescence	ultrasound	
solvatoluminescence	photons	detectors, analytical devices
chemoluminescence	chemical reaction energy	analytical chemistry
bioluminescence	biochemical reaction energy	analytical chemistry
triboluminescence	mechanical energy	

Thomas Jüstel's Group, Philips Research Laboratories
Angew. Chem. Int. Ed. (1998).

Photoluminescence

- Absorption (Excitation)
- Energy Transfer (Relaxation)
- Emission

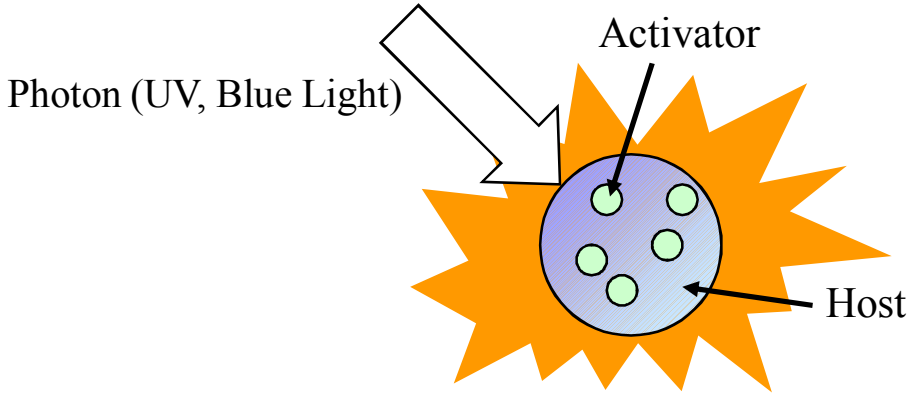

$$\text{Quantum Efficiency } \eta = \frac{\text{number of emitted photons}}{\text{number of absorbed photons}} = \frac{k_{rad}}{k_{rad} + k_{nonrad}}$$

periodic table of the "lighting" elements

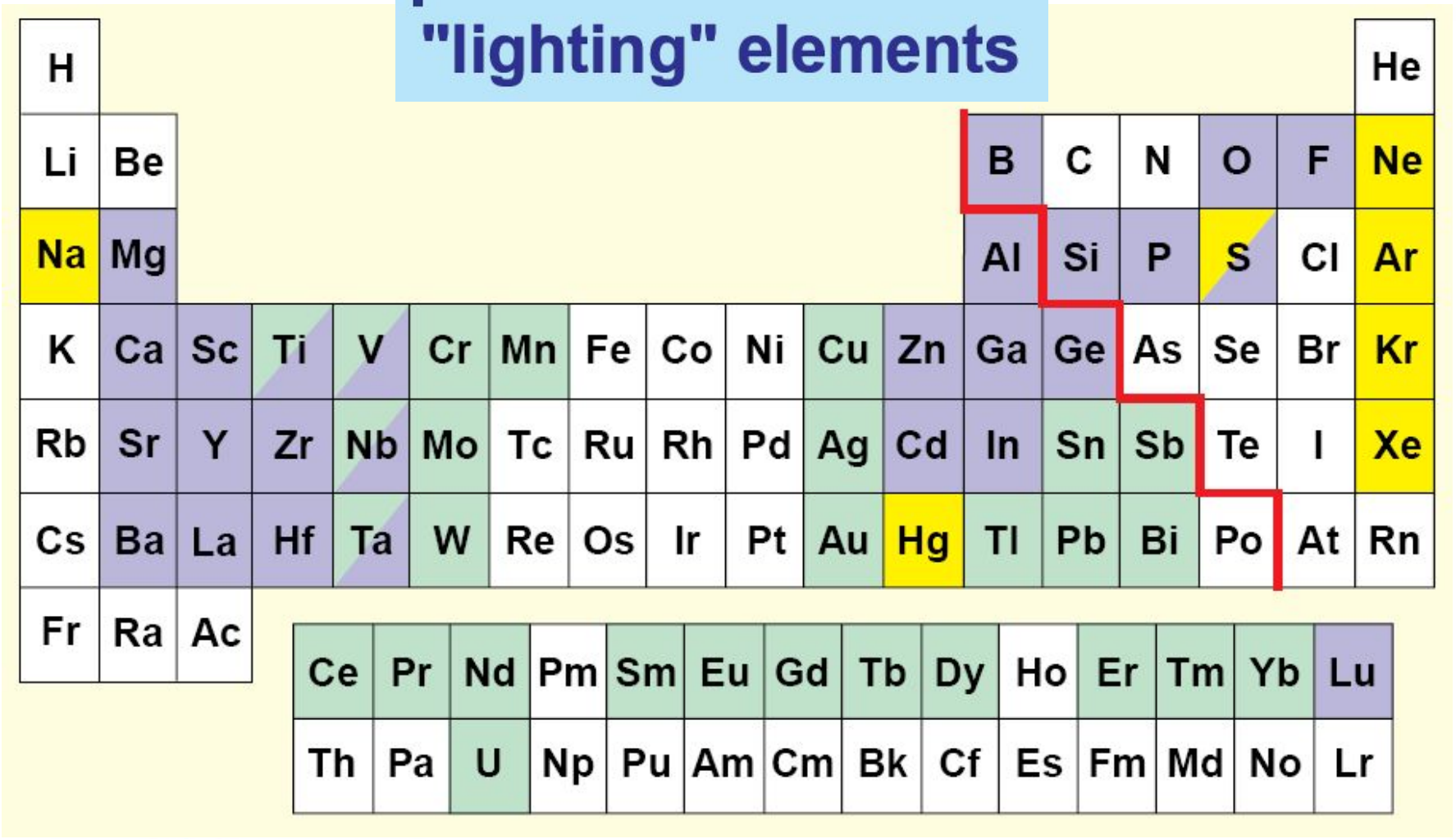

- activator elements
- plasma elements
- host lattice elements

Thomas Jüstel's Group, Philips Research Laboratories
Angew. Chem. Int. Ed. (1998).

New Developments in the Field of Luminescent Materials for Lighting and Displays

Thomas Jüstel,* Hans Nikol,* and Cees Ronda*

While in the seventies and eighties the field of luminescent materials seemed to be fairly well covered, research in the nineties has been revitalized both in industry and academia. Improved performance of allegedly mature "classical" materials has demonstrated impressively the role of until then often neglected parameters such as surface and particle properties. In a business as developed as the lamp market new lamp features such as reduced mercury consumption can lead to a competitive edge and new phosphor research programs. Quantum cutter phosphors that generate two visible photons from one UV photon are the focus of research again, for example, for plasma display panels as huge flat and thin hang-on-the-wall TVs. Promising new developments such as electroluminescent full-color displays or the blue (laser) diode have created excitement and numerous research efforts in laboratories around the world. The direct conversion of electricity into light, common to both applications, challenges current concepts and might eventually revolutionize the way we illuminate rooms, car lights, or traffic signals, and how we display video information. A deep understanding of the interaction of light and matter together with advanced material chemistry is the key to both improved and new lighting and display products.

Keywords: displays · fluorescence · luminescence · materials science · rare-earth compounds

Thomas Jüstel's Group, Philips Research Laboratories
Angew. Chem. Int. Ed. (1998).

Radiative Recombination and Nonradiative Recombination

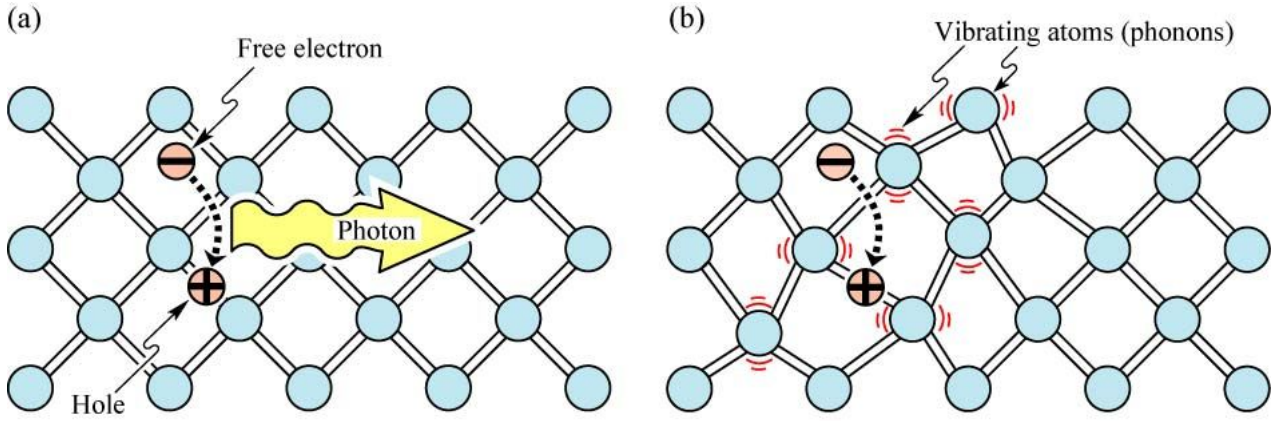

Fig. 2.5. (a) Radiative recombination of an electron-hole pair accompanied by the emission of a photon with energy $h\nu \approx E_g$. (b) In non-radiative recombination events, the energy released during the electron-hole recombination is converted to phonons (adopted from Shockley, 1950).

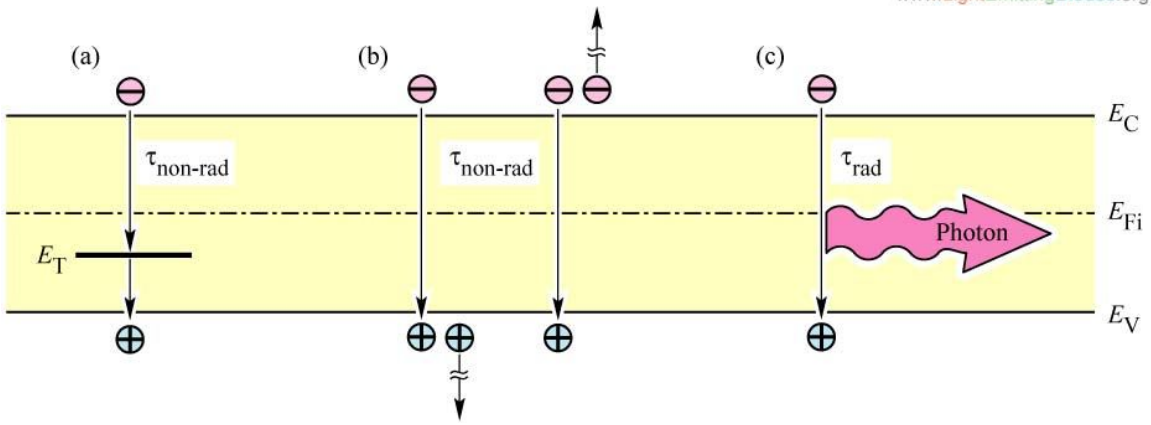

Fig. 2.6. Band diagram illustrating non-radiative recombination: (a) via a deep level, (b) via an Auger process and (c) radiative recombination.

Bandgap Energy for Semiconductors

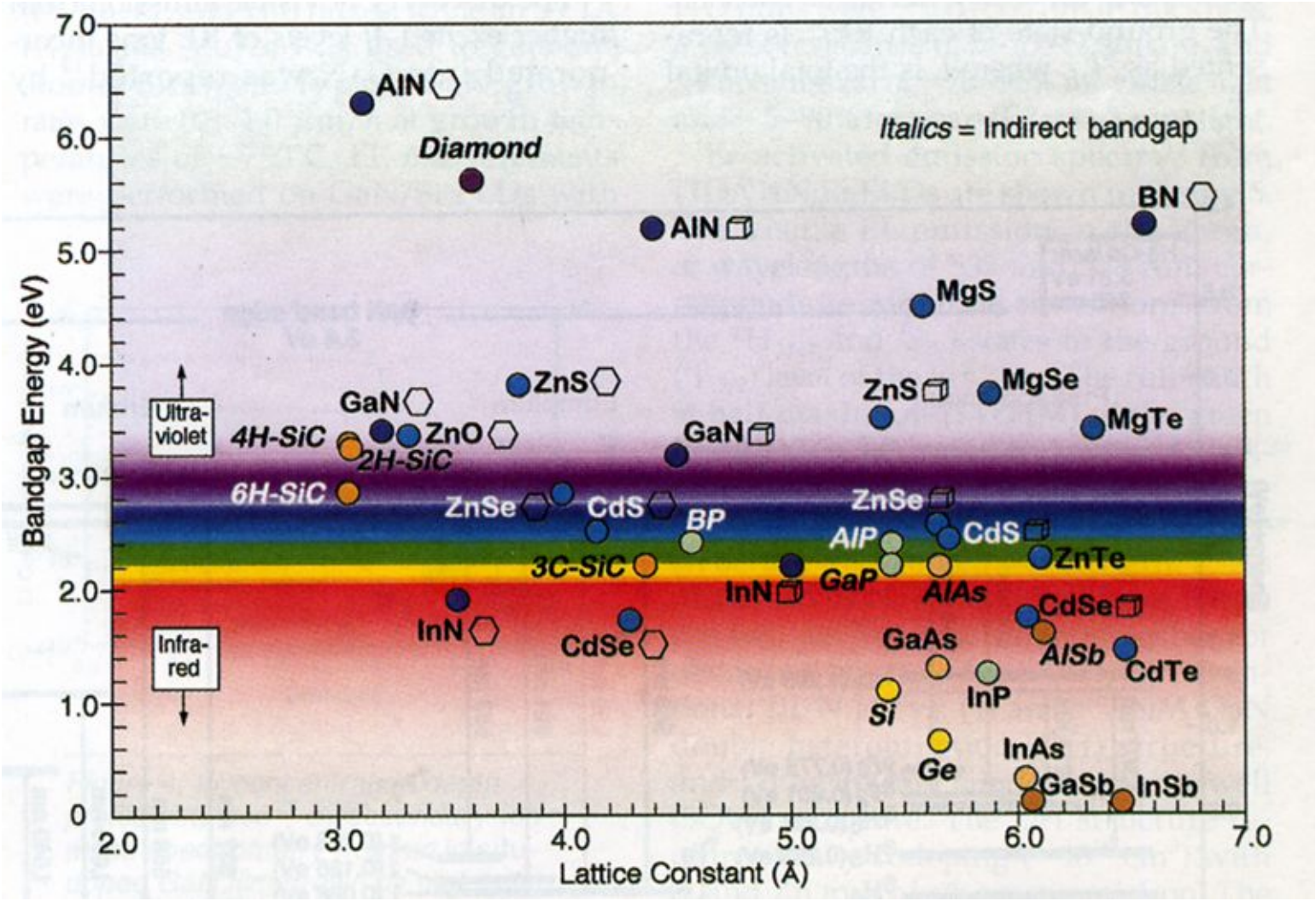

MRS Bulletin (1999)

Direct Band Gap and Indirect Band Gap

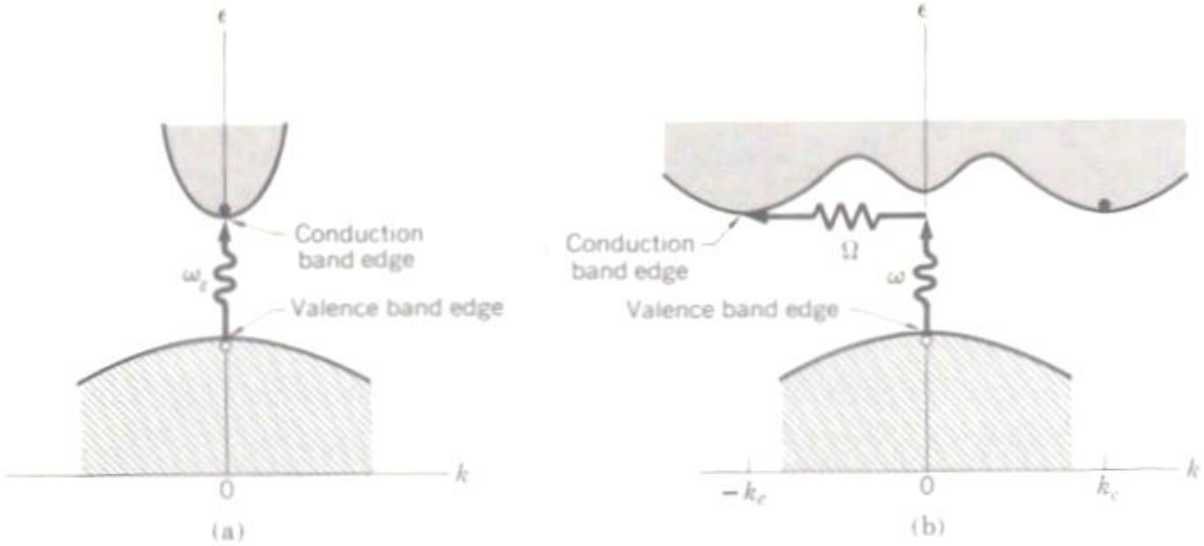

Figure 5 In (a) the lowest point of the conduction band occurs at the same value of **k** as the highest point of the valence band. A direct optical transition is drawn vertically with no significant change of **k**, because the absorbed photon has a very small wavevector. The threshold frequency ω_g for absorption by the direct transition determines the energy gap $E_g = \hbar\omega_g$. The indirect transition in (b) involves both a photon and a phonon because the band edges of the conduction and valence bands are widely separated in **k** space. The threshold energy for the indirect process in (b) is greater than the true band gap. The absorption threshold for the indirect transition between the band edges is at $\hbar\omega = E_g + \hbar\Omega$, where Ω is the frequency of an emitted *phonon* of wavevector $\mathbf{K} = -\mathbf{k}_c$. At higher temperatures phonons are already present; if a phonon is absorbed along with a photon, the threshold energy is $\hbar\omega = E_g - \hbar\Omega$. *Note:* The figure shows only the threshold transitions. Transitions occur generally between almost all points of the two bands for which the wavevectors and energy can be conserved.

C. Kittel
Introduction to Solid State Physics

Measurement of Absolute Quantum Efficiency

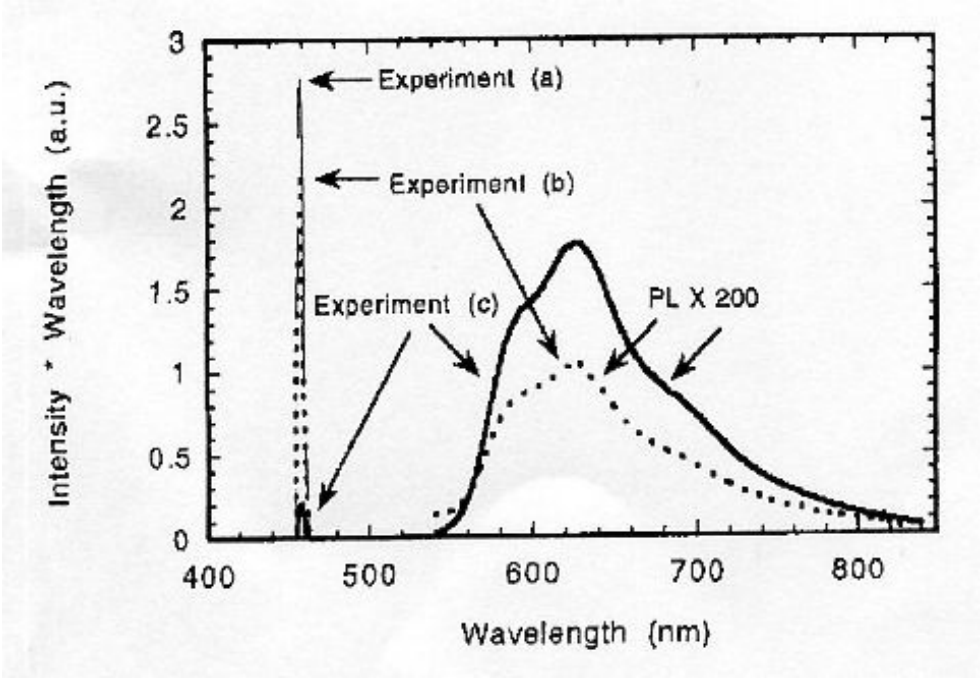

MEH-PPV thin film

$N = N_{\Omega}(4\pi/\Omega)$

➔ Integrating sphere

Fig. 2. The complete spectra for the measurement of a thin film of MEH PPV. The PL spectra have been enlarged by a factor of 200 for clarity.

Friend's Group, Cambridge University
Adv. Mater. (1997).

Measurement of Absolute Quantum Efficiency

$L_b = L_a(1 - \mu)$
$L_c = L_a(1 - A)(1 - \mu)$
➔ $A = (1 - L_c / L_a)$

$L_c + L_a = (1 - A)(L_b + P_b) + \eta L_a A$
➔ $\eta = \{P_c - (1 - A)P_b\} / L_a A$

L : # of photons in laser region
P : # of photons in PL region
μ : sample absorption of scattered light from sphere
A : sample absorption of incident light

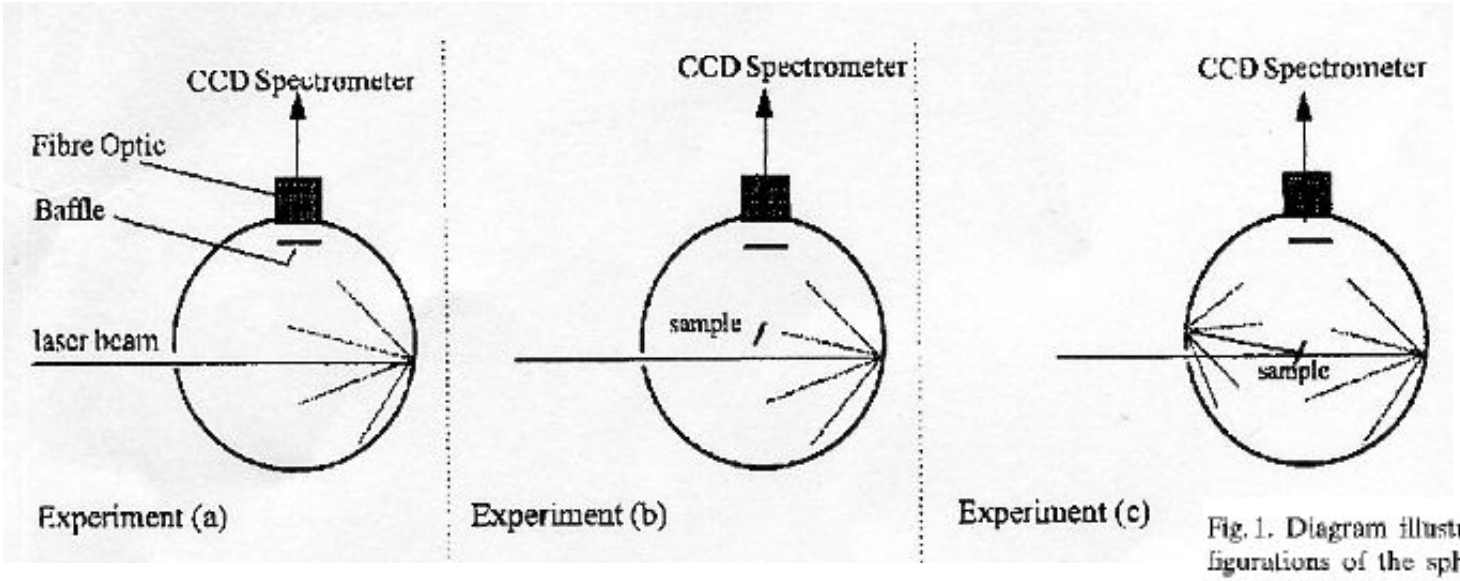

Fig. 1. Diagram illustrating the three configurations of the sphere required for the efficiency measurement: a) the sphere is empty; b) the sample is in place and the laser beam is directed onto the sphere wall; c) the sample is in place and the laser beam is directed onto the sample.

Friend's Group, Cambridge University
Adv. Mater. (1997).

Term Symbol

$^{2S+1}L_J$

S : total spin quantum number (spin-up : s = +1/2, spin-down : s = –1/2)

L : total orbital quantum number (L = 0,1,2,3,4,5,…. ➔ S,P,D,F,G,H,…)

J : total angular momentum quantum number (J = L +S)

ex) F : $1s^2 2s^2 2p^5$

	m_l		
	+1	0	−1
m_s	↑↓	↑↓	↑

S = +1/2

L = 1

J = 3/2, 1/2

∴ F의 Ground State에서의 Term Symbol은 $^2P_{3/2}$

Term Symbol

Ex) Eu : $[Xe]4f^7 5d^0 6s^2$

Eu^{3+} : $[Xe]4f^6$

Eu^{3+}

	m_l						
	+3	+2	+1	0	−1	−2	−3
m_s	↑	↑	↑	↑	↑	↑	

L=3, S=3

∴ $^7F_0$, $^7F_1$, $^7F_2$, $^7F_3$, $^7F_4$, $^7F_5$, $^7F_6$

Eu^{3+}

	m_l						
	+3	+2	+1	0	−1	−2	−3
m_s		↑↓	↑	↑	↑	↑	

L=2, S=2

∴ $^5D_0$, $^5D_1$, $^5D_2$, $^5D_3$, $^5D_4$

Energy Level Diagrams for Rare-Earth Elements

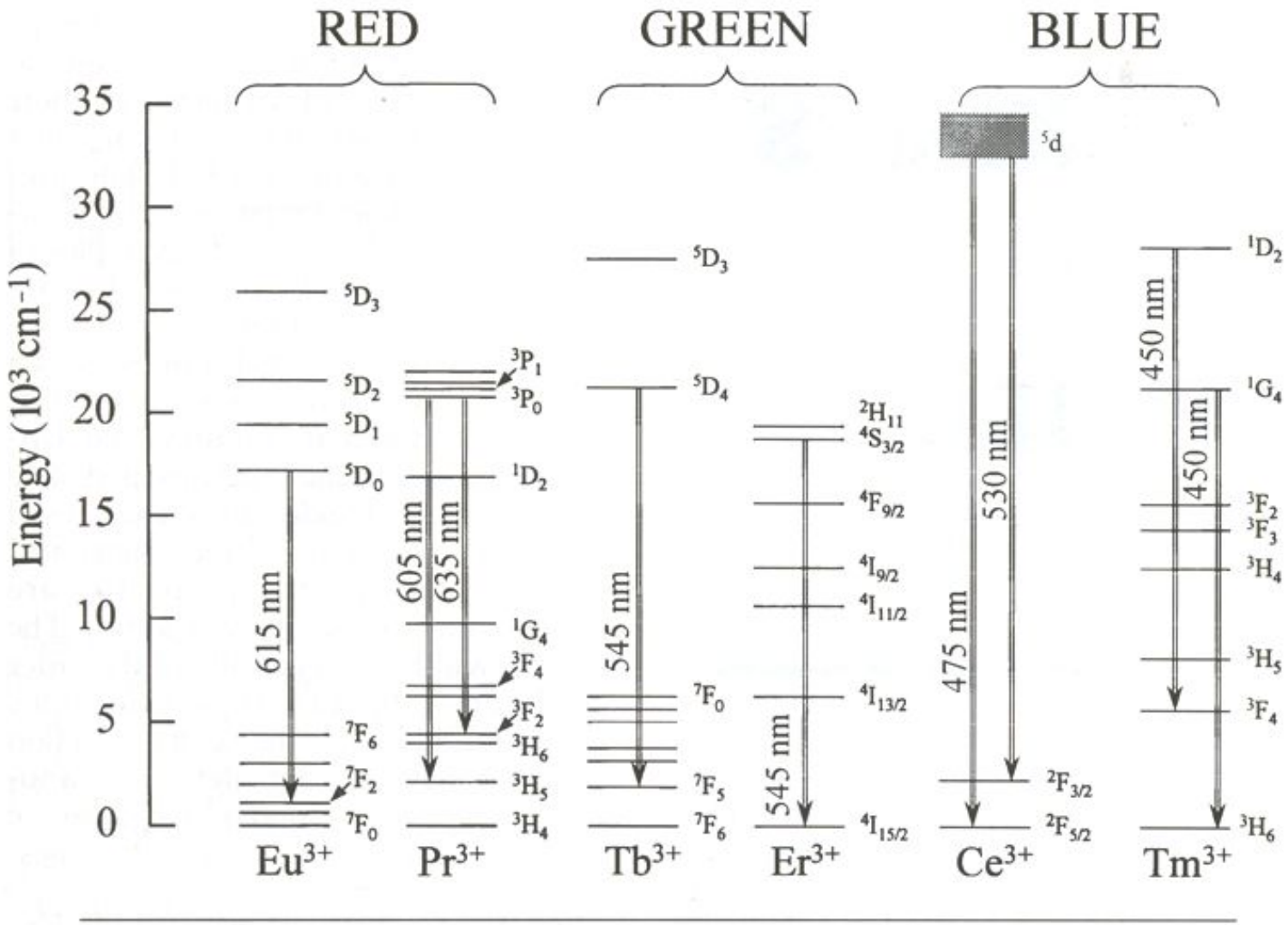

Figure 1. Energy-level diagrams for rare-earth elements emitting in the visible.

Energy Diagram of Mn^{2+} Ion ($^4T_1$ - $^6A_1$ Transition)

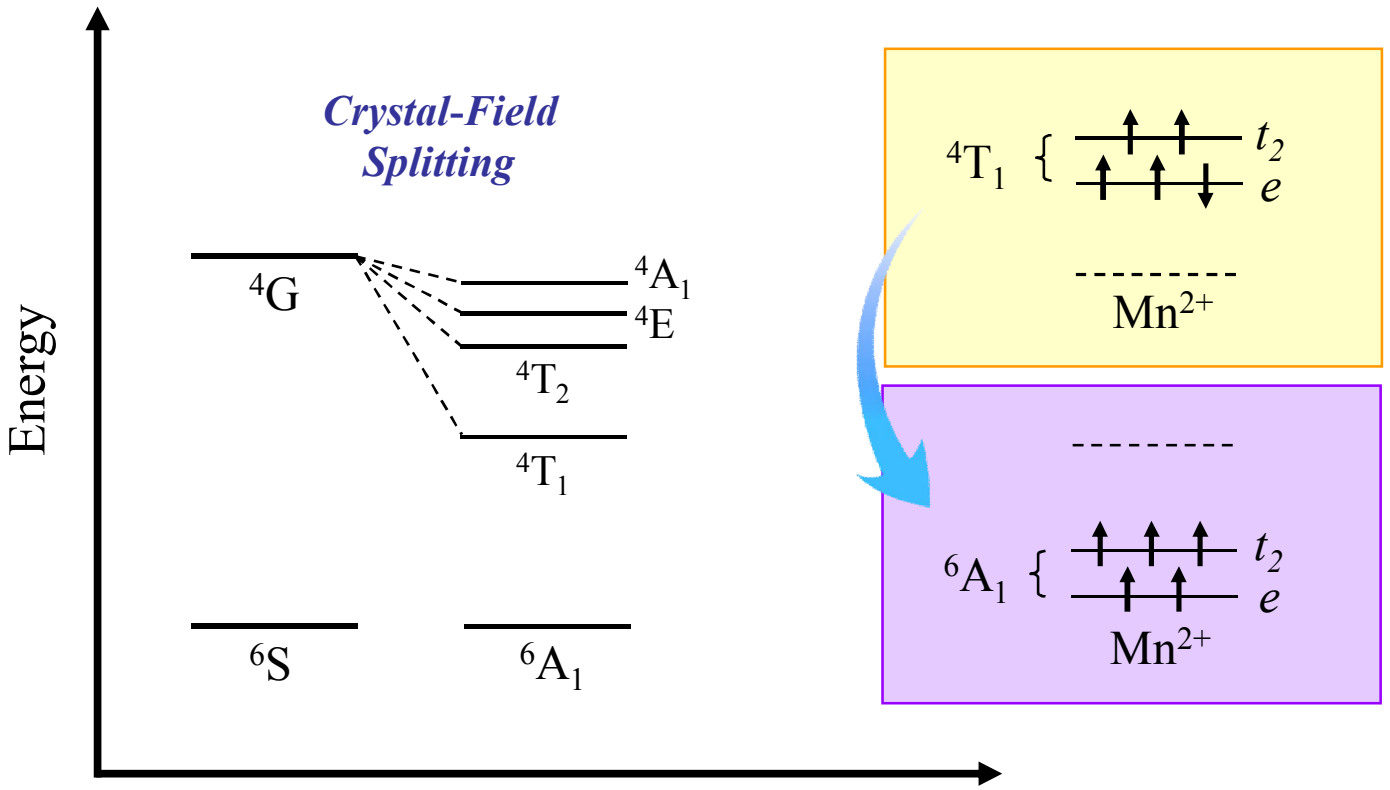

- **Characteristic emission of Mn^{2+} ions: $^4T_1$ (excited) – $^6A_1$ (ground)**

Electronic Structure of $CePO_4$

254 nm excitation

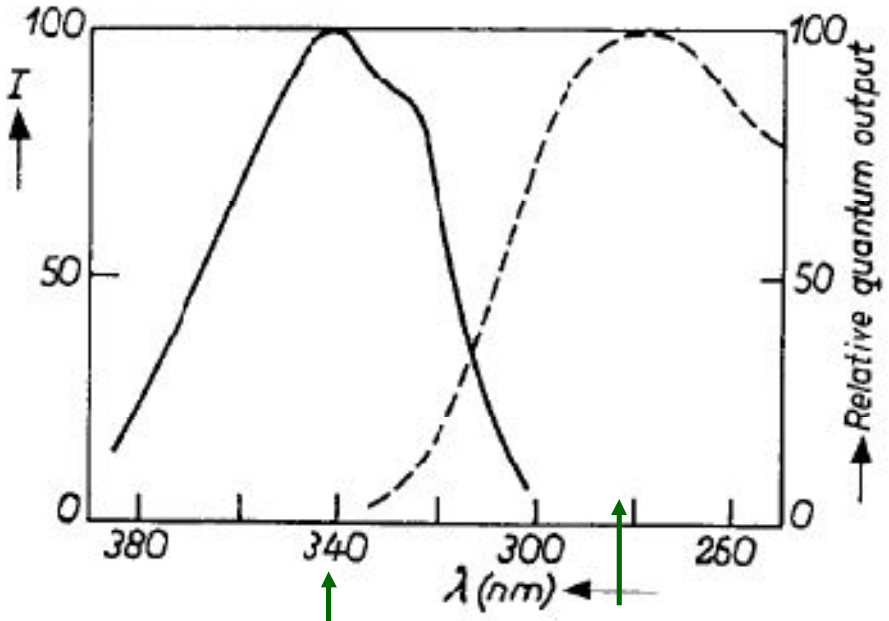

FIG. 2. Emission of $CePO_4$ and excitation of $CePO_4$ and $Ce_{0.95}Tb_{0.05}PO_4$. For details see caption to Fig. 1.

TABLE I. Quantum efficiencies q for excitation into the lowest Ce^{3+} absorption level.

Composition	q(%) Ce^{3+} emission	q(%) Tb^{3+} emission
$La_{0.99}Ce_{0.01}F_3$	50	...
$La_{0.95}Ce_{0.05}F_3$	50	...
$La_{0.8}Ce_{0.2}F_3$	50	...
$La_{0.5}Ce_{0.5}F_3$	50	...
$La_{0.2}Ce_{0.8}F_3$	50	...
CeF_3	50	...
$Ce_{0.99}Tb_{0.01}F_3$	40	10
$Ce_{0.95}Tb_{0.05}F_3$	20	30
$Ce_{0.9}Tb_{0.1}F_3$	10	40
$Ce_{0.8}Tb_{0.2}F_3$	<5	50
$La_{0.99}Ce_{0.01}PO_4$	60	...
$La_{0.95}Ce_{0.05}PO_4$	50	...
$La_{0.9}Ce_{0.1}PO_4$	45	...
$CePO_4$	40	...
$Ce_{0.99}Tb_{0.01}PO_4$	15	35
$Ce_{0.95}Tb_{0.05}PO_4$	<5	50
$La_{0.99}Ce_{0.01}BO_3$	40	...
$La_{0.95}Ce_{0.05}BO_3$	35	...
$La_{0.9}Ce_{0.1}BO_3$	30	...
$CeBO_3$	15	...
$Ce_{0.99}Tb_{0.01}BO_3$	<5	40
$La_{0.99}Ce_{0.01}AlO_3$	<5	...
$CeAlO_3$	<5	...
$Ce_{0.99}Tb_{0.01}AlO_3$	<5	<5

G. Blasse and A. Bril, Philips Research Laboratories
J. Chem. Phys. (1969)

THE JOURNAL OF CHEMICAL PHYSICS VOLUME 51, NUMBER 8 15 OCTOBER 1969

Energy Transfer in Tb^{3+}-Activated Cerium(III) Compounds

G. BLASSE AND A. BRIL

Philips Research Laboratories, N. V. Philips' Gloeilampenfabrieken, Eindhoven, Netherlands

(Received 30 June 1969)

The luminescence of Tb^{3+}-activated CeF_3, $CePO_4$, $CeBO_3$, and $CeAlO_3$ has been investigated. Energy transfer from the Ce^{3+} host lattice to the Tb^{3+} ion occurs by Ce^{3+}–Ce^{3+} and Ce^{3+}–Tb^{3+} transfer. From a study of the Ce^{3+} luminescence in the analogous La compounds it can be concluded that the probability of the former transfer is different for these host lattices. An analogy with Eu^{3+}-activated host lattices is pointed out.

I. INTRODUCTION

The Tb^{3+} ion is known to be an efficient activator in several host lattices. This paper reports on some Tb^{3+}-activated cerium(III) compounds. It may be expected that ultraviolet radiation is absorbed by the Ce^{3+} ions,[1] followed by $Ce^{3+}\rightarrow Ce^{3+}$ energy transfer and finally by $Ce^{3+}\rightarrow Tb^{3+}$ energy transfer. Energy transfer from Ce^{3+} to Ce^{3+} has been considered by Botden[2] and ourselves and occurs over distances of 15–20 Å.[3,4] Energy transfer from Ce^{3+} to Tb^{3+} has been observed for many host lattices, e.g., $Ca(PO_3)_2$[5] and yttrium compounds.[3] Recently Denis and Loriers[6] described the efficient fluorescence of $CePO_4$–Tb. The energy processes in phosphors of this type will be described in this paper.

Optical measurements were performed as described previously.[7] The quantum efficiency of the ultraviolet emission of the samples $La_{1-x}Ce_xF_3$ $(0<x\leq 1)$ was measured by using a cadmium vapor discharge lamp as the excitation source. With the aid of a combination of a chlorine gas filter (4 cm, 1 atm pressure) and a Barr and Stroud broad-band interference filter peaking at 229 nm, mainly 228.8-nm radiation was isolated from the emission of the lamp. The fluorescence radiation passed a 0.8-cm Schott WG8 filter in order to absorb the reflected ultraviolet excitation radiation.

III. RESULTS

The Tb^{3+} fluorescence was studied in the following Ce^{3+} compounds: CeF_3, $CePO_4$, $CeBO_3$, $CeAlO_3$. We also

Even if the quantum efficiency of a phosphor is over 100%, the energy conversion efficiency is lower than 100%!

Visible Quantum Cutting in $LiGdF_4:Eu^{3+}$ Through Downconversion

René T. Wegh, Harry Donker, Koenraad D. Oskam, Andries Meijerink*

For mercury-free fluorescent lamps and plasma display panels, alternative luminescent materials are required for the efficient conversion of vacuum ultraviolet radiation to visible light. Quantum cutting involving the emission of two visible photons for each vacuum ultraviolet photon absorbed is demonstrated in Eu^{3+}-doped $LiGdF_4$ with the concept of downconversion. Upon excitation of Gd^{3+} with a high-energy photon, two visible photons can be emitted by Eu^{3+} through an efficient two-step energy transfer from Gd^{3+} to Eu^{3+}, with a quantum efficiency that approaches 200 percent.

Meijerink's Group, Utrecht University, Netherlands
Science (1999).

Quantum Cutting ($LiGdF_4:Eu^{3+}$)

Meijerink's Group, Utrecht University, Netherlands
Science (1999).

Proposed Mechanisms of Quantum Cutting

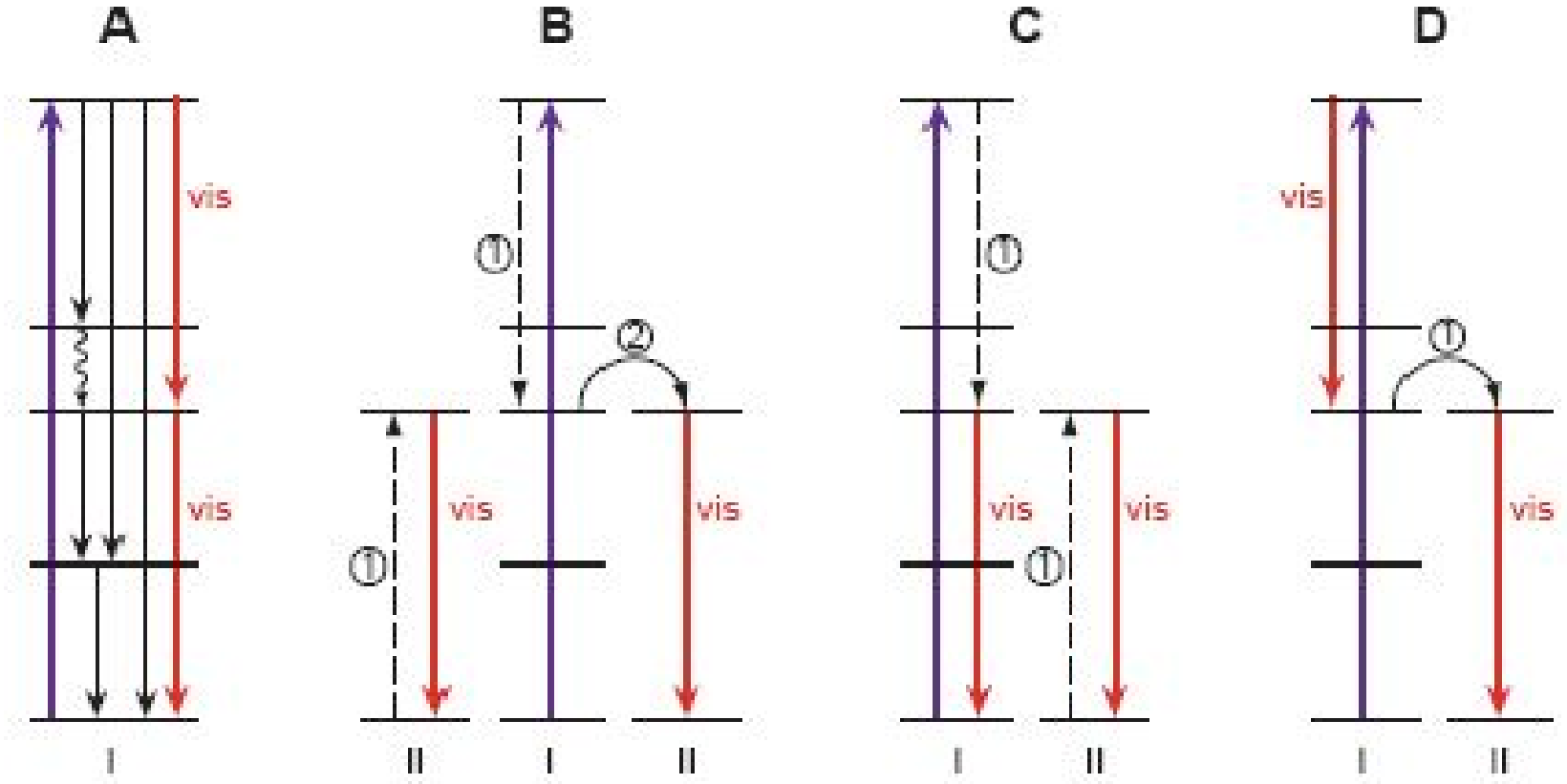

Fig. 1 (left). Energy level diagrams for two (hypothetical) types of lanthanide ions (I and II), showing the concept of downconversion. Type I is an ion for which emission from a high energy level can occur. Type II is an ion to which energy transfer takes place. (**A**) Quantum cutting on a single ion I by the sequential emission of two visible photons. (**B**) The possibility of quantum cutting by a two-step energy transfer. In the first step (indicated by ①), a part of the excitation energy is transferred from ion I to ion II by cross-relaxation. Ion II returns to the ground state by emitting one photon of visible light. Ion I is still in an excited state and can transfer the remaining energy to a second ion of type II (indicated by ②), which also emits a photon in the visible spectral region, giving a quantum efficiency of 200%. (**C** and **D**) The remaining two possibilities involve only one energy transfer step from ion I to ion II. This is sufficient to obtain visible quantum cutting if one of the two visible photons can be emitted by ion I. **Fig. 2 (right).** Energy level diagram of the Gd^{3+}-Eu^{3+} system, showing the possibility of visible quantum cutting by a two-step energy transfer from Gd^{3+} to Eu^{3+}.

Quantum Cutting ($LiGdF_4:Eu^{3+}$) Gadolinium -> Europium

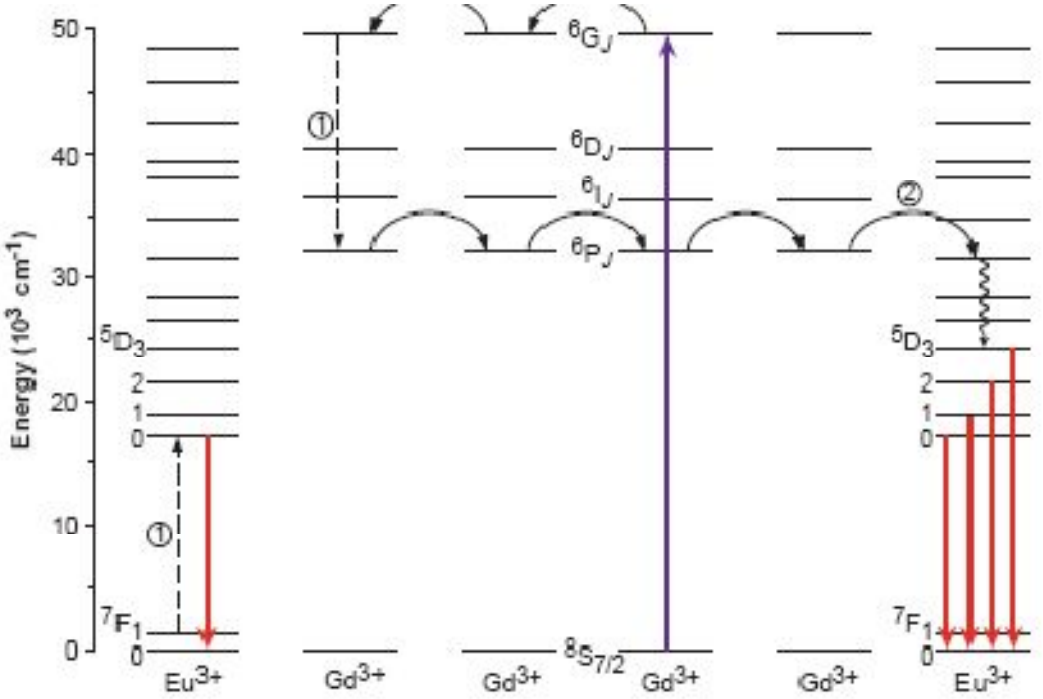

in the visible spectral region, giving a quantum efficiency of 200%. (**C** and **D**) The remaining two possibilities involve only one energy transfer step from ion I to ion II. This is sufficient to obtain visible quantum cutting if one of the two visible photons can be emitted by ion I. **Fig. 2 (right).** Energy level diagram of the Gd^{3+}-Eu^{3+} system, showing the possibility of visible quantum cutting by a two-step energy transfer from Gd^{3+} to Eu^{3+}.

Meijerink's Group, Utrecht University, Netherlands
Science (1999).

Quantum Cutting ($LiGdF_4:Eu^{3+}$)

PL Spectra

PLE Spectra

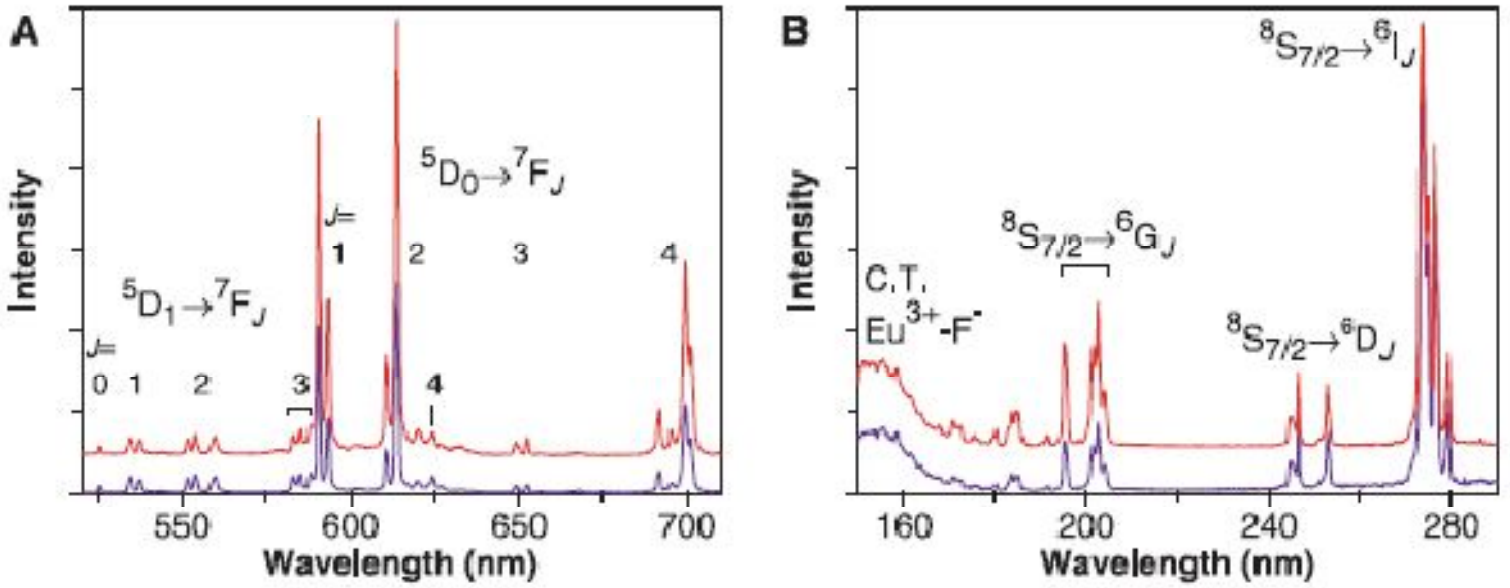

Fig. 3. (A) Emission spectra of $LiGdF_4:Eu^{3+}$ (0.5 mol%) upon excitation in the ^6I_J levels of Gd^{3+} at 273 nm (violet line) and upon excitation in the ^6G_J levels of Gd^{3+} at 202 nm (red line), both at 300 K. The spectra are scaled on the $^5D_1 \rightarrow {}^7F_J$ emission intensity. (B) Excitation spectra of $LiGdF_4:Eu^{3+}$ (0.5 mol%) monitoring the $^5D_1 \rightarrow {}^7F_2$ emission of Eu^{3+} at 554 nm (violet line) and the $^5D_0 \rightarrow {}^7F_2$ emission at 614 nm (red line), both at 300 K. The spectra are scaled on the $^8S_{7/2} \rightarrow {}^6I_J$ excitation intensity.

Meijerink's Group, Utrecht University, Netherlands
Science (1999).

A Quantum-Splitting Phosphor Exploiting the Energy Transfer from Anion Excitons to Tb^{3+} in $CaSO_4$:Tb,Na**

By *Arunachalam R. Lakshmanan, Seon-Bae Kim, Hyun M. Jang,* Byung G. Kum, Bong K. Kang, Soonyeong Heo,* and *Dongsung Seo*

Wide-bandgap materials doped with rare-earth ions are currently of great interest as new vacuum ultraviolet (VUV) phosphors for lighting and displays. This paper reports the development of a highly sensitive green phosphor, $CaSO_4$:Tb,Na, which exhibits a quantum efficiency higher than 100 % by exploiting the energy-transfer mechanism from anion excitons to the activator ions, Tb^{3+}. The VUV excitation spectra of $CaSO_4$:Tb^{3+} with Na^+ as a charge compensator show two prominent excitation bands at 147 and 216 nm. The former band is attributed to the charge-transfer excitations within SO_4^{2-} complexes while the latter was assigned to the $4f^8 \rightarrow 4f^75d$ transitions on Tb^{3+}. The energy-transfer mechanism from anion excitons to Tb^{3+} strongly raises the possibility of two-photon emission via a second-order down-conversion under the VUV excitation, which is basically a new approach in the goal of achieving a quantum-splitting phosphor.

Hyun M. Jang's Group, Postech
Adv. Funct. Mater. (2007).

Quantum Cutting ($CaSO_4$:Tb,Na)

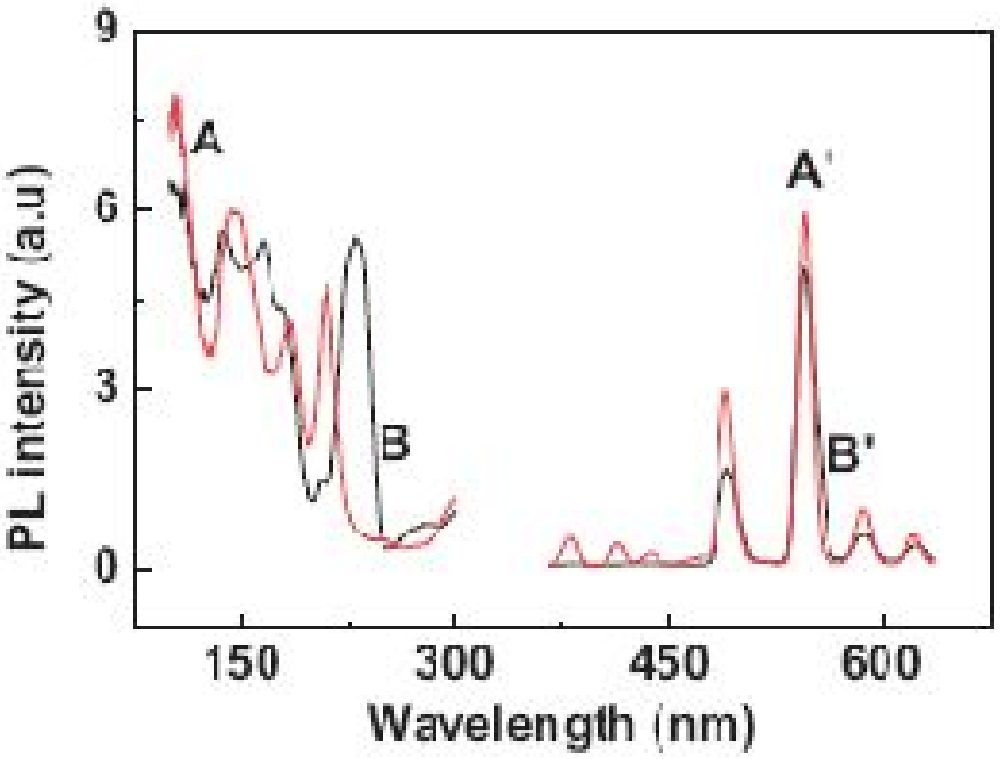

Figure 4. VUV excitation/emission (λ_{emi} = 545 nm, λ_{exi} = 147 nm) spectra of $CaSO_4$:Tb^{3+},Na^+ (made with NaCl) and YBO_3:Tb^{3-} phosphors. A and A′ denote excitation and emission spectra (red lines) of $CaSO_4$:Tb(4 %),Na(12 %), whereas B and B′ represent those (black lines) for the commercial green PDP phosphor, YBO_3:Tb^{3+}.

Quantum Efficiency

➔ 104 ~ 117%

➔ Compared to YBO_3:Tb^{3+}

Hyun M. Jang's Group, Postech
Adv. Funct. Mater. (2007).

Quantum Cutting ($CaSO_4$:Tb,Na)

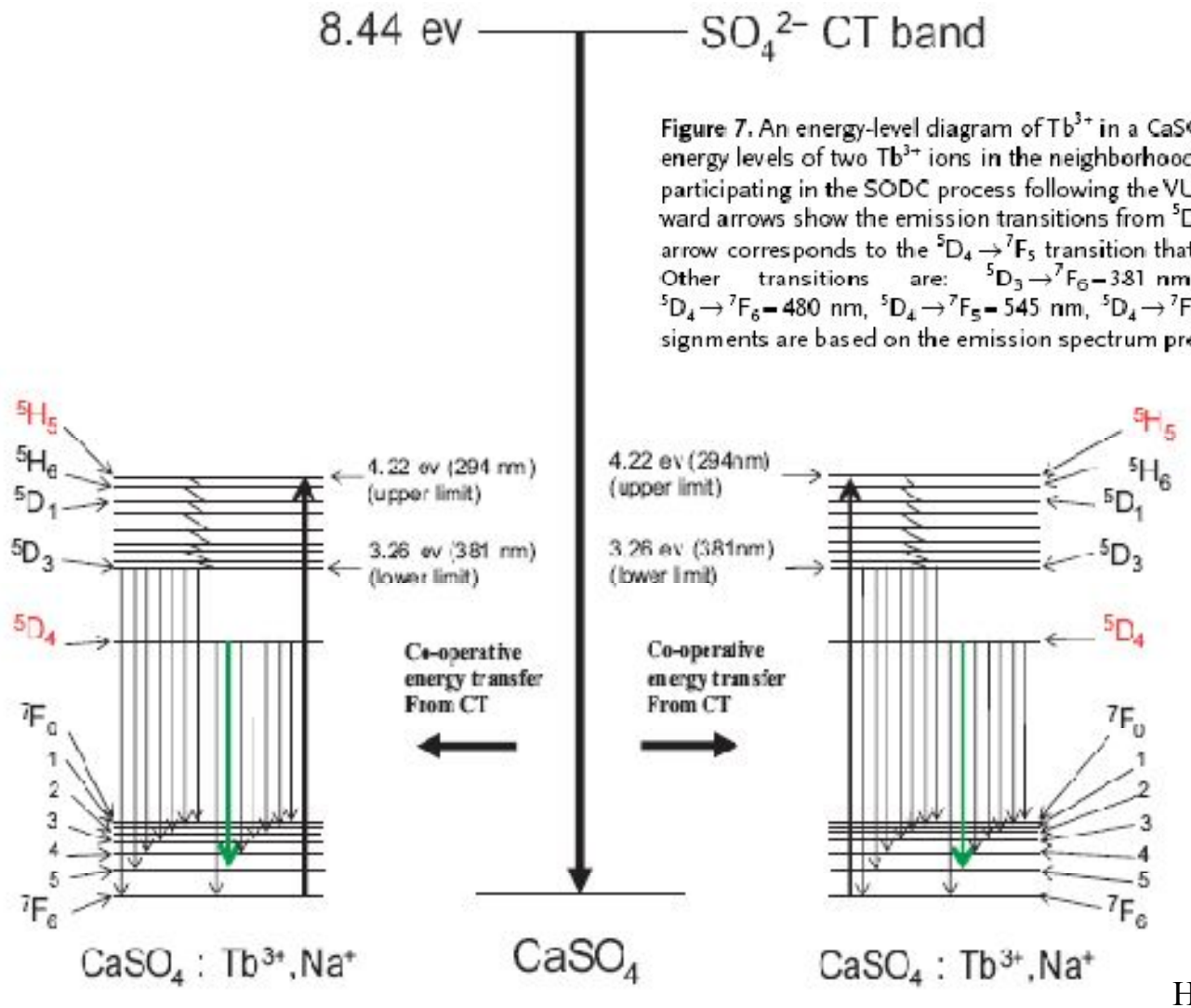

Figure 7. An energy-level diagram of Tb^{3+} in a $CaSO_4$:Tb,Na phosphor. The diagram shows various energy levels of two Tb^{3+} ions in the neighborhood of an SO_4^{2-} anion complex in $CaSO_4$:Tb^{3+},Na^+, participating in the SODC process following the VUV absorption at an SO_4^{2-} anion complex. Downward arrows show the emission transitions from $^5D_3$ and $^5D_4$ to various ^7F_j energy levels. The green arrow corresponds to the $^5D_4 \rightarrow {}^7F_5$ transition that results in the intense 545 nm green emission. Other transitions are: $^5D_3 \rightarrow {}^7F_6 = 381$ nm, $^5D_3 \rightarrow {}^7F_5 = 413$ nm, $^5D_3 \rightarrow {}^7F_4 = 435$ nm, $^5D_4 \rightarrow {}^7F_6 = 480$ nm, $^5D_4 \rightarrow {}^7F_5 = 545$ nm, $^5D_4 \rightarrow {}^7F_4 = 588$ nm, and $^5D_4 \rightarrow {}^7F_3 = 621$ nm. These assignments are based on the emission spectrum presented in Figure 4.

Hyun M. Jang's Group, Postech
Adv. Funct. Mater. (2007).

Quantum Splitting Phosphors

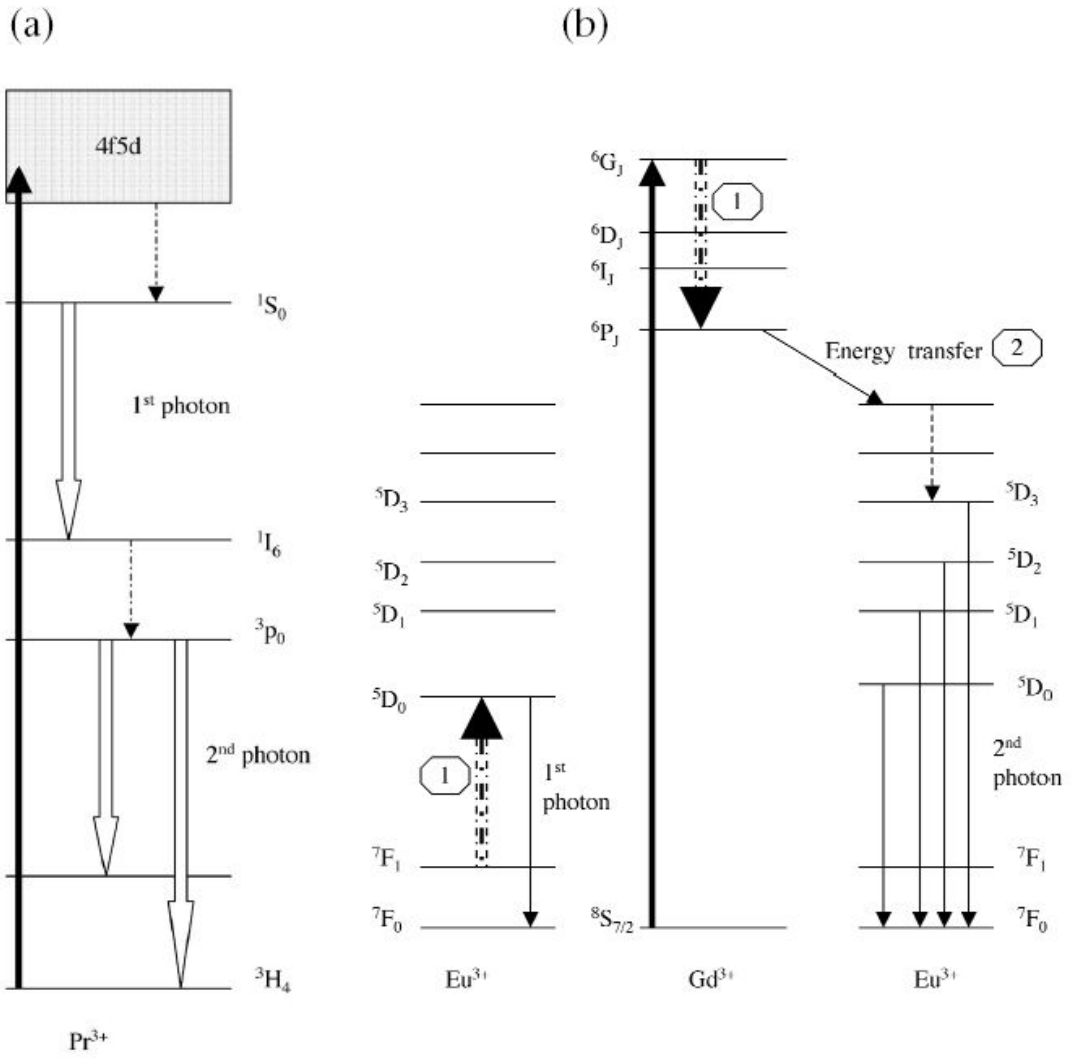

FIG. 3. Schematic representation of multiphoton emission via the Pr^{3+} ion and the Gd^{3+}-Eu^{3+} couple.

Recently, an effort in quantum-splitting phosphors centered on the trivalent gadolinium ion has been described in the literature.[7] Incident VUV photons are absorbed via the Gd^{3+} $^8S_{7/2} \rightarrow {}^6G_J$ optical transition (Fig. 3b). A cross-relaxation process excites the emission of the intentionally added activator, Eu^{3+} (Step P1 in Fig. 3b). During this cross-relaxation process the Gd^{3+} ion relaxes to the lower ^6P_J state. Energy migrating over the ^6P_J levels is trapped by a second Eu^{3+} ion (Step P2 in Fig. 3b). Hence, two red photons may be produced per incident VUV photon. Indeed, internal quantum efficiencies approaching nearly two in the $Li(Y,Gd)F_4:Eu^{3+}$ has been estimated.

C. R. Ronda, Caltech, *Interface* (2003)

Praseodymium

Energy-Transfer Pumping of Semiconductor Nanocrystals

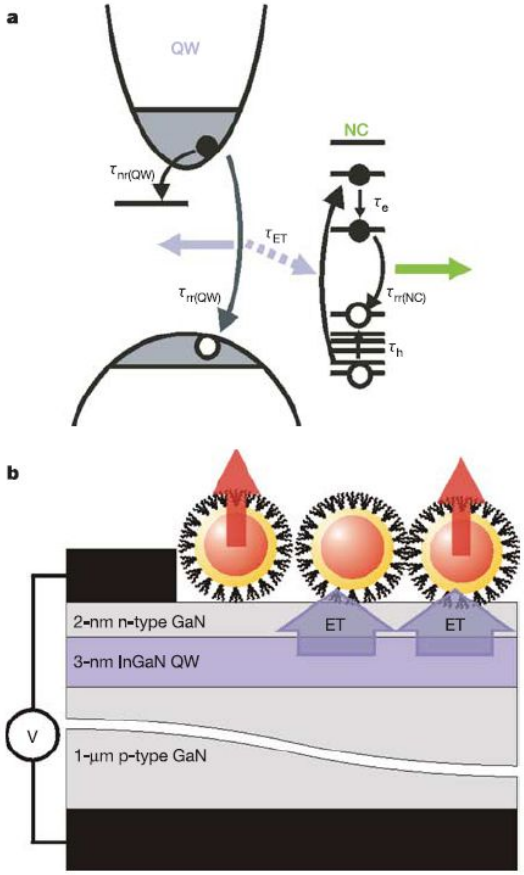

Figure 4 Carrier relaxation and energy-transfer processes in the hybrid quantum-well/nanocrystal structure and a schematic of an electrically driven energy-transfer device. **a**, The QW–NC energy transfer competes with radiative and non-radiative decay processes in the quantum well. High-energy excitations created in the nanocrystals through energy transfer rapidly relax (time constants τ_e and τ_h) to the nanocrystal band edge, which prevents backtransfer. Subscript e is electron and h is hole. **b**, An electrically powered hybrid quantum-well/nanocrystal device that can be used to realize the 'energy-transfer colour-converter' in the regime of electrical injection. It depicts an InGaN quantum well sandwiched between bottom p-type and thin, top n-type GaN barriers with attached metal contacts. The top contact only partially covers the quantum well and leaves open space for assembling the nanocrystals.

Figure 4a displays the schematics of energy transfer along with other relaxation processes in the hybrid quantum-well/nanocrystal structures studied in this work. Following photoexcitation, carrier thermalization, and cooling, the thermal distribution of free electrons and holes is established in the quantum well. Quantum-well carriers can decay either radiatively (time constant τ_{rr}) or non-radiatively (τ_{nr}), or experience energy transfer (τ_{ET}) into a nanocrystal. Carriers generated in the nanocrystal by resonant QW–NC energy transfer have significant access energies as measured with respect to the nanocrystal bandgap. Extremely fast intraband relaxation in nanocrystals (subpicosecond time scales)[12,13] rapidly removes carriers from resonance with the quantum-well transition and prevents backtransfer. In well-passivated nanocrystals, relaxed electron–hole pairs recombine primarily radiatively with a time constant of ~20 ns, emitting a photon with an energy that is determined by the nanocrystal size.

V. I. Klimov, Los Alamos National Laboratory
Nature (2004)

Nanocrystal Applications to LEDs

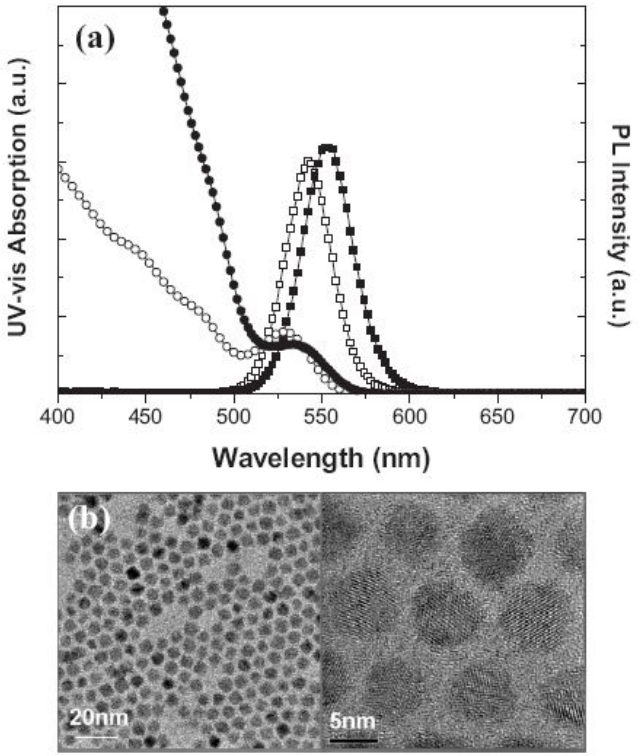

Figure 4. a) UV-vis absorption (circles) and PL emission (squares) spectra of CdSeS (open symbols) and CdSeS/ZnS (solid symbols) solutions. b) TEM (left) and HR-TEM (right) images of CdSeS/ZnS NCs.

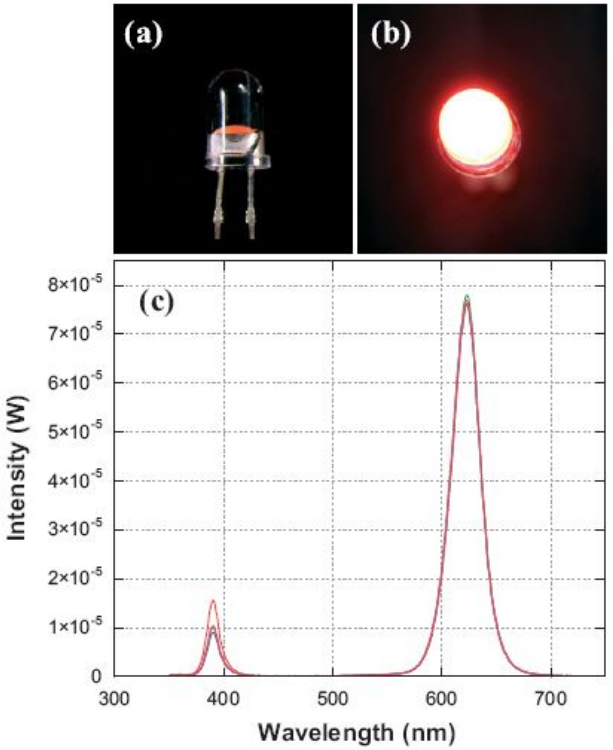

Figure 6. Photographs of a) an as-prepared NC-LED and b) a light-emitting NC-LED operating at 20 mA. c) Luminescent spectra of four samples of NC-LEDs operated at 20 mA.

In this Communication, we introduce a facile one-pot method for synthesizing a CdSe/CdS/ZnS core/multishell structure. The continuous crystal growth without core separation was easily scaled up to produce 3 g of NC powder in one pot. Also, the photostability of the NCs and their applicability to LEDs are described in detail.

E. Jang, SAIT, *Adv. Mater.* (2007)

Indium Composition Variations

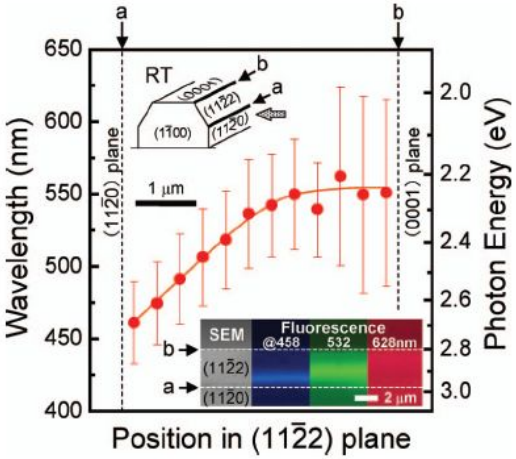

FIG. 2. (Color) Position dependence of the CL peak wavelength of the (11$\bar{2}$2) SQW. The error bars represent the emission line widths. The lower inset is a SEM image and monochromatic FLM images monitored at 458, 532, and 628 nm, while the upper inset shows a schematic sample structure where the arrow indicates the measurement direction.

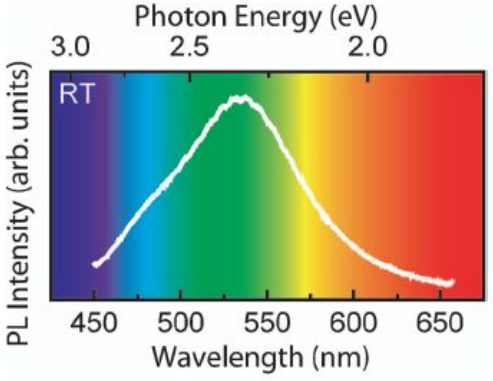

FIG. 3. (Color) PL spectrum of the {11$\bar{2}$2} SQWs measured at RT. The background color is equivalent to the emission colors.

The composition monotonously increased from 25% on the (11$\bar{2}$0) side to 40% on the (0001) side. Considering a 2-nm uniform well width and an internal electric field due to the piezoelectric and spontaneous polarization, the estimated QW transition energy ranged from 2.43 eV (510 nm) to 2.79 eV (444 nm).

This surprisingly large distribution of the In composition was caused by the growth characteristics of $In_xGa_{1-x}N$ on GaN microfacets. The STEM observation revealed that the growth rate became faster in the order (0001)>{11$\bar{2}$2}>{11$\bar{2}$0}, suggesting that the atoms migrated from {11$\bar{2}$0} toward (0001) through the {11$\bar{2}$2} facet. Furthermore, since an In atom possesses a higher diffusivity than Ga atom due to a higher vapor pressure, the In composition gradually increased along the stream of In migration; that is, (0001)>{11$\bar{2}$2}>{11$\bar{2}$0}.

K. Nishizuka, Kyoto University
Appl. Phys. Lett. (2007)

PL Enhancement and Surface Plasmon Dispersion

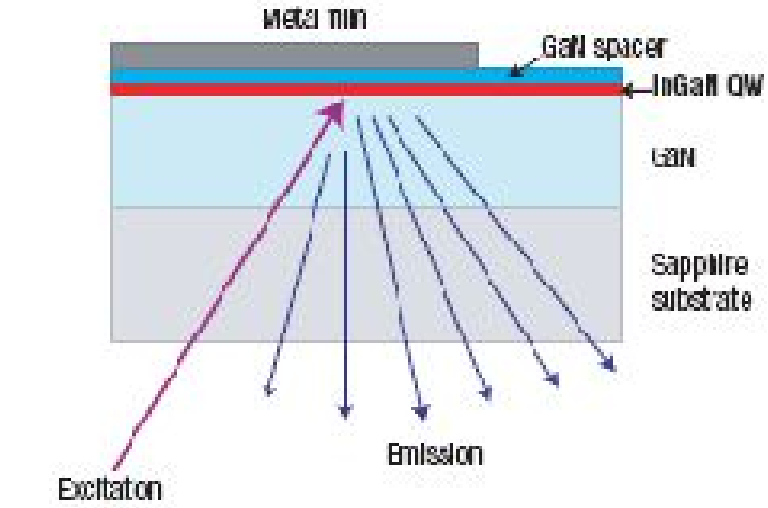

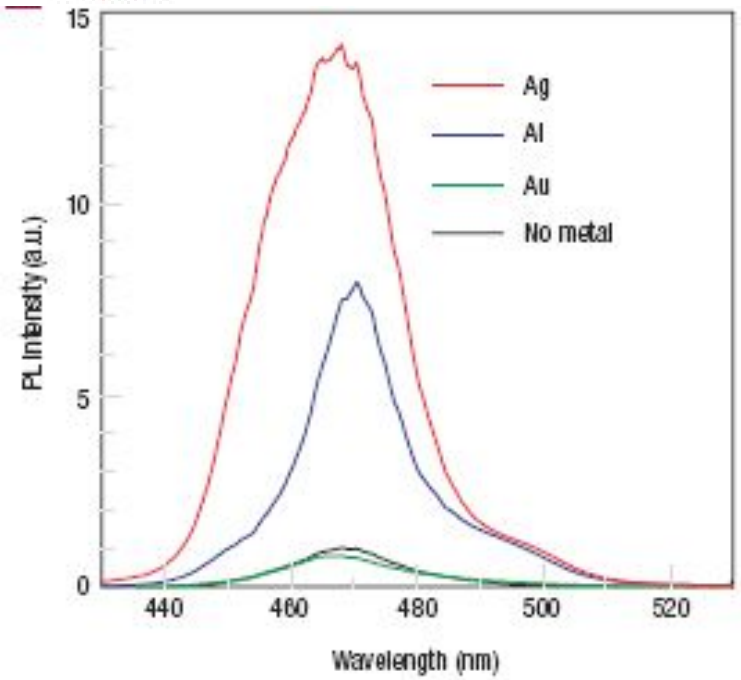

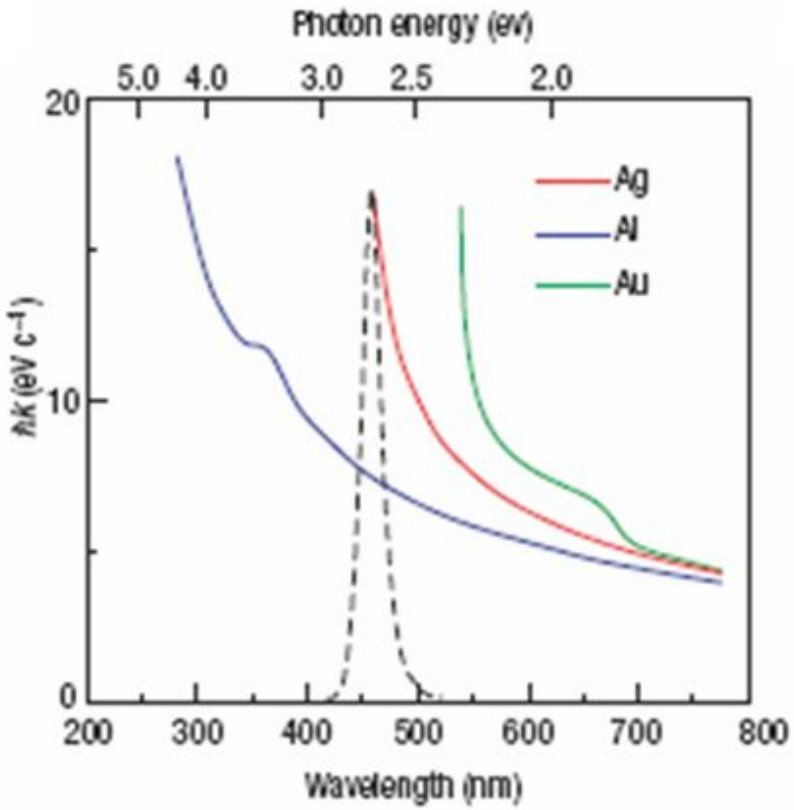

- Electron-hole pairs excited within the QW couple to electron vibrations at the metal/semiconductor interface when the energies of electron–hole pairs and of the metal SP are similar

A. Scherer, Caltech, *Nat. Mater.* (2004)

PL Enhancement and Surface Plasmon Dispersion

We propose a possible mechanism of QW-SP coupling and light extraction shown in Fig. 3. First, excitons are generated in the QW by photo-pumping or electrical pumping. For uncoated samples, these excitons are terminated by the radiative (k_{rad}) or nonradiative (k_{non}) recombination rates, and η_{int} is determined by the ratio of these two rates as $\eta_{int} = k_{rad}/(k_{rad}+k_{non})$. When a metal layer is grown within the near-field of the active layer, and when the bandgap energy ($\hbar\omega_{BG}$) of InGaN active layer is close to the electron vibration energy ($\hbar\omega_{SP}$) of SP at the metal-semiconductor surface, then the QW energy can transfer to the SP. PL decay rates are enhanced through the QW-SP coupling rate (k_{SP}), as k_{SP} values are expected to be very fast. High electromagnetic fields are introduced by the large density of states from the SP dispersion diagram, and this increases k_{SP}. QW-SP coupling in LED devices may be considered detrimental to the optical efficiency, because the SP is a nonpropagating evanescent wave. If the metal surface is perfectly flat, the SP energy would be thermally dissipated. However, the SP energy can be extracted as light by providing roughness or nanostructuring the metal layer. Such roughness allows SPs of high momentum to scatter, lose momentum, and couple to radiated light.[25] The few tens of nanometer sized roughness in the Ag surface layer can be obtained by controlling the evaporation conditions or by microfabrication to obtain the high photon extraction efficiencies.

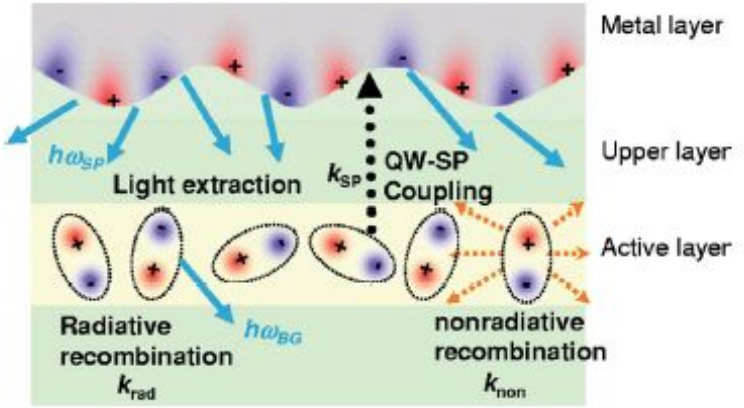

FIG. 3. (Color) Schematic diagram of the electron-hole recombination and QW-surface plasmon (SP) coupling mechanism.

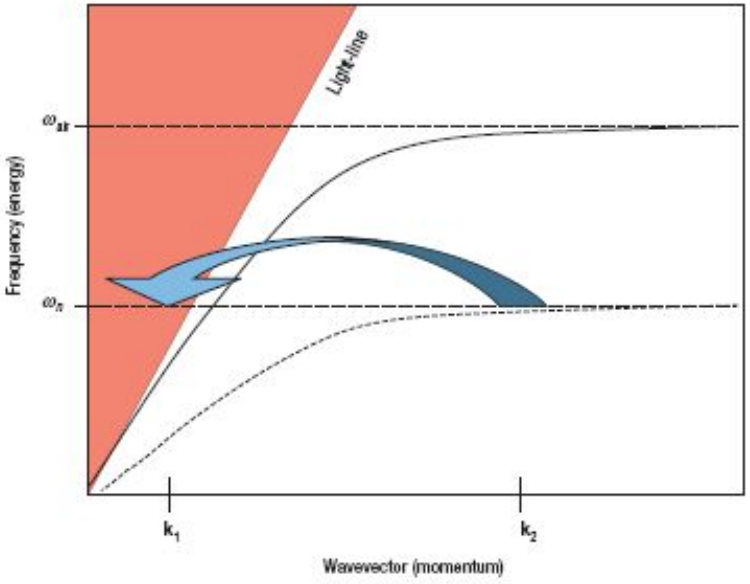

A. Scherer, Caltech, *Appl. Phys. Lett.* (2005)

Nanophosphors

Introduction

Phosphor

Luminescent material (phosphor):

A solid which converts certain types of energy into electromagnetic radiation.

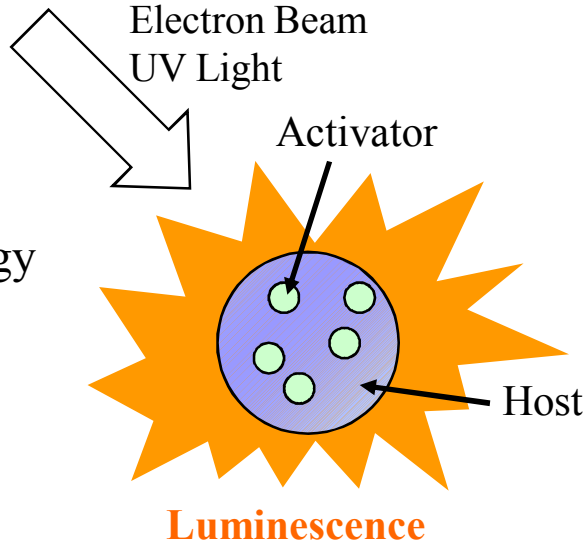

Applications

Introduction

❑ Nanophosphor

- Higher packing density
- Lower scattering of light
- Quantum size effect

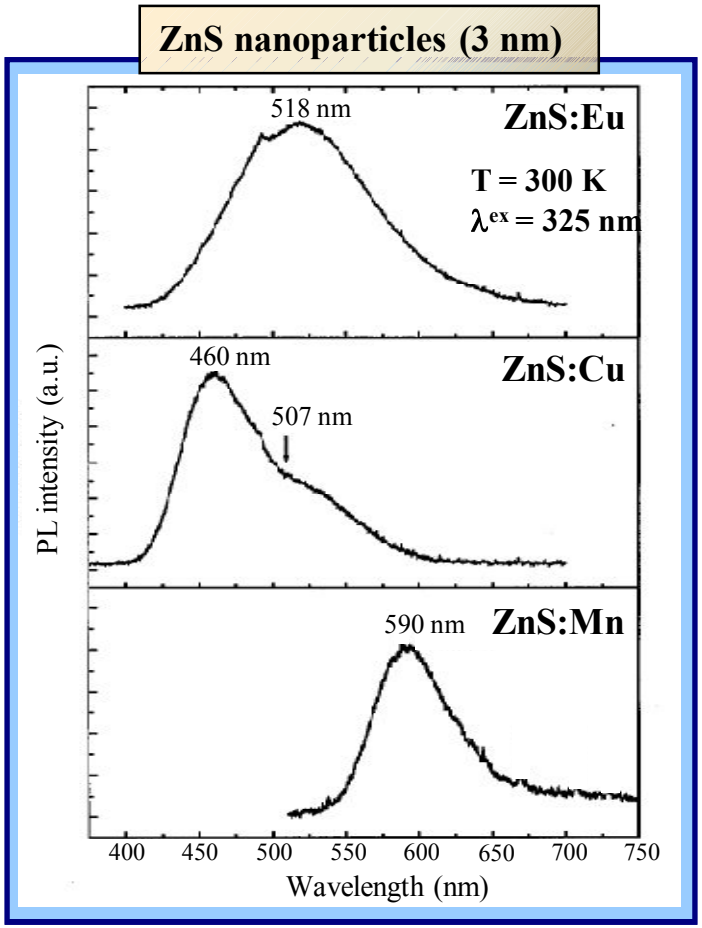

❑ Problems

- Low quantum efficiency, probably due to the surface adsorbates and defects in nanocrystals.
- PL properties will largely depend on the thermal histories of nanoparticles.
- However, characterizations of phosphor itself have been rare. (S. J. Chua's group, *APL*, 1998)

Need to systematically characterize the luminescence properties for developing high-efficiency nanophosphors

The Factors of PL Enhancement/Retardation

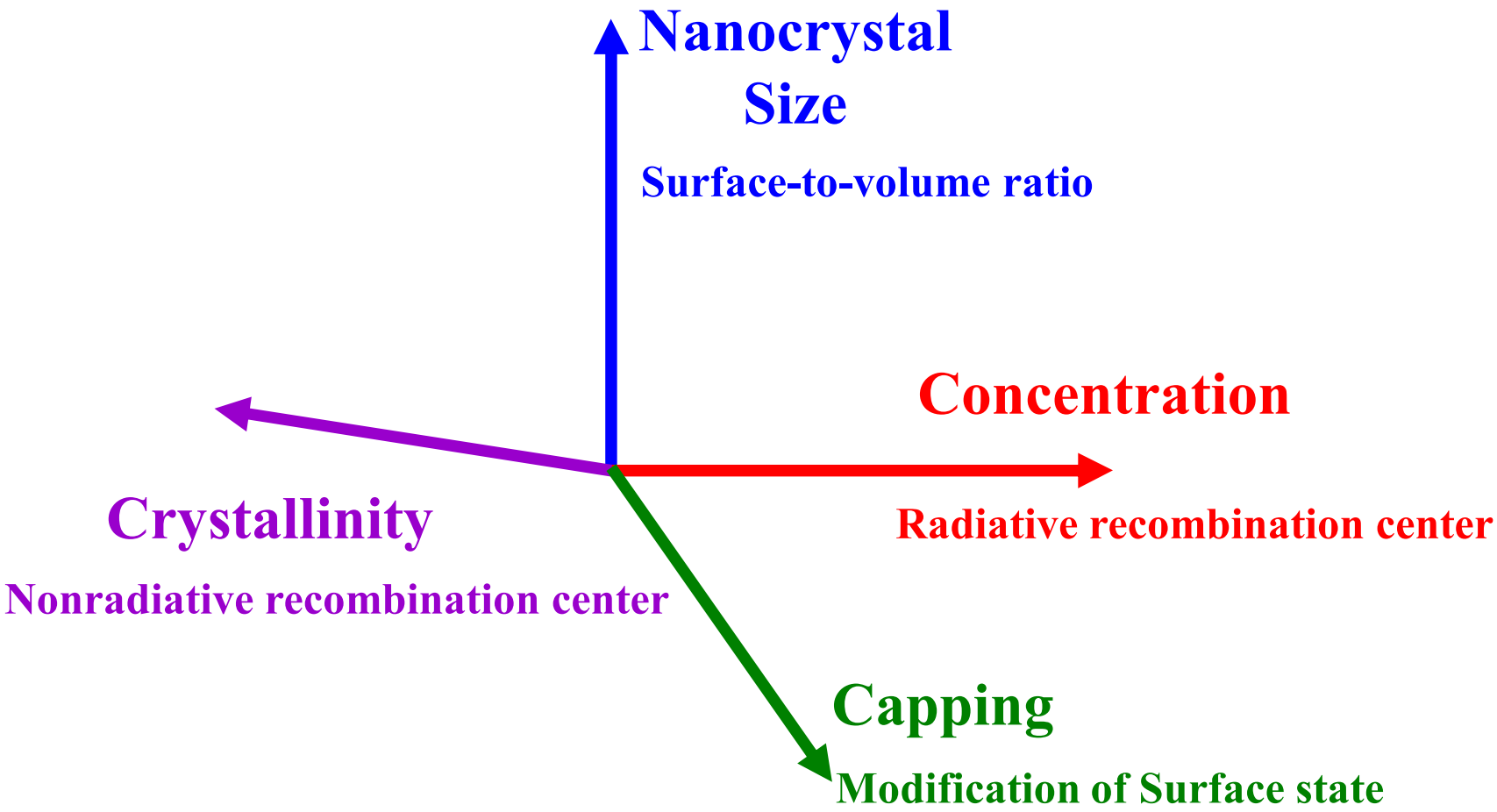

Non-Uniform Distribution of Local Strain

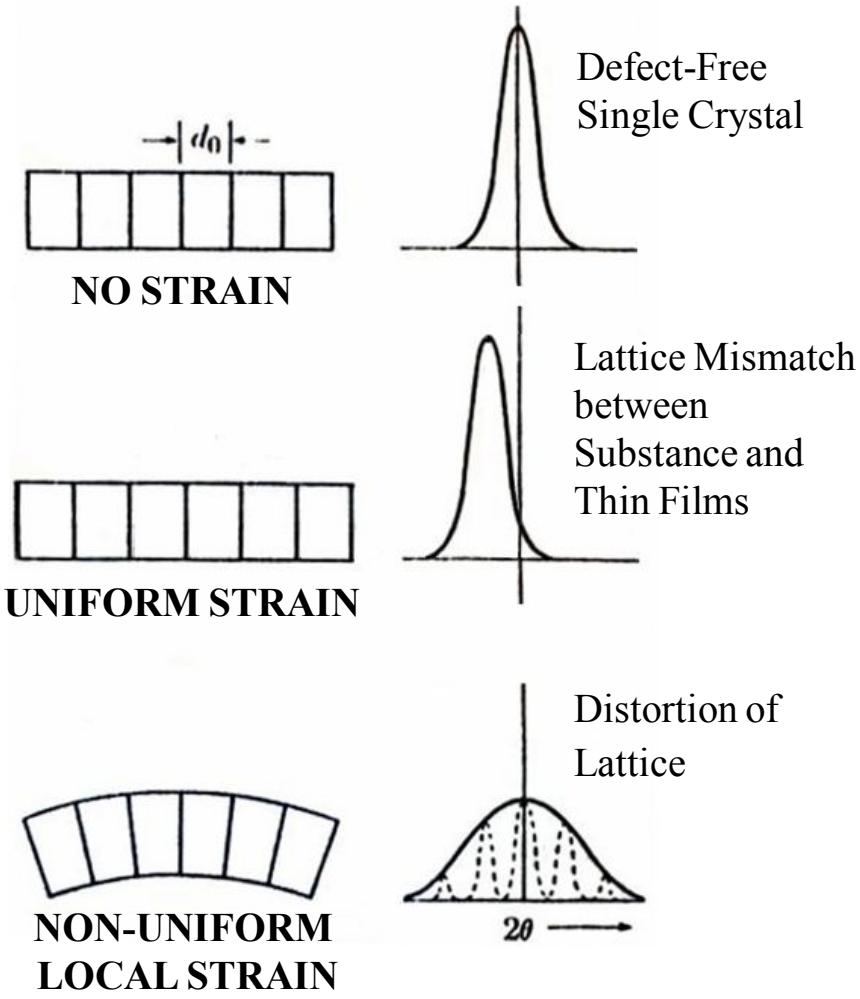

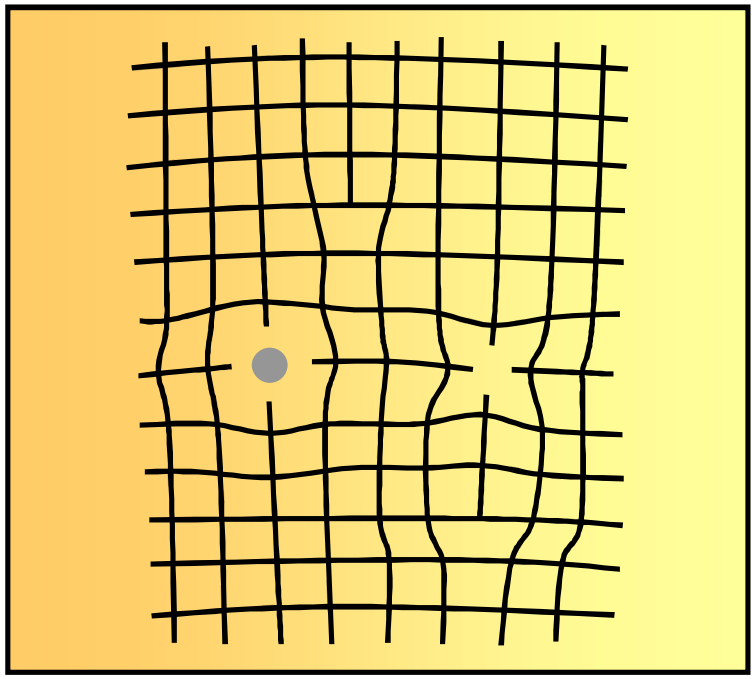

Non-Uniform Local Strain

Point Defects, Off-Stoichiometry, Stacking Faults, Dislocations, etc.

Synthesis and Photoluminescence of Mn-Doped Zinc Sulfide Nanoparticles

Dongyeon Son, Dae-Ryong Jung, Jongmin Kim, Taeho Moon, Chunjoong Kim, and Byungwoo Park*

APL **(2007)**

Motivation

- **Nanoparticles with monodispersity:**
  Technical challenge for luminescence applications
- **Temperature dependence of ZnS:Mn nanocrystals:**
  In aspect of water/organic quenching and local strain

How to improve the luminescence properties?
What is the optimum condition?

The Goals:

✓ **Synthesis of nearly monodisperse ZnS:Mn nanoparticles with a simple method**
✓ **Doping-concentration effects**
✓ **Annealing-temperature effects for both the water/organic quenching and the local strain**

Synthesis of ZnS:Mn Nanoparticles by LSS Method

(Liquid-Solid-Solution)

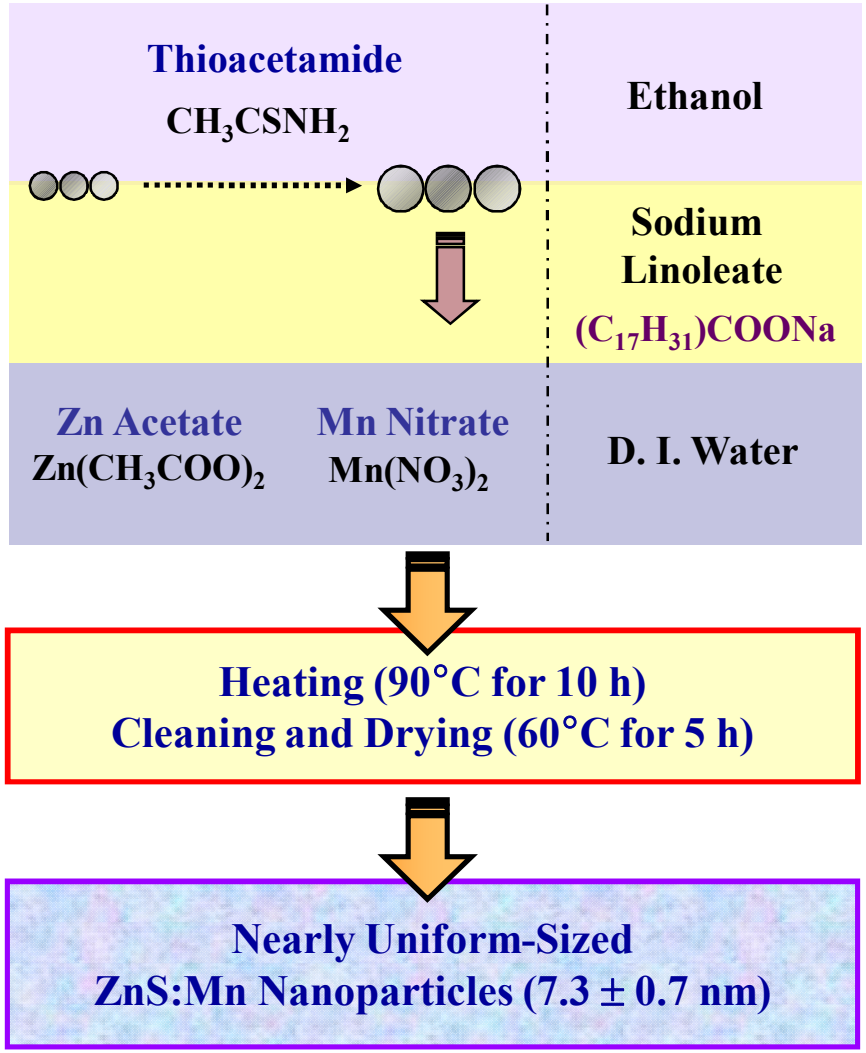

Yadong Li's group, *Nature* (2005).

ZnS Structure

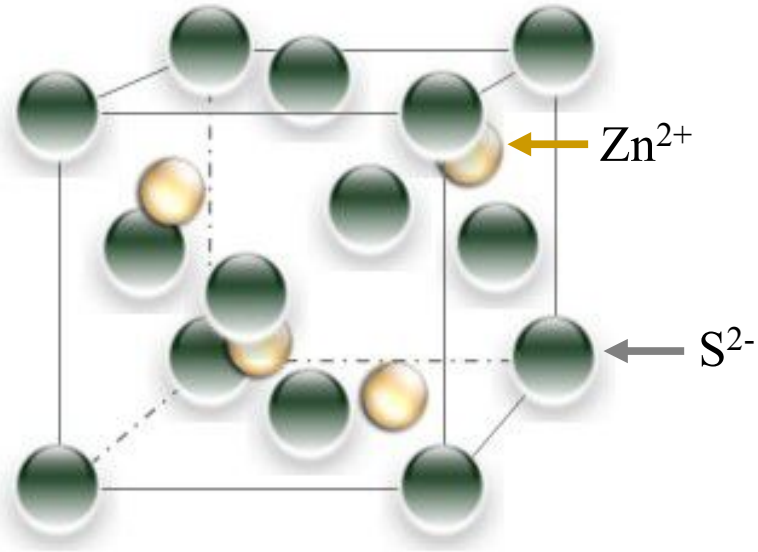

Cubic Zinc Blende ($\bar{F}43m$)

X-Ray Diffraction for Various Doping Concentrations

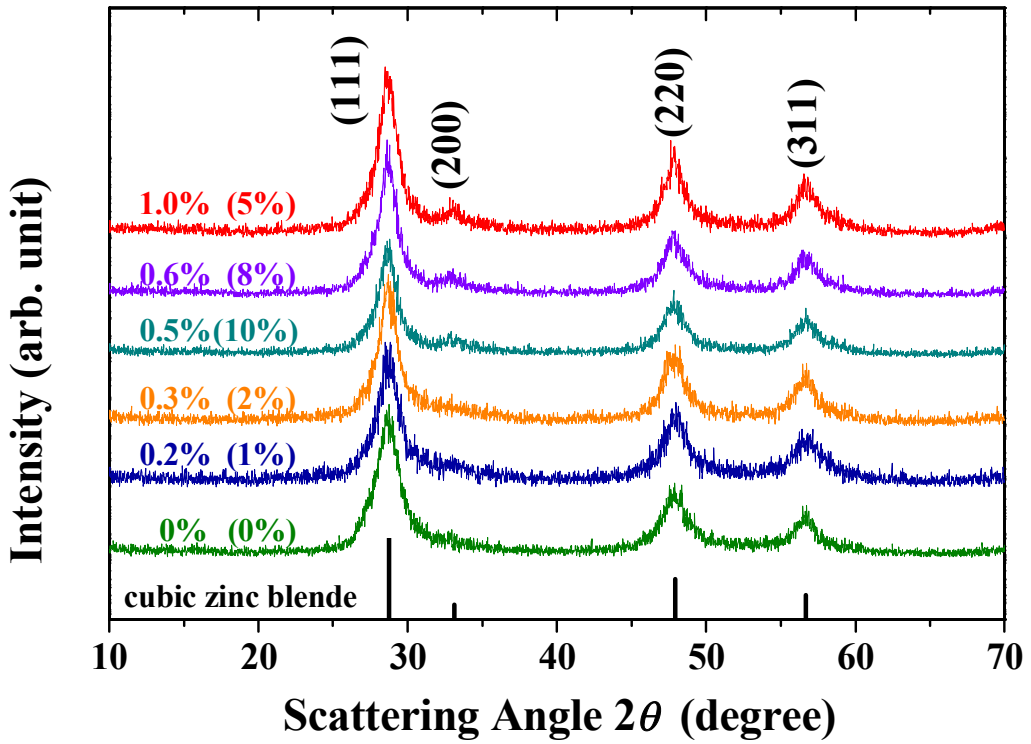

* The values in the parentheses are Mn precursor concentration during syntheses.

- XRD patterns with different Mn concentrations
- Cubic zinc-blende structure, no secondary phases

Nearly Monodisperse Nanoparticles

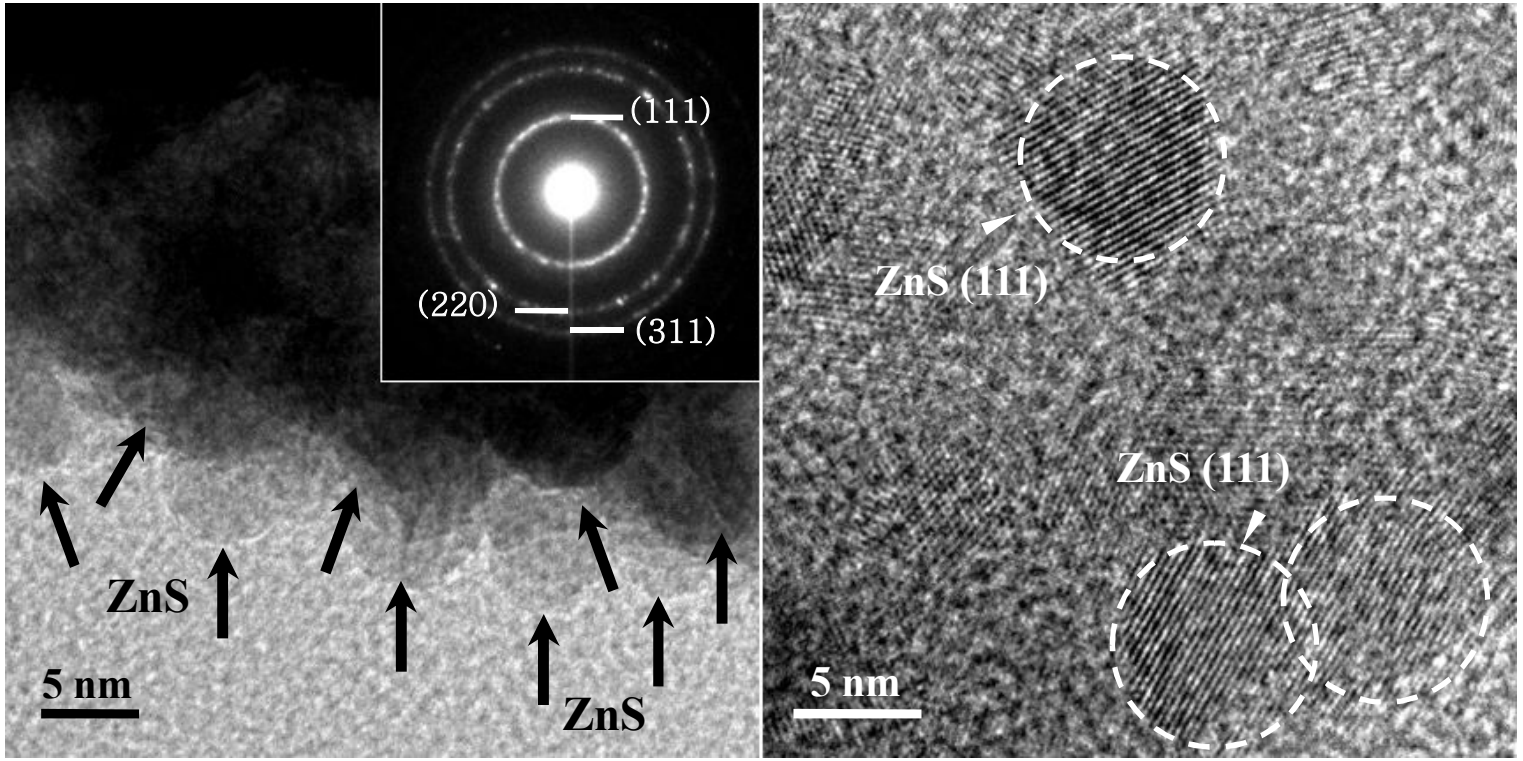

- TEM images show nearly monodisperse (7.3 ± 0.7 nm) ZnS:Mn nanoparticles.
- The inset represents diffraction patterns confirming crystalline ZnS.

Band Gap Estimation of Nanoparticles

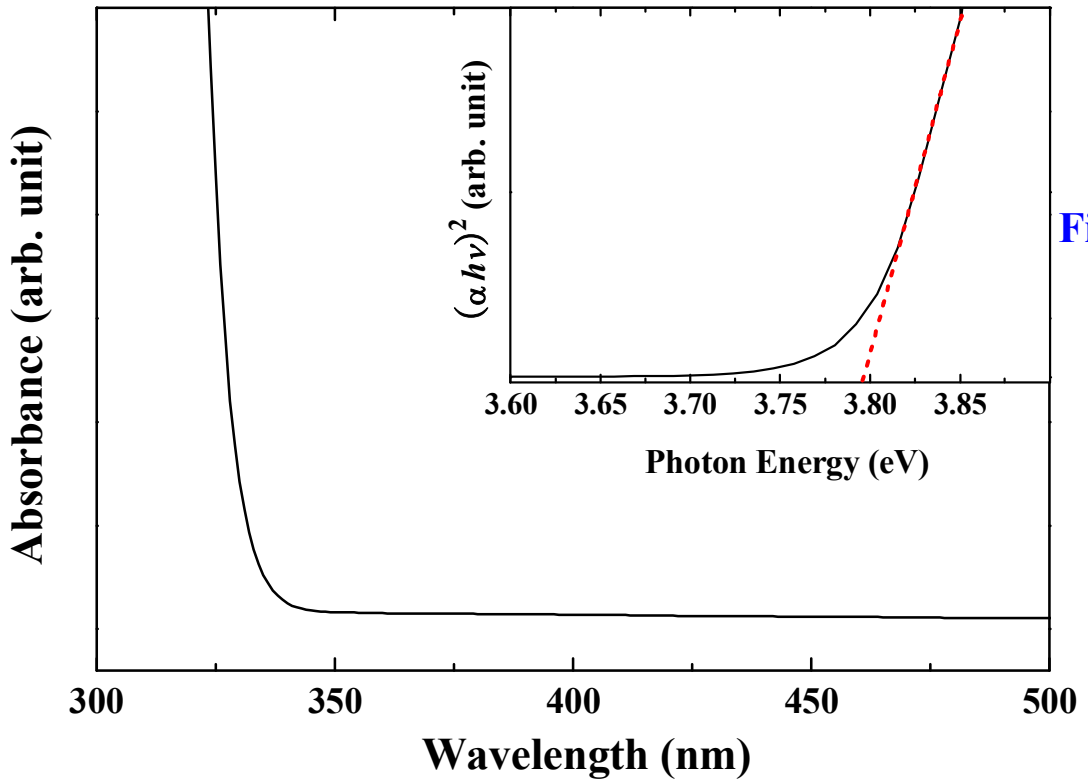

Fitted E_g: ~3.8 eV (~7 nm ZnS)

- **The fitted E_g (~3.8 eV) is larger than that of bulk ZnS (3.7 eV).**
- **The calculated E_g value by Brus equation: 3.79 eV.**

The Effect of Annealing Temperature on PL Properties

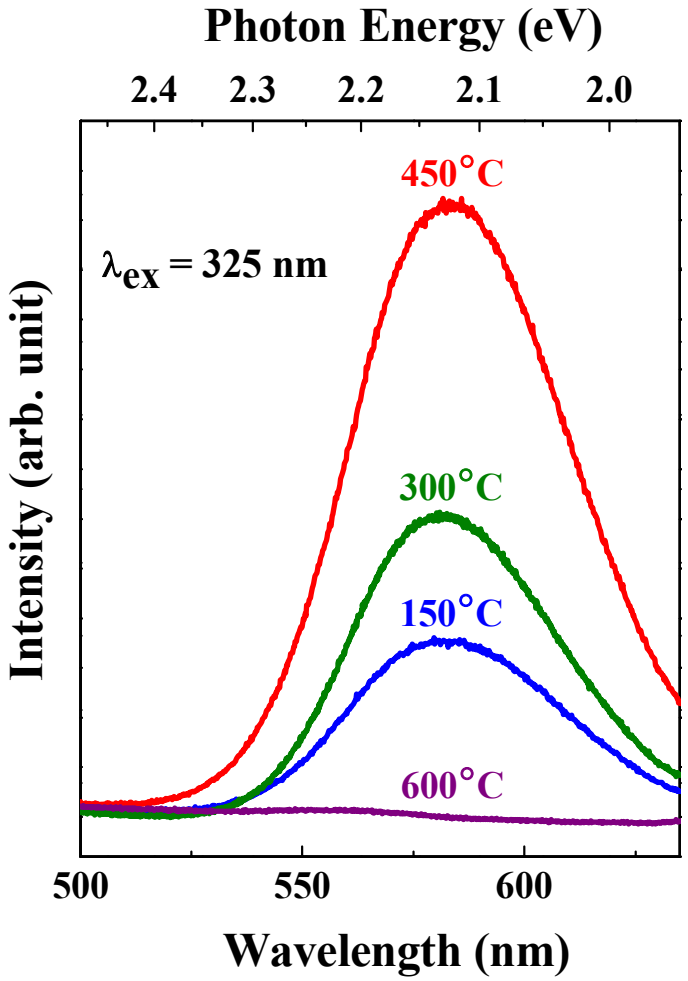

The slope of Δk vs. k representing the local strain ($\Delta d/d$)

Annealing Temp. (Actual Mn Concent. ≅ 1 at. %)	Local Strain	Nanoparticle Size
Room Temp.	1.18 ± 0.42%	5.7 ± 0.5 nm
150°C	0.91 ± 0.34%	6.3 ± 0.4 nm
300°C	0.76 ± 0.29%	6.9 ± 0.5 nm
450°C	0.53 ± 0.22%	7.2 ± 0.4 nm
600°C	Phase Transition	Phase Transition

❖ With the increasing annealing temperature, the local strain was reduced.

Reduction of Water/Organics

Linoleic Acid: $(C_{17}H_{31})COOH$
Sodium Linoleate: $(C_{17}H_{31})COONa$

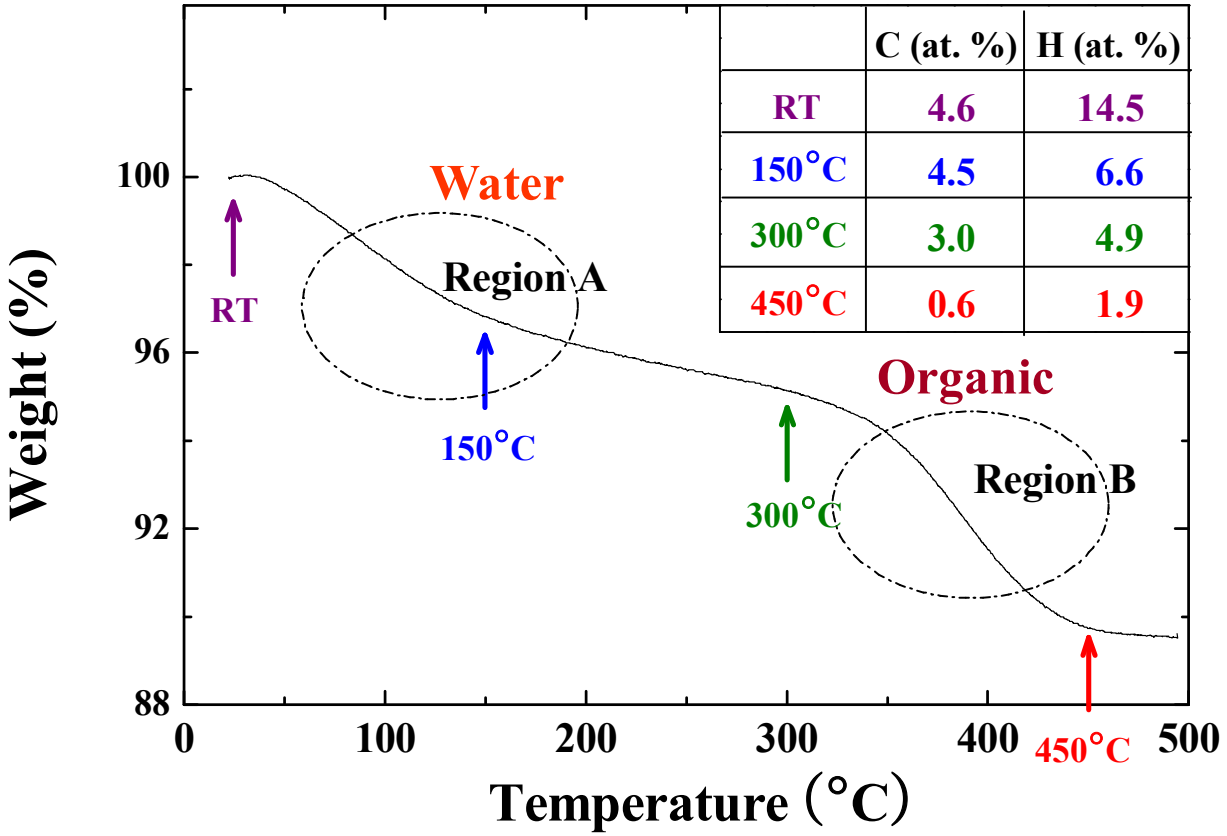

	C (at. %)	H (at. %)
RT	4.6	14.5
150°C	4.5	6.6
300°C	3.0	4.9
450°C	0.6	1.9

- TGA result for the ZnS:Mn nanoparticles:
  evaporation of water (Region A) + decomposition of organics (Region B).
- CHNS results show the presence of carbon and hydrogen quantitatively.

Peak Shift to the Pure ZnS Values

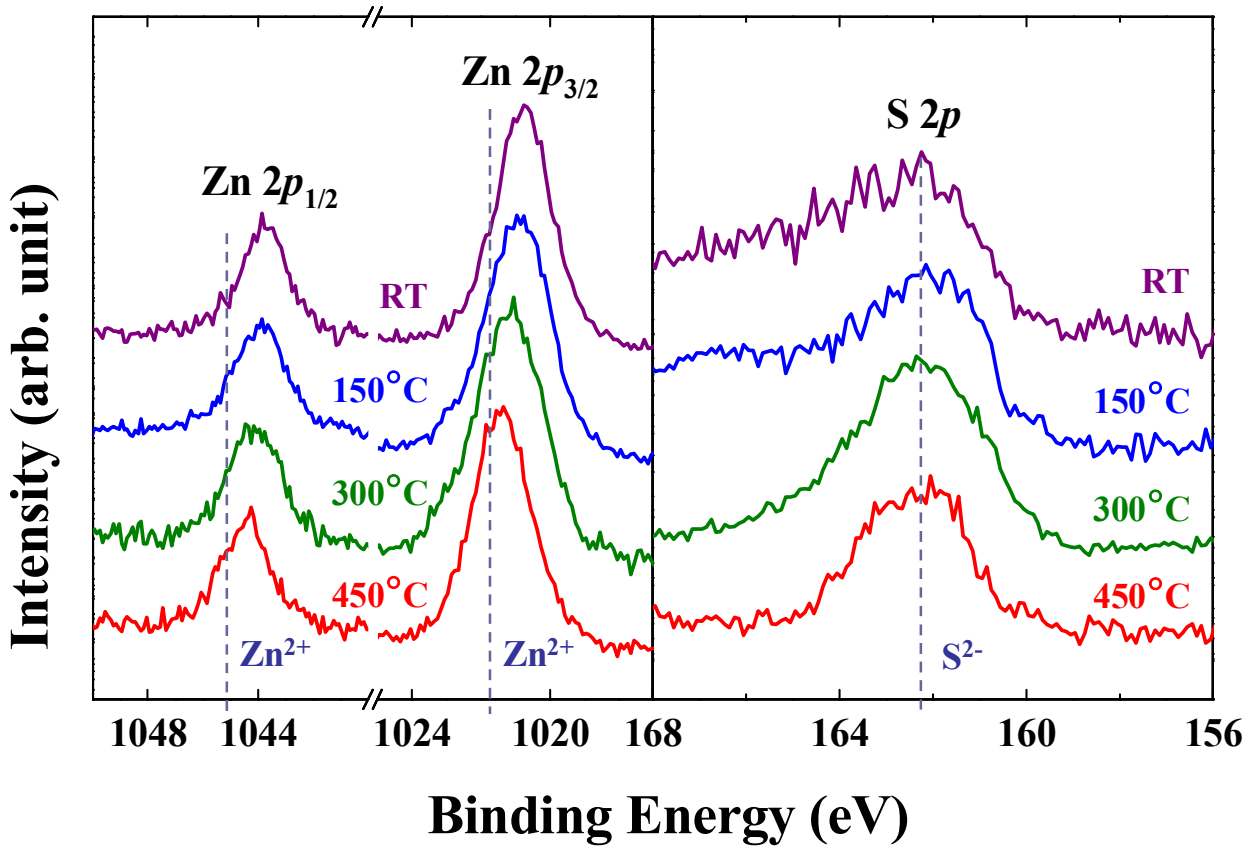

- **The peak shift of Zn 2*p* peaks:**
  After 450°C annealing, the peaks are close to the values for pure ZnS.
- **Broad shoulder peak (~165.5 eV) of S 2*p***

Schematic Figure for the Annealing-Temperature Effect

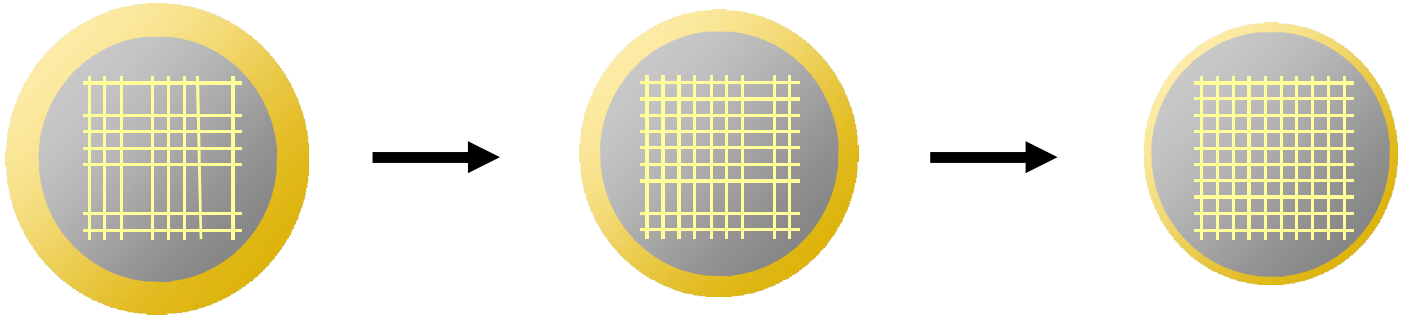

150°C 300°C 450°C

Removal of Water + Organic Capping

Enhanced Crystallinity

Improvement of PL Intensity

Linoleic Acid: $(C_{17}H_{31})COOH$

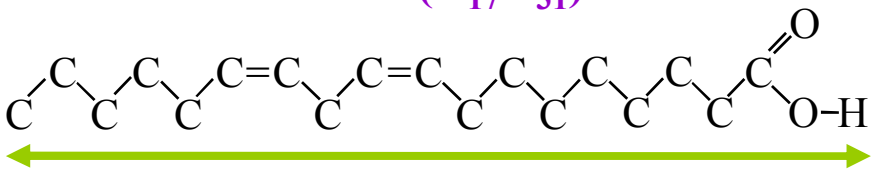

~2.2 nm

- **Density estimation from TGA at RT**
  - ➡ **0.82 organics per nm²**
  - ➡ **7.32 water molecules per nm²**

Highly-Luminescent Surface-Passivated ZnS:Mn Nanoparticles by a Simple One-Step Synthesis

Dae-Ryong Jung, Dongyeon Son, Jongmin Kim, Chunjoong Kim, and Byungwoo Park*

***APL* (2008)**

Synthesis of ZnS:Mn Nanoparticles by LSS Method

(Liquid-Solid-Solution)

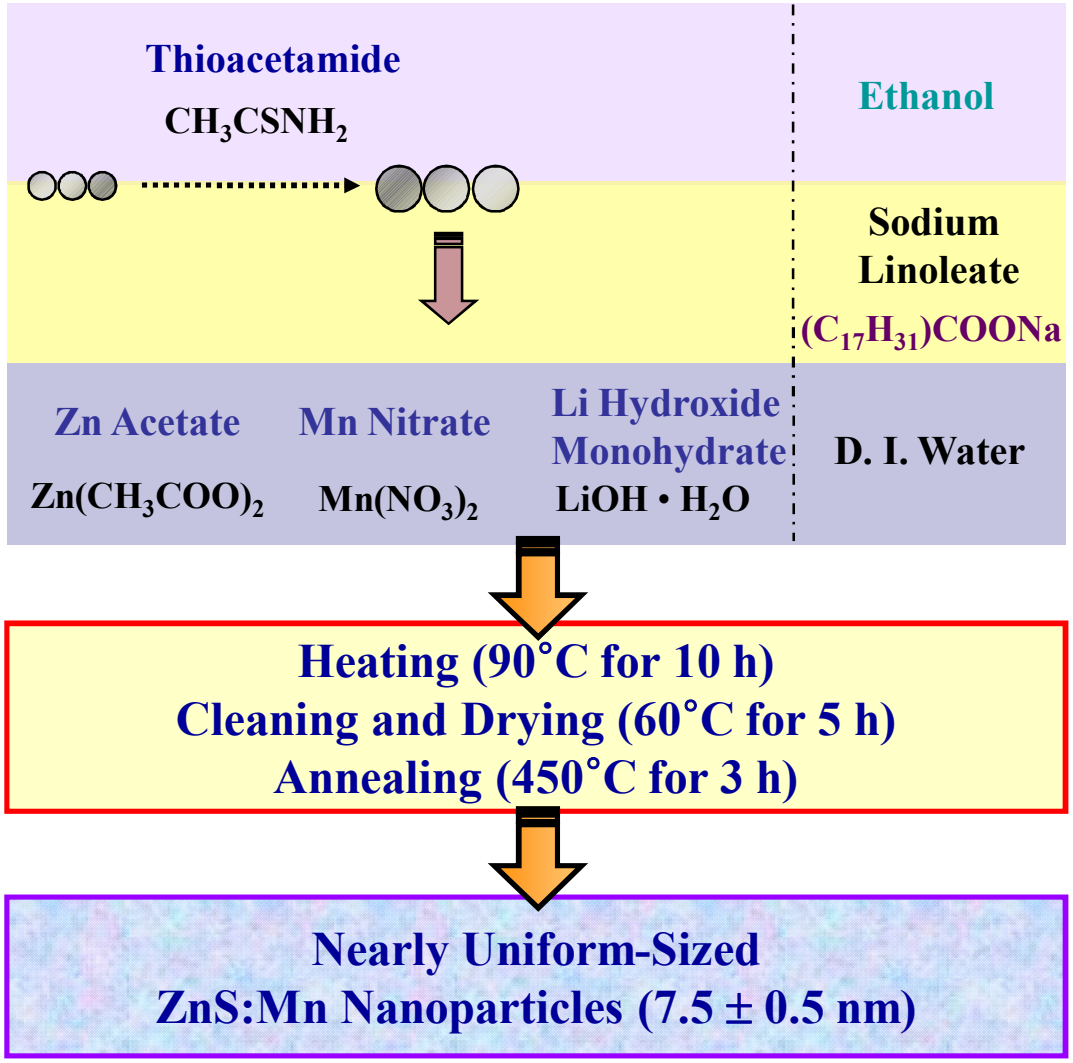

Yadong Li's group, *Nature* (2005).

My group, *Appl. Phys. Lett.* (2007).

Energy Diagram of Mn^{2+} Ion ($^4T_1$ - $^6A_1$ Transition)

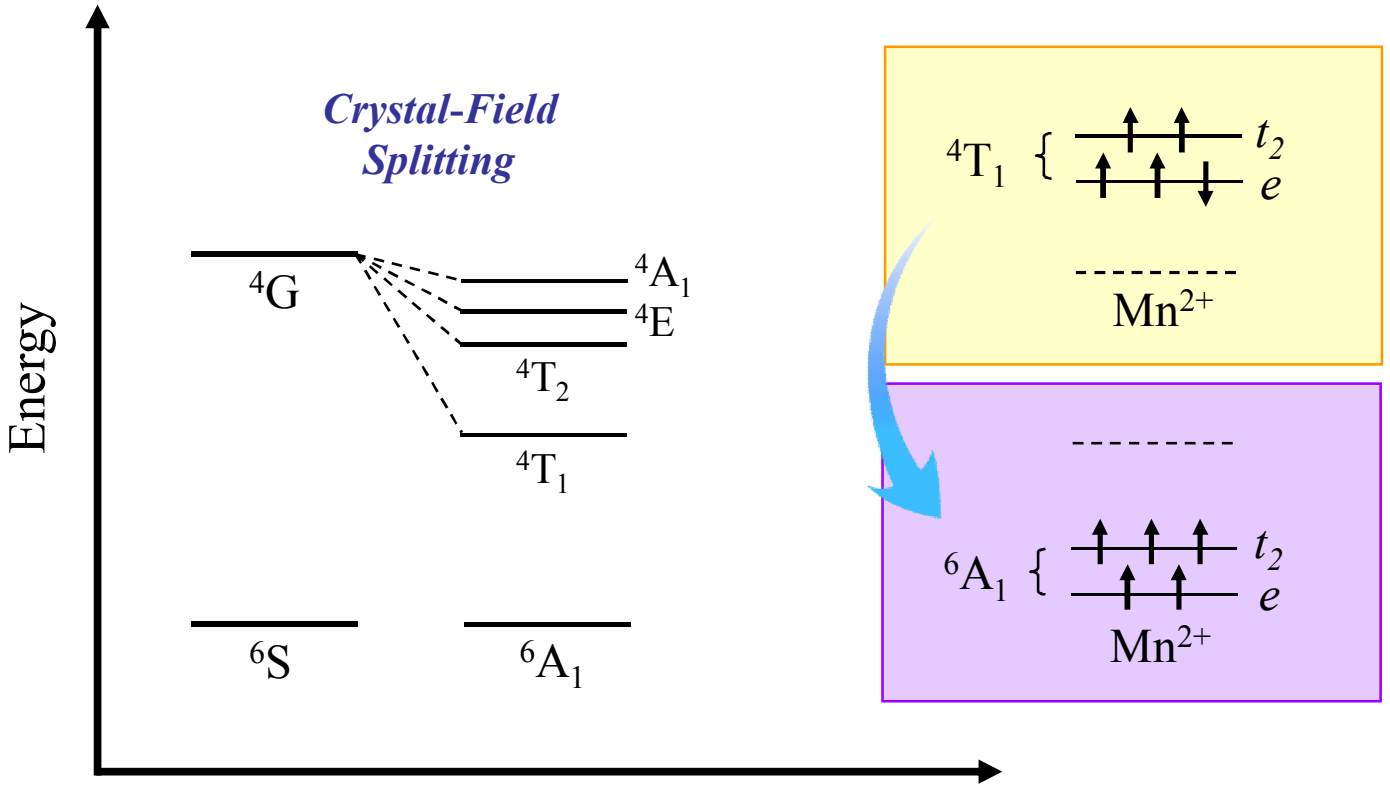

• **Characteristic emission of Mn^{2+} ions: $^4T_1$ (excited) – $^6A_1$ (ground)**

X-Ray Diffraction

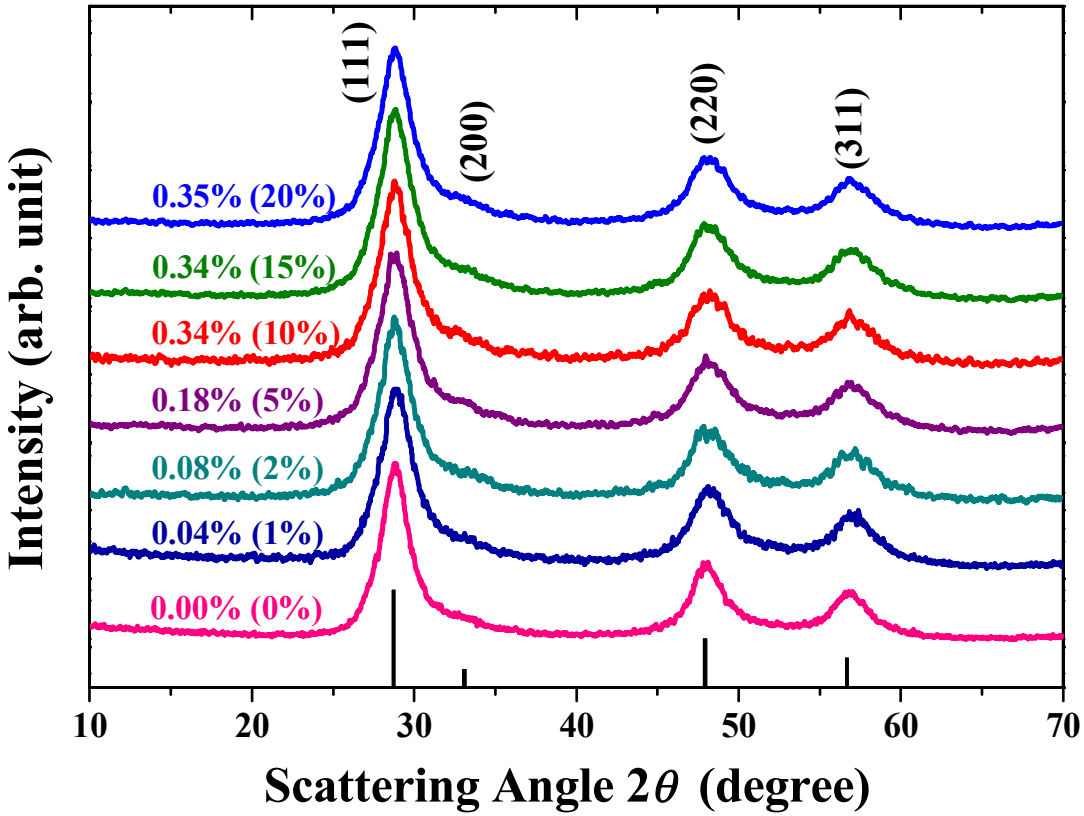

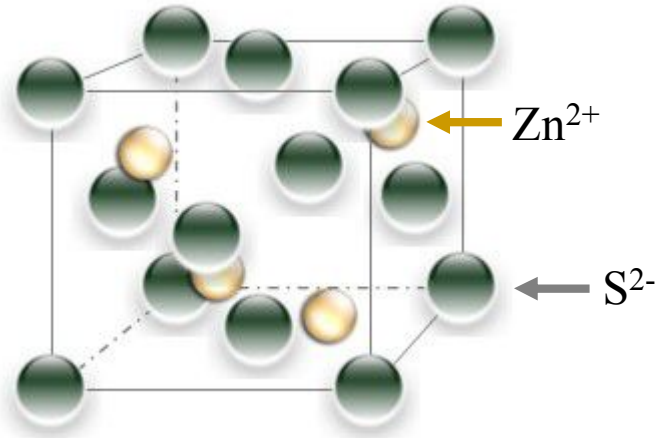

Cubic Zinc Blende ($F\bar{4}3m$)

- **XRD patterns with different Li concentrations (Mn concent. ≅ 1 at. %)**
- **Cubic zinc-blende structure, no secondary phases**

Local Strain and Nanoparticle Size

Li Concent. (Li-Precursor Concent.) 450°C Annealing Mn Concent. ≅ 1 at. %	Local Strain	Nanoparticle Size
0 at. % (0 at. %)	0.55 ± 0.12%	7.2 ± 0.4 nm
0.04 at. % (1 at. %)	0.66 ± 0.13%	7.4 ± 0.5 nm
0.08 at. % (2 at. %)	0.67 ± 0.19%	7.5 ± 0.5 nm
0.18 at. % (5 at. %)	0.62 ± 0.15%	7.5 ± 0.4 nm
0.34 at. % (10 at. %)	0.62 ± 0.18%	7.6 ± 0.5 nm
0.34 at. % (15 at. %)	0.68 ± 0.19%	7.8 ± 0.6 nm
0.35 at. % (20 at. %)	0.67 ± 0.19%	7.9 ± 0.6 nm

❖ **Scherrer formula**

$$\Delta k = \frac{2\pi}{D} + \frac{\Delta d}{d} k$$

Capping Effects on PL Properties

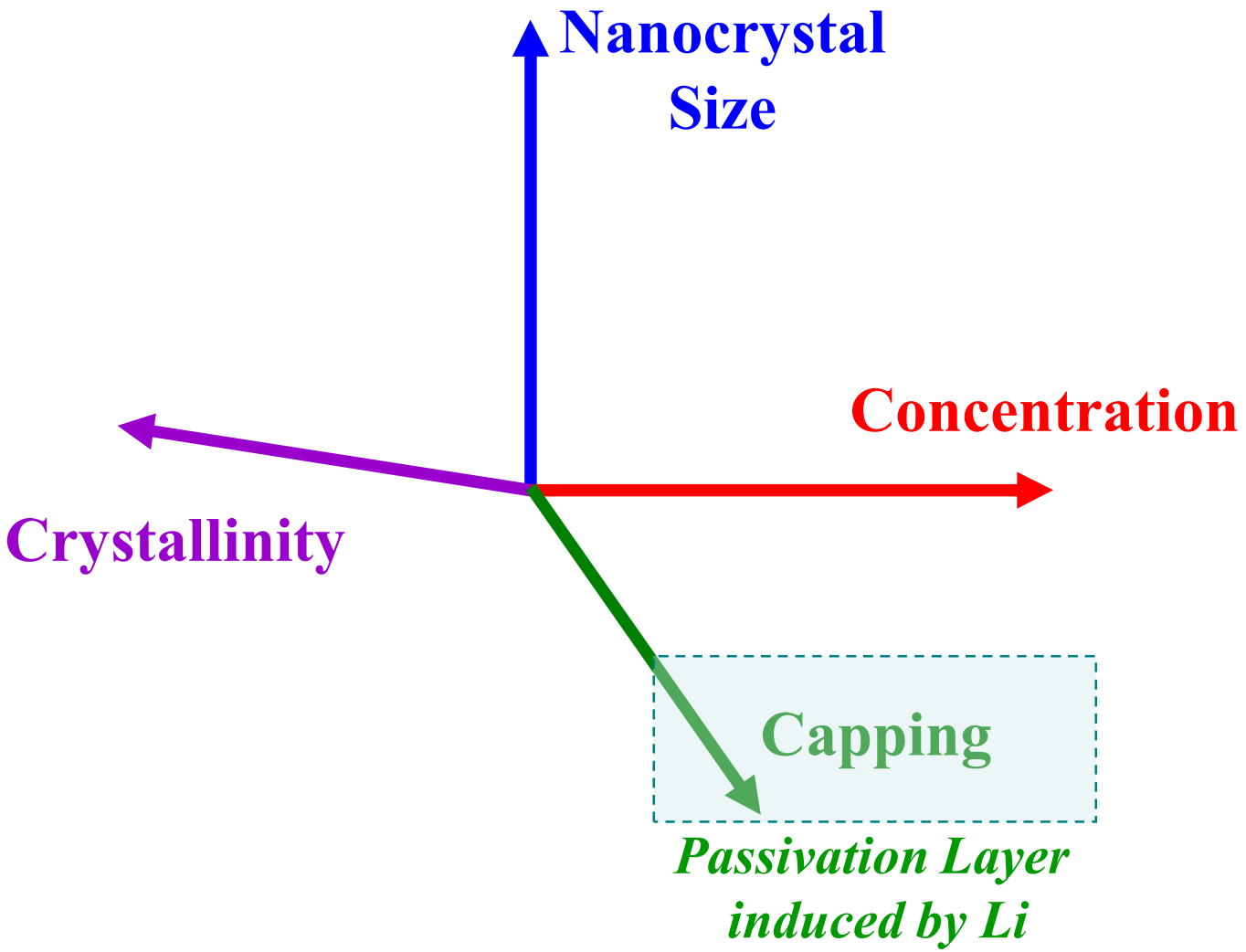

The Effect of Li Concentration for PL Properties

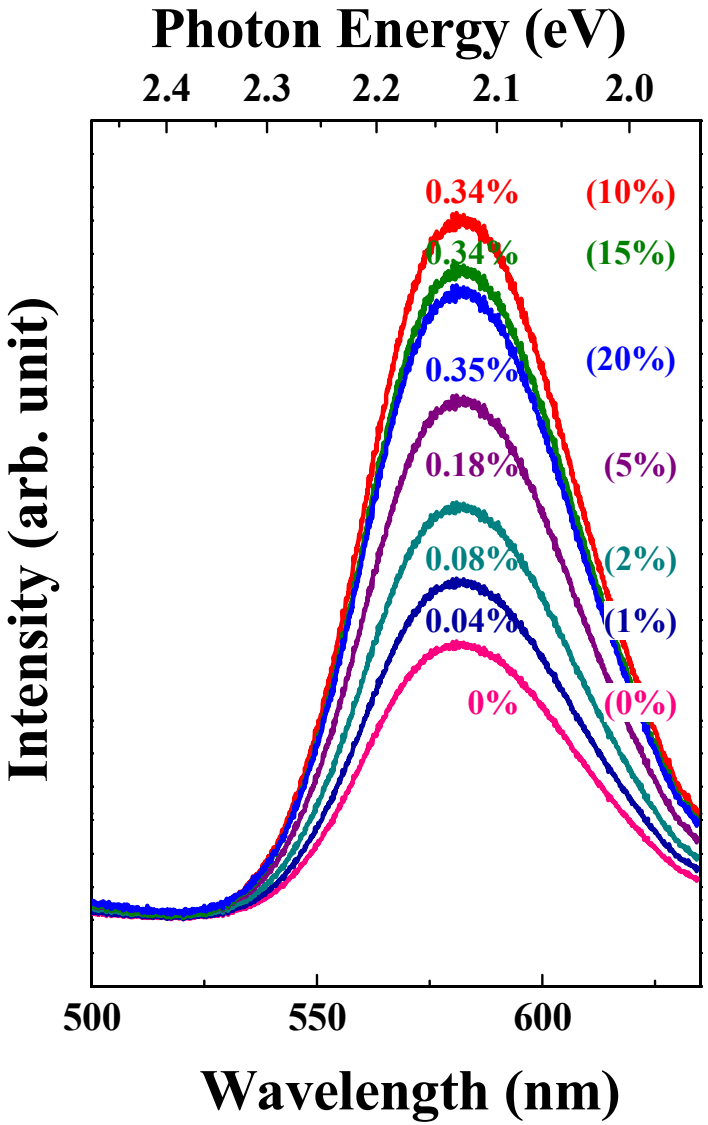

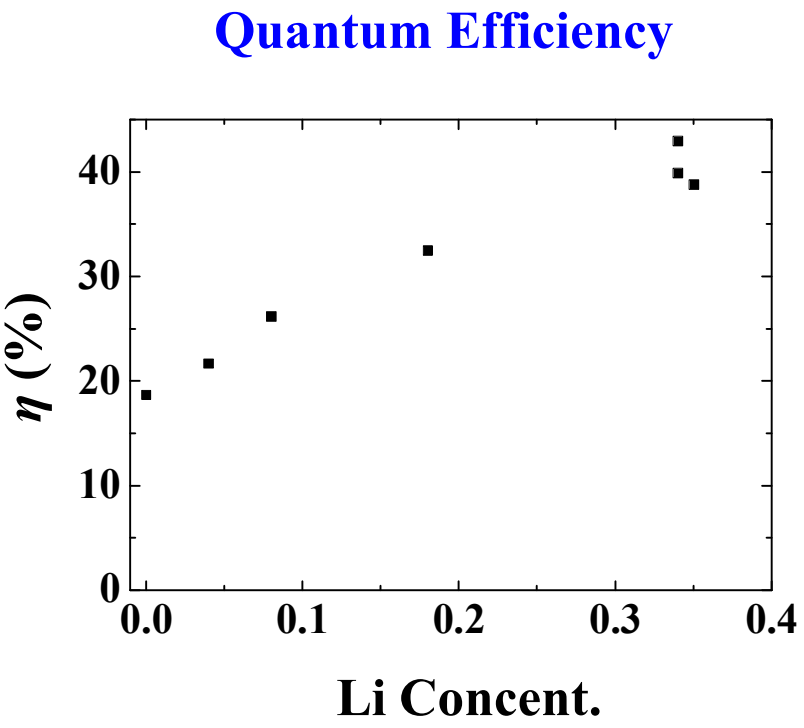

Issue:
How to Confirm the **Effect of Passivation Layer**?

X-Ray Photoemission Spectra

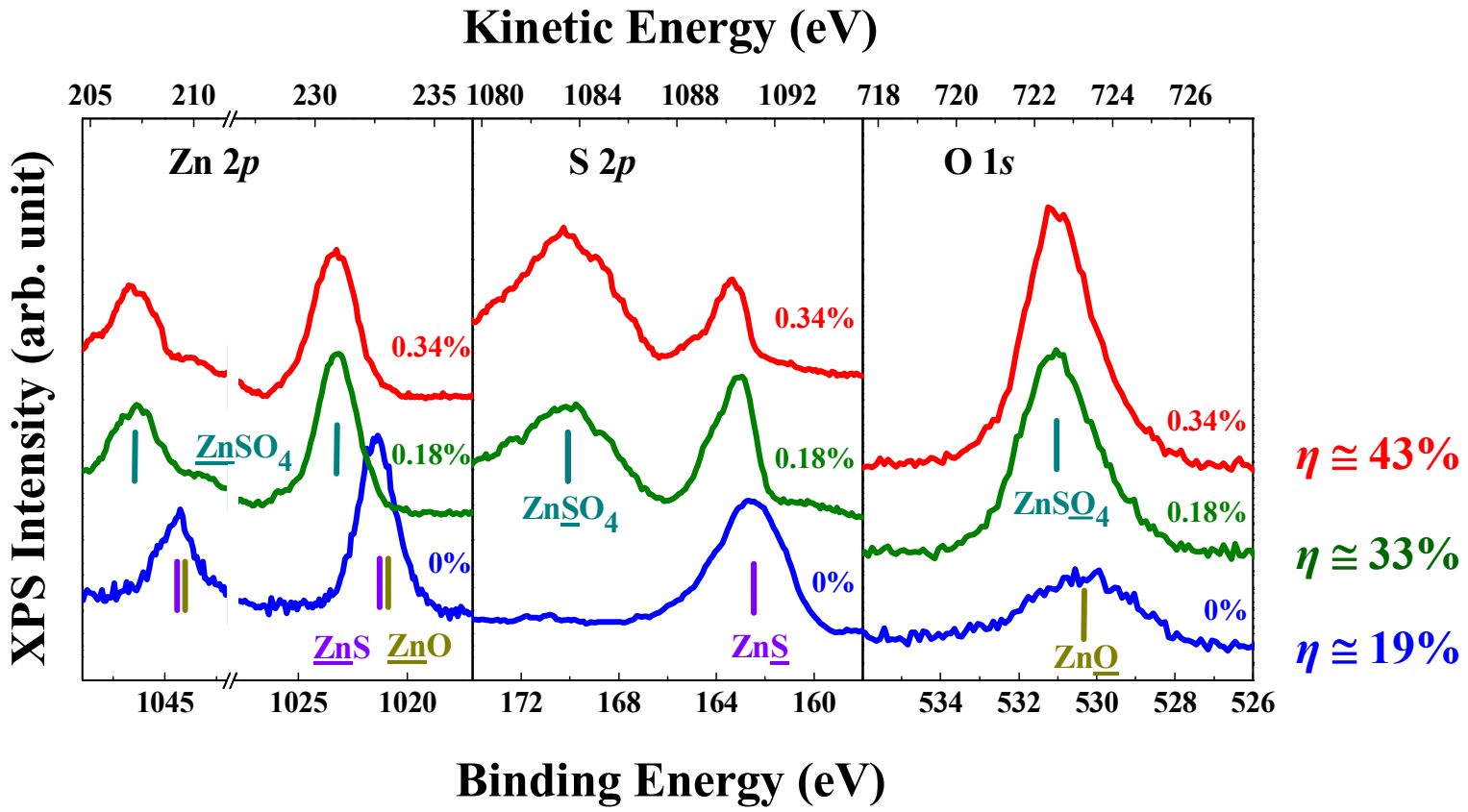

- Peak shift in the Li-added samples is attributed to the surface passivation. (from ZnS to $ZnSO_4$)
- XPS results indicate the formation of zinc-sulfate layer.
- The thickness of passivation layer ($ZnSO_4$) can be estimated from XPS data.

TEM Images

Without Li
$\eta \cong 19\%$

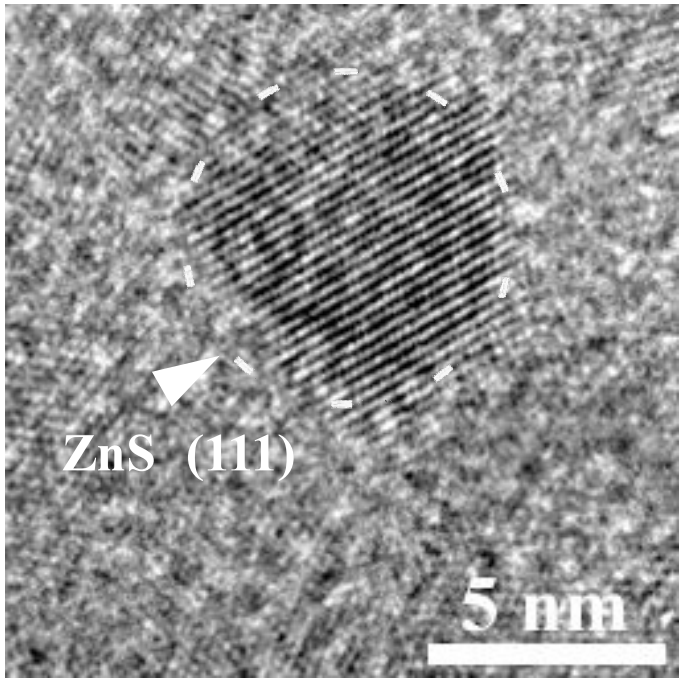

With Li (0.34%)
$\eta \cong 43\%$

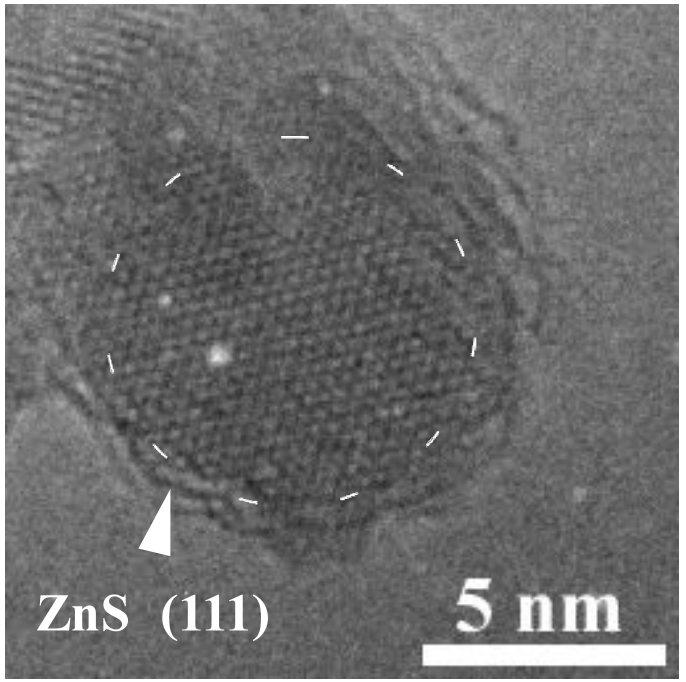

Amorphous-Layer Coated ZnS:Mn Nanoparticle

Schematic Figure for Li-Addition Effects

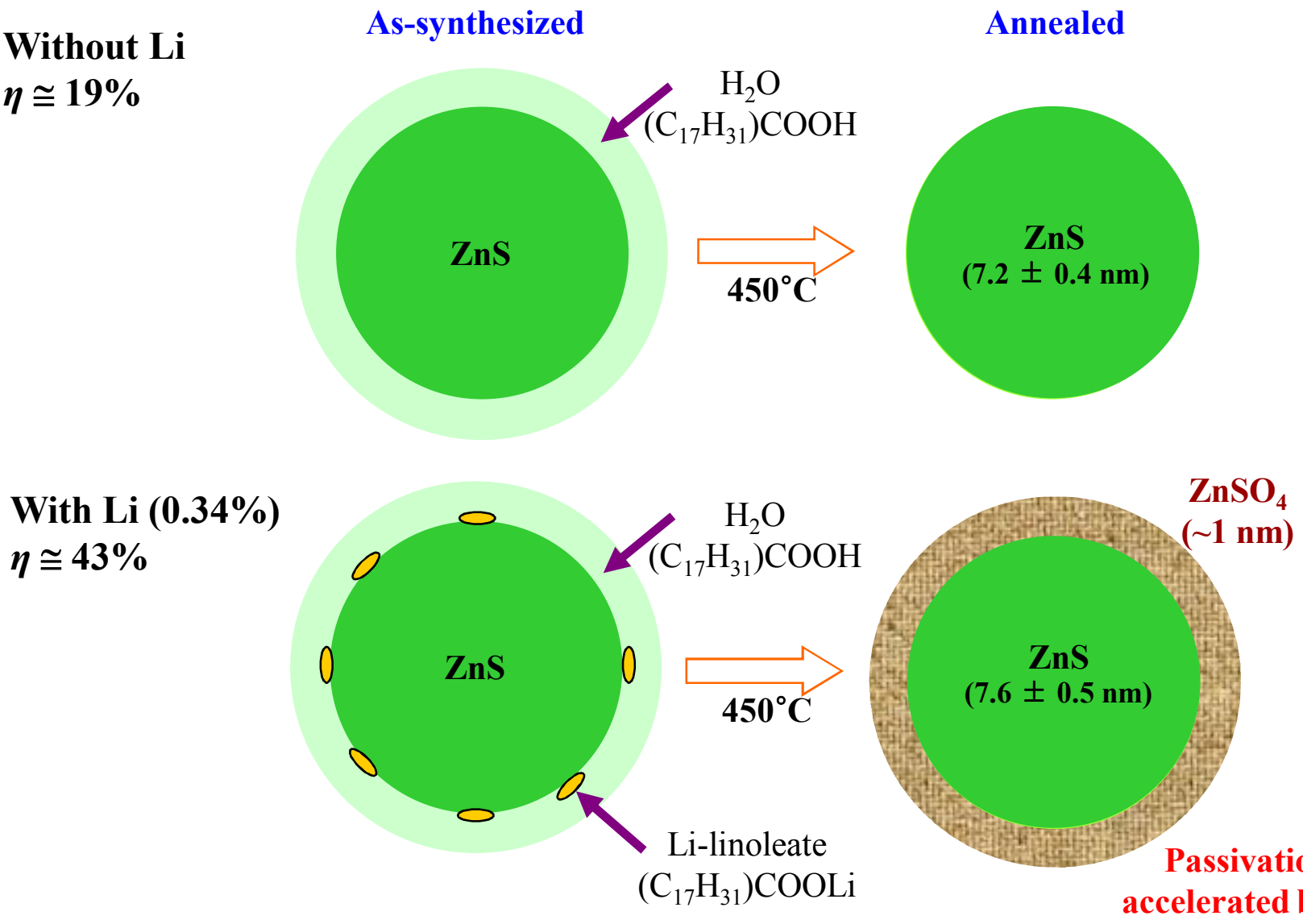

Decay Curves (Time-Resolved PL)

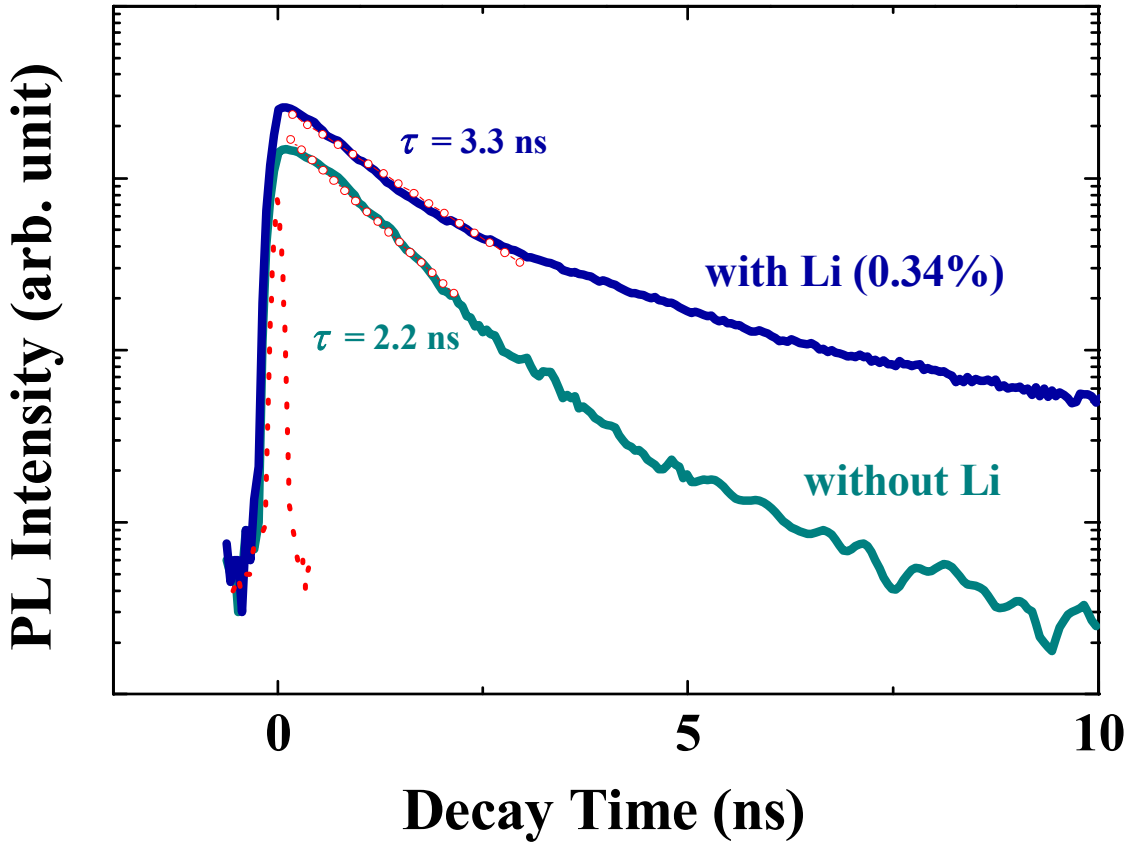

- Clear difference in the PL decay spectra.
- Ratio of the radiative/nonradiative recombination rates.

Contribution of Radiative/Nonradiative Recombination Rates

$$k_{total} = k_{rad} + k_{nonrad}$$

$$\eta = \frac{k_{rad}}{k_{rad} + k_{nonrad}} = k_{rad} \times \tau$$

Single exponential fitting for decay time ($\tau = k_{total}^{-1}$)

	Without Li	With 0.34 at. % Li (10 at. % Li precursor)
Quantum efficiency	~19%	~43%
k_{total}	$4.5 \times 10^8\ s^{-1}$	$3.0 \times 10^8\ s^{-1}$
k_{rad}	$0.9 \times 10^8\ s^{-1}$	$1.3 \times 10^8\ s^{-1}$
k_{nonrad}	$3.6 \times 10^8\ s^{-1}$	$1.7 \times 10^8\ s^{-1}$

- **Li-added samples**
  - **Radiative recombination rate ↑**
  - **Nonradiative recombination rate ↓**
- **$ZnSO_4$ capping layer**
  - **Restriction of nonradiative loss**
  - **The passivation layer activates surface Mn^{2+} ions.**

Hydroxyl-Quenching Effects on the Photoluminescence Properties of $SnO_2:Eu^{3+}$ Nanoparticles

Taeho Moon, Sun-Tae Hwang, Dae-Ryong Jung, Dongyeon Son, Chunjoong Kim, Jongmin Kim, Myunggoo Kang, and Byungwoo Park*

***J. Phys. Chem. C* (2007)**

Hydroxyl Quenching

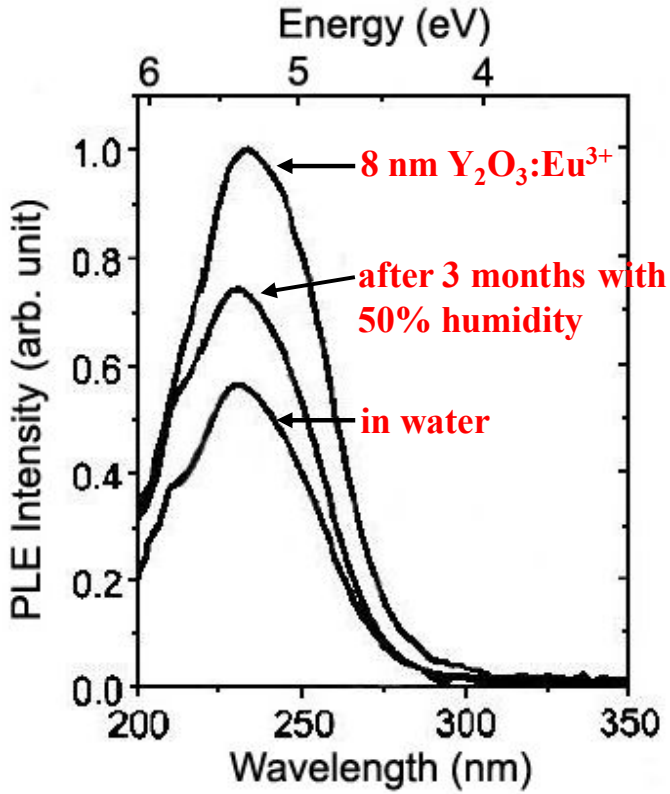

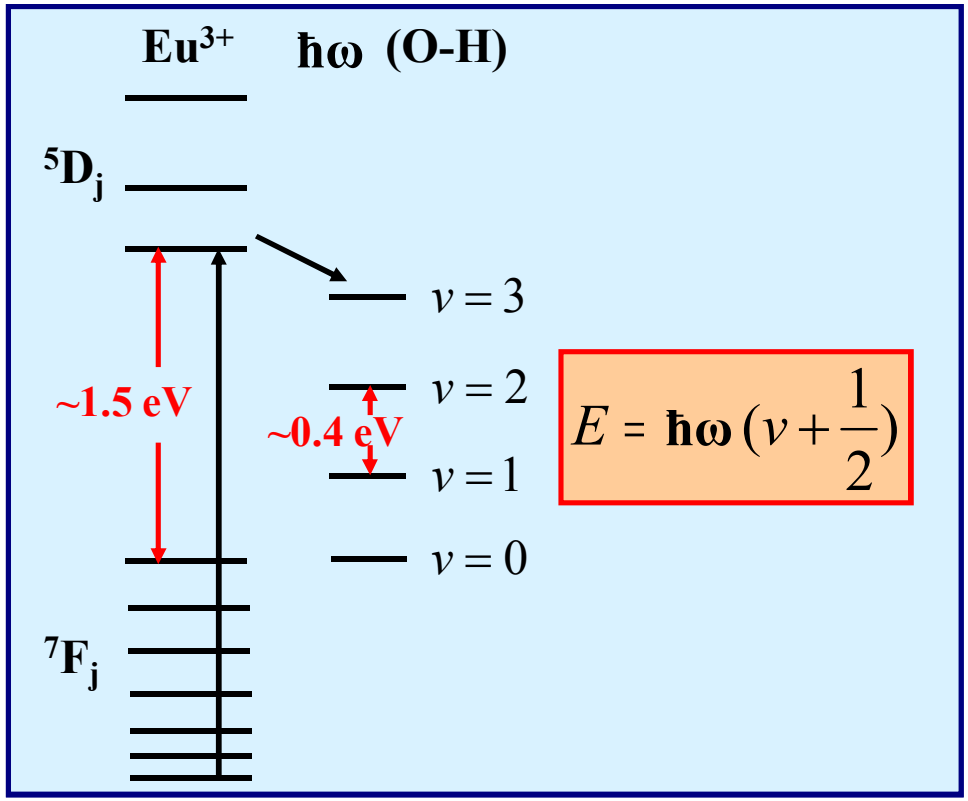

- **Strong drop of PLE intensities for nanoparticles with water**

(Schmechel's group, *JAP*, 2001)

- **Nonradiative energy transfer to the O-H vibration states**

(Horrocks' group, *Acc. Chem. Res.*, 1981)

Experimental Procedure

❖ Synthesis

- $SnCl_4$ & $EuCl_3$ (10 mol. %)
  in ethylene glycol at 180°C, for 12 h
- Calcination: 700°C - 1000°C, for 3 h, air

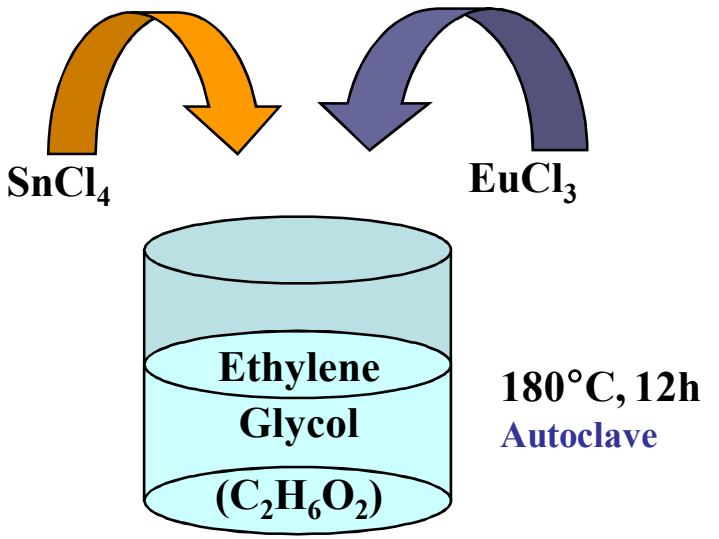

❖ Characterizations

- Photoluminescence (λ_{ex} = 325 nm)
- UV Absorption
- XPS
- XRD, FT-IR, TGA

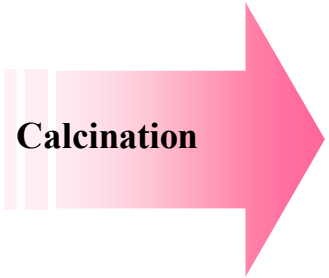

SnO_2:Eu^{3+} Nanoparticles

PL Spectra vs. Calcination Temperature

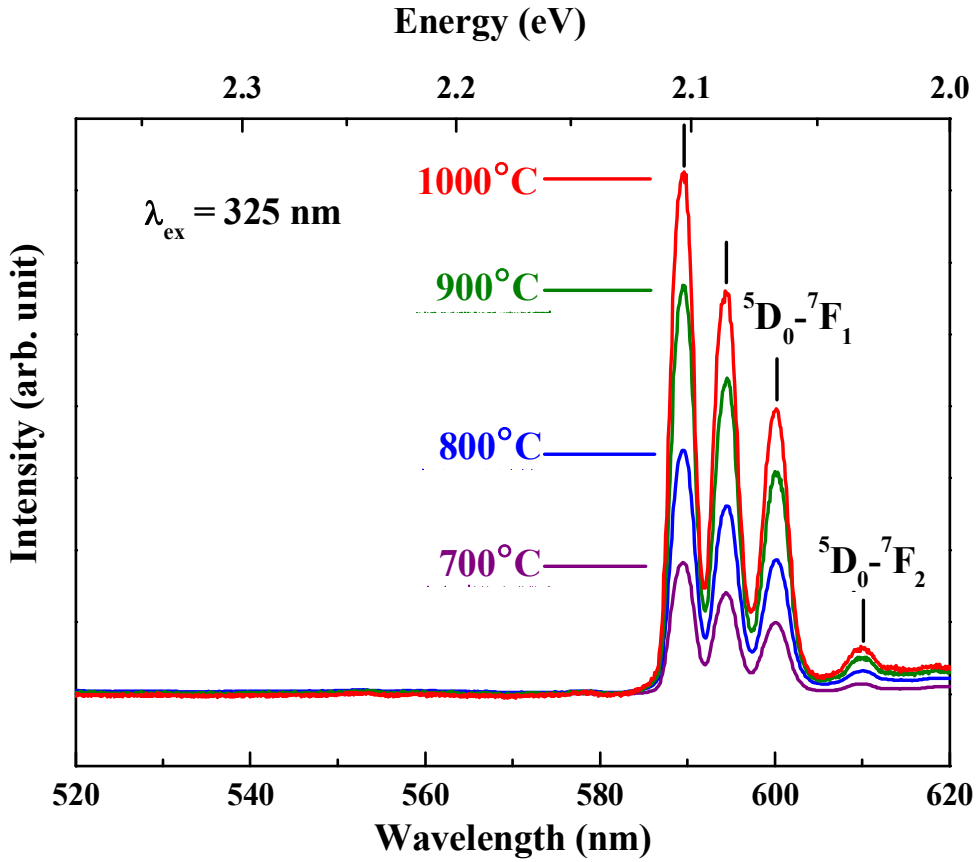

- **Reddish orange emission** increased with the calcination temperature.
- Symmetry of octahedral oxygen sites is not significantly distorted from $^5D_0$ - $^7F_2$ / $^5D_0$ - $^7F_1$ ratio.

TGA Profile of As-Synthesized $SnO_2:Eu^{3+}$ Nanoparticles

-Sn-O-Sn-OC_2H_4OH -Sn-O-Sn-OH -Sn-O-Sn-O

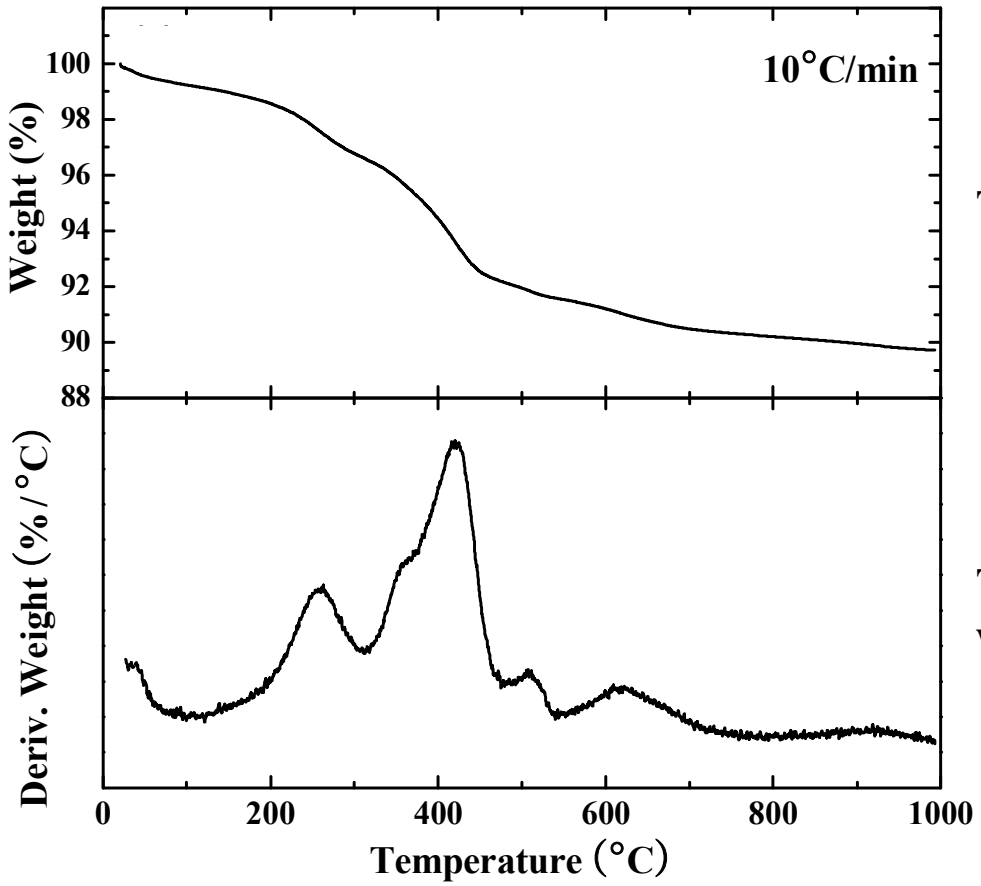

TGA profile

The first derivative of weight

Water

Residual solvent + organic

Removal of chemically-bonded OH groups

Crystallinity and Particle Size from XRD Peak Widths

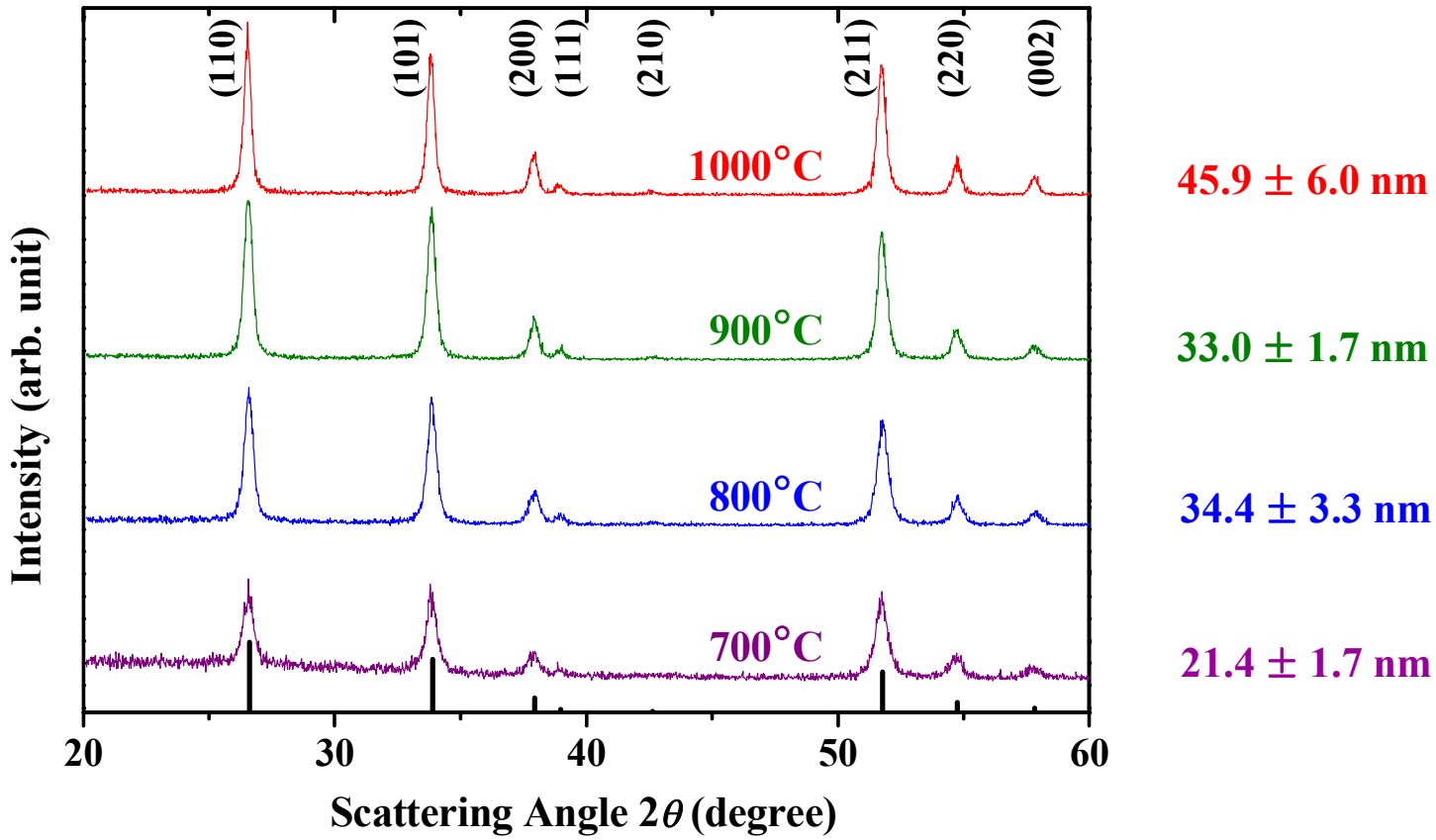

- Rutile structures without any second phase.
- Particle sizes and local strains were analyzed from the peak widths.

Local Strain vs. Calcination Temperature

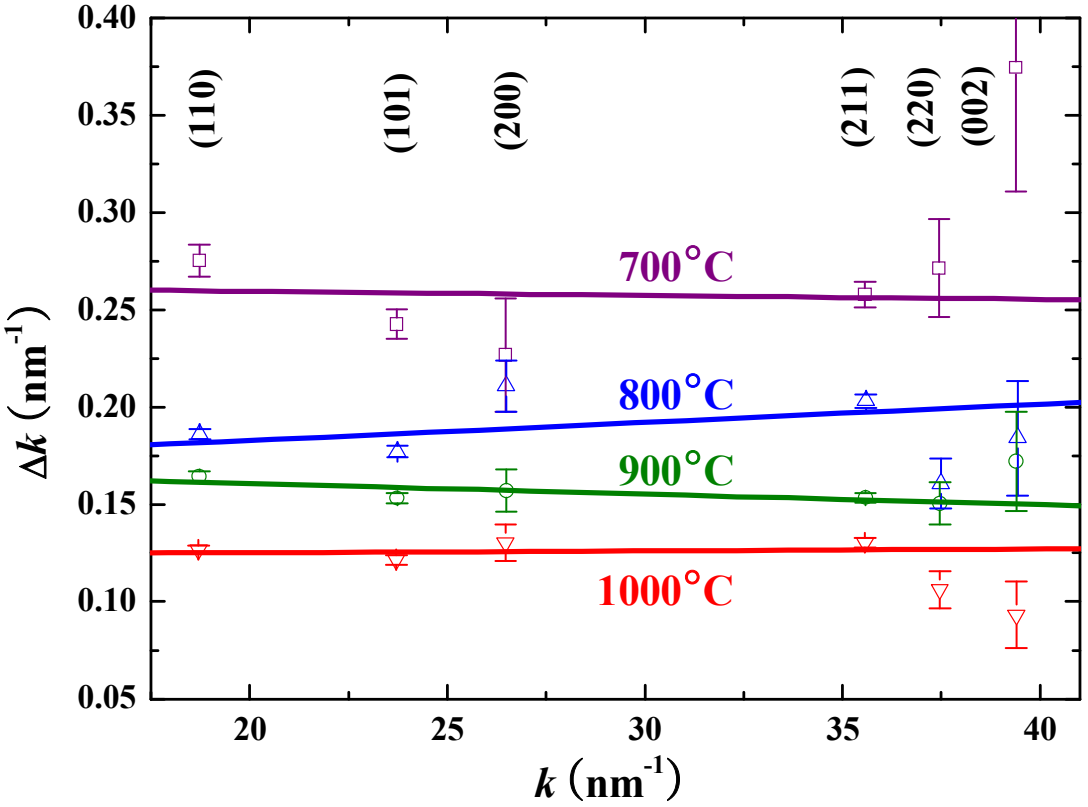

$$\Delta k = \frac{2\pi}{D} + \frac{\Delta d}{d} k$$

- Slope ($\Delta d/d$):
non-uniform distribution
of local strain

- The variation of non-uniform distribution of local strain with the calcination temperature is negligible.

Variation of Hydroxyl Groups vs. Calcination Temperature

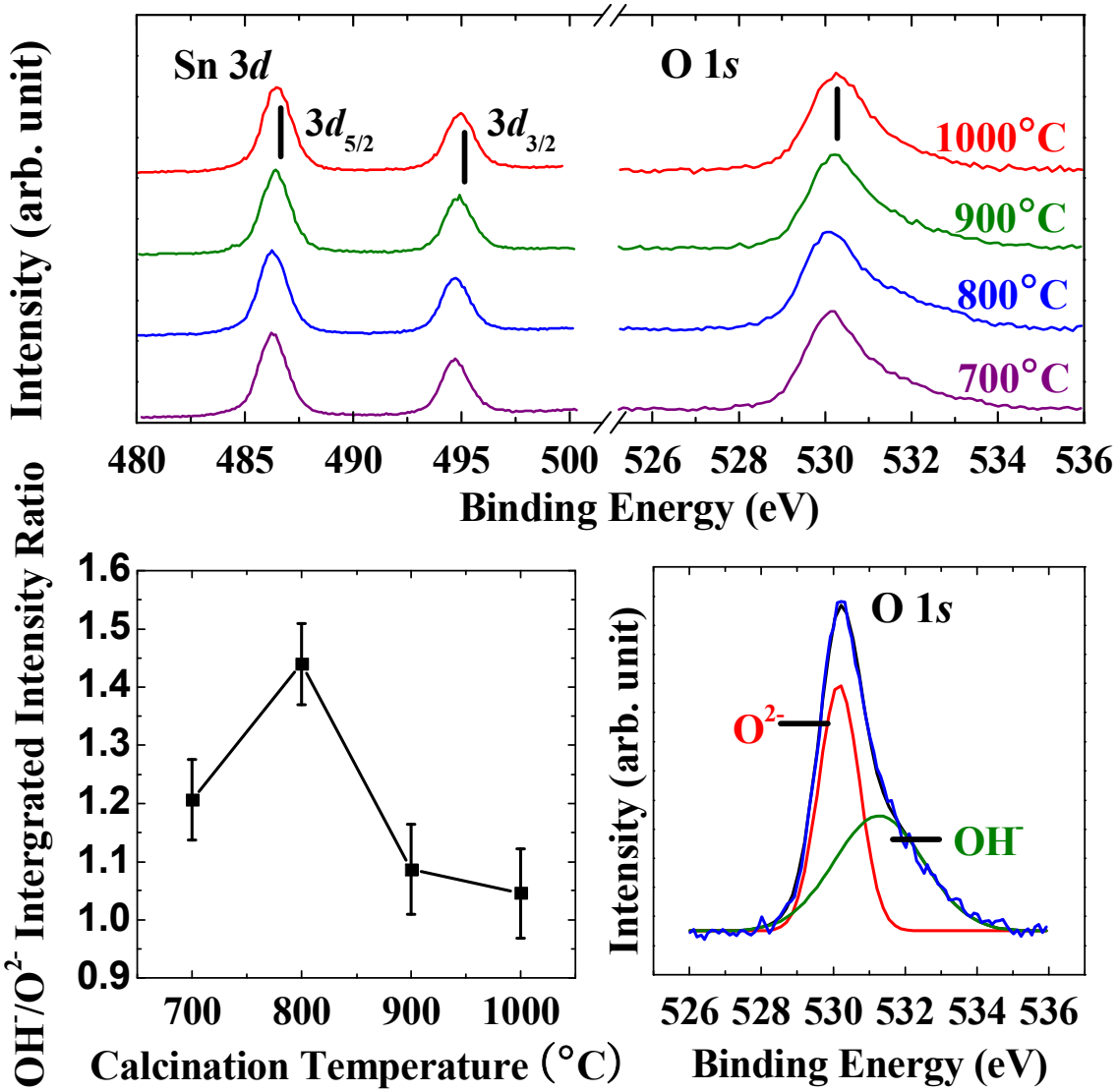

- Sn peaks are not significantly changed.
- From O peaks, correlation between OH^-/O^{2-} intensity ratios and PL intensities.

FT-IR Spectrum Showing Existence of Hydroxyl Groups

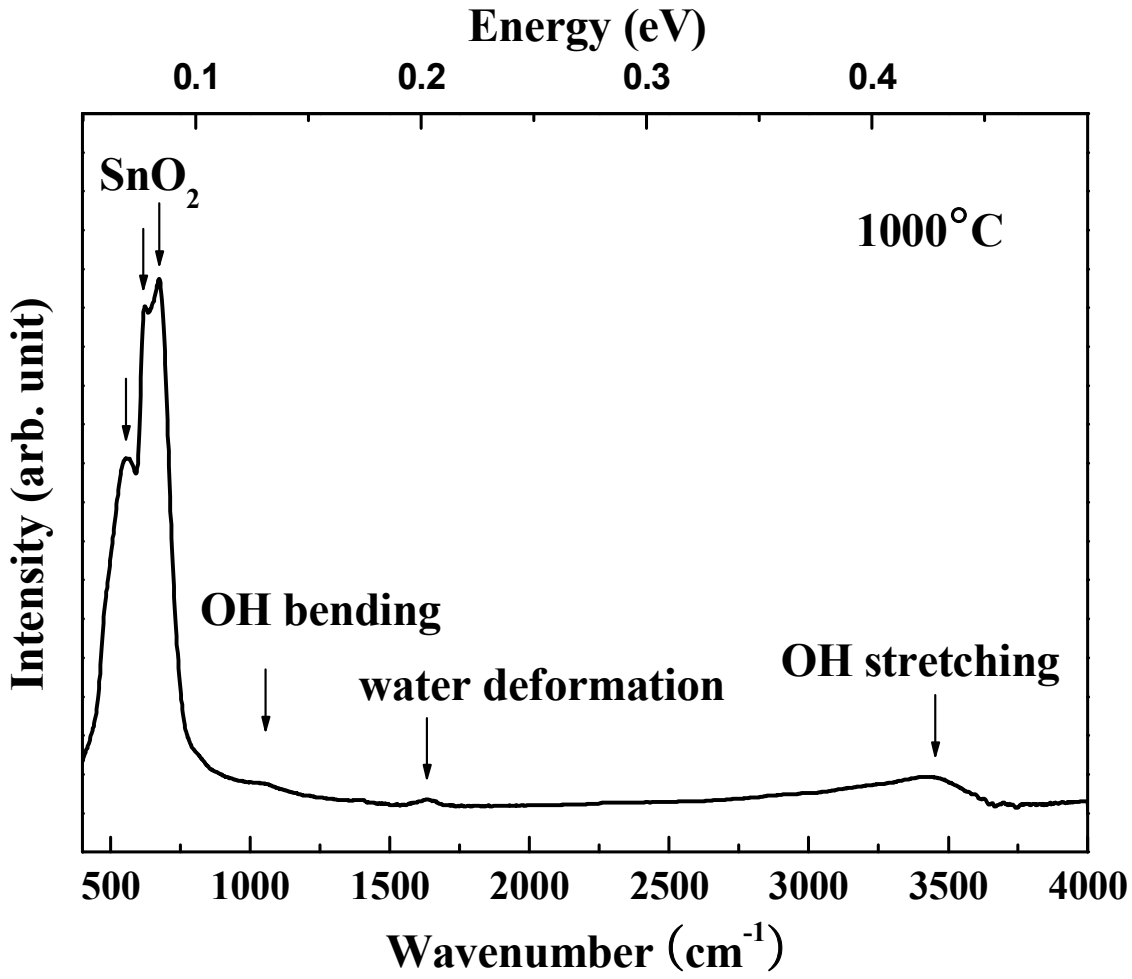

- **Hydroxyl groups still remain, even in samples calcined at 1000°C.**

Hydrothermal Treatment

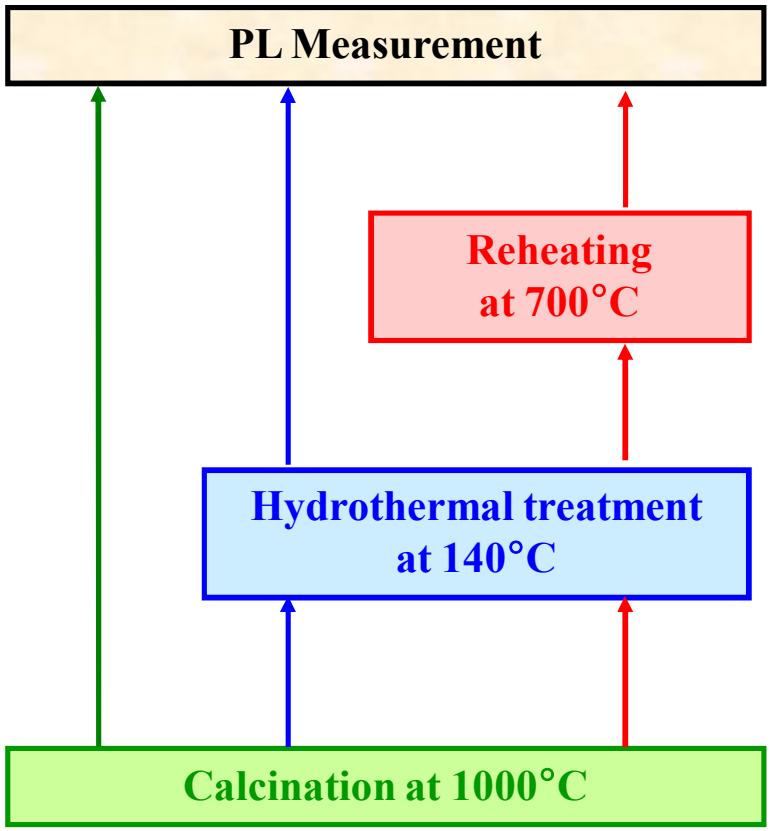

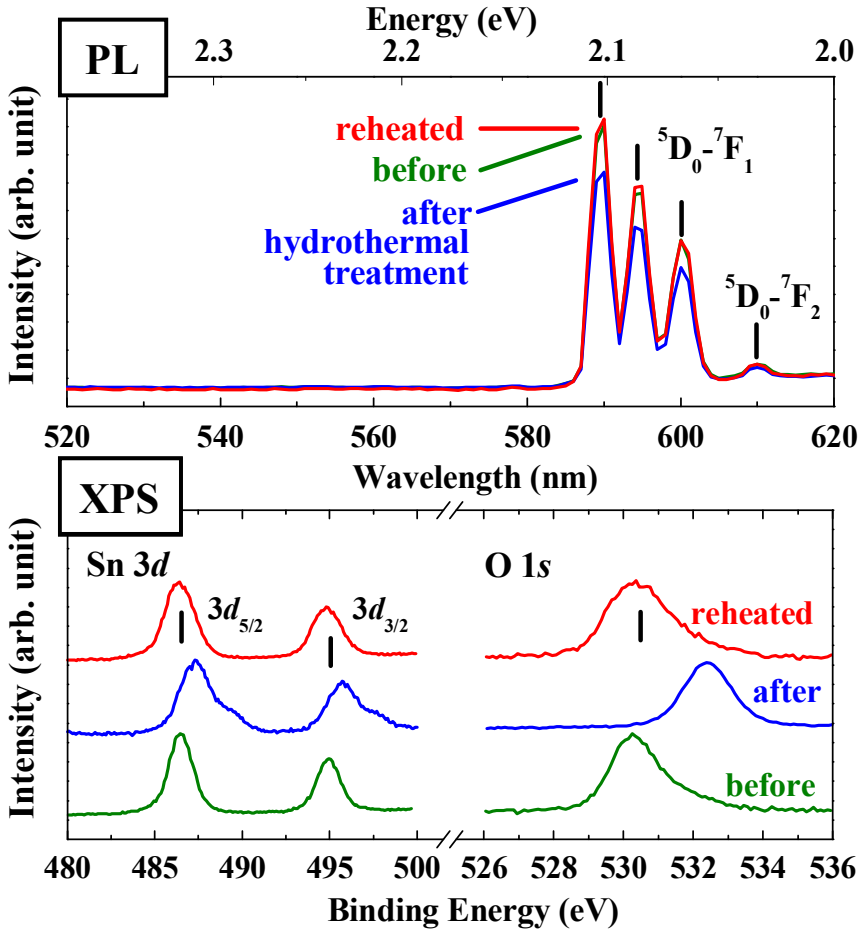

- PL spectra shows ~20% decrease after the hydrothermal treatment and full recovery after reheating.
- This behavior with XPS confirms the hydroxyl-quenching effect.